1-1-1982

Observations of SiO masers in the circumstellar envelopes of late type stars.

Adair Payson Lane
University of Massachusetts Amherst

OBSERVATIONS OF SIO MASERS

IN THE CIRCUMSTELLAR ENVELOPES OF LATE TYPE STARS

A Dissertation Presented

By

Adair Payson Lane

Submitted to the Graduate School of the
University of Massachusetts in partial fulfillment
of the requirements for the degree of

DOCTOR OF PHILOSOPHY

September 1982

Department of Physics and Astronomy

OBSERVATIONS OF SIO MASERS

IN THE CIRCUMSTELLAR ENVELOPES OF LATE TYPE STARS

A Dissertation Presented

By

Adair Payson Lane

Approved as to style and content by:

Dr. Joseph H. Taylor, Chairperson of Committee

Dr. G. Richard Huguenin, Member

Dr. Nicholas Z. Scoville, Member

Dr. Sigfrid K. Yngvesson, Member

Dr. Leroy F. Cook, Department Head
Physics and Astronomy

ACKNOWLEDGEMENTS

Many individuals have graciously provided the intellectual and moral support necessary for me to make the arduous transition from undergraduate psychology student to Ph.D. astronomer. I would like to thank everyone who has contributed to my education and growth during my graduate career at the University of Massachusetts.

I would like to express particular appreciation to a number of individuals who have made valuable contributions to the completion of this thesis. As Director of the Five College Radio Astronomy Observatory, Richard Huguenin has provided me with generous support in terms of telescope time, funding, and freedom to pursue this and other research. I am very grateful both to him and to my advisor, Joe Taylor, for their encouragement, patience, confidence, and guidance throughout the past several years. I am grateful to Nick Scoville for his support, helpful comments and critical reading of this thesis (even if he did leave the annotated manuscript under his airplane seat). I would also like to thank Sigfrid Yngvesson for his interest in this work.

The observations reported here would not have been possible without the dedicated efforts and assistance of many FCRAO staff members. Special thanks are due Read Predmore, Wayne Pleasant, Al Rodman, Steve Lord, John Putnam, Alan Parrish, and John Kapitsky for their assistance and expertice with hardware and software on numerous occasions. Nick Scoville was responsible for the excellent data reduction programs at FCRAO. Dan Clemens kindly provided the program for translation of

Haystack data tapes. Ken Bechis, Guy Blair, Read Predmore, and especially Dan Clemens provided invaluable assistance with the observations so that I could get much needed sleep during twenty-two long observing runs.

The VLBI observations were made in collaboration with Jim Moran, Mark Reid, Read Predmore, Reinhard Genzel, and Stan Hansen; I greatly appreciate their expert help and their painstaking instruction in the basics of interferometry. I would like to thank Bruce Leslie and the rest of the staff of Haystack Observatory for their help and cooperation on both single-dish and VLBI runs. I also thank Dave Buhl and Gordon Chin for their collaboration on two of the single-dish runs at Haystack.

During the course of this work, I have benefitted from helpful discussions with Steve Robinson, David Van Blerkom, John Kwan, Frank Clark, Phil Schwartz, and a number of other people; I thank them all. Tom Balonek provided crucial moral support and friendly commiseration in the final stages.

ABSTRACT

OBSERVATIONS OF SIO MASERS
IN THE CIRCUMSTELLAR ENVELOPES OF LATE TYPE STARS

(September 1982)

Adair Payson Lane, B.A., Wellesley College

M.S., Ph.D., University of Massachusetts

Directed by: Professor Joseph H. Taylor

The properties of silicon monoxide masers toward late type stars have been investigated by means of time monitoring studies and very long baseline interferometry. Spectra were obtained in the J=1-0, v=1, 2, and 3 (43 Ghz) and J=2-1, v=1 (86 Ghz) transitions of SiO toward twelve long-period variables and Orion/IRc2 at twenty-two epochs over a 2.5 year period. The integrated SiO line flux for most sources exhibits both periodic variations which correlate with the stellar infrared light cycle and secular variations.

Detailed analysis of the correspondence of velocity structure in different transitions indicates a common location for the J=1-0 masers in different vibrational states but a different origin for the v=1, J=2-1 masers. Line intensity ratios of different transitions are examined in order to further constrain maser pump models.

The v=1, J=1-0 and v=2, J=1-0 profiles are systematically skewed to the red in nine out of ten sources for which reliable determination of the stellar velocity is available; the average velocity shift of the emission centroid is 2.7 km/s. At most epochs, 65-100% of the flux in

these transitions is from redshifted gas. Over the same period, a similar predominance of redshifted emission is not present in the v=1, J=2-1 line. No evidence was found for any phase dependent variations in the fraction of the total flux which is redshifted or in any other velocity structure characteristics of the lines.

Results from two VLBI experiments using the 75 km baseline between FCRAO and Haystack are discussed. The apparent sizes of the smallest features in the J=1-0 lines toward Mira variables are $2\text{-}6\times10^{13}$cm, while for the supergiant VX Sgr, the sizes are $2\text{-}4\times10^{14}$cm. Peak brightness temperatures in the v=1 and v=2 transitions are in the range 5×10^{9} to 2×10^{10}K. Toward R Cas, the v=1, J=1-0 masers occur out to distances of at least $4R_{\star}$ (1.5×10^{14}cm). The spatial distributions of the v=1, J=1-0 and v=2, J=1-0 masers toward VX Sgr are consistent with location of the masers in an expanding circumstellar shell of radius $6R_{\star}$ ($\sim8\times10^{14}$cm). Spatial offsets of $\sim10^{15}$cm were measured between features in the v=1, J=1-0 spectra of both Orion and VY CMa.

TABLE OF CONTENTS

LIST OF TABLES

LIST OF ILLUSTRATIONS

CHAPTER I

INTRODUCTION

§1. Thesis Motivation

This thesis presents an investigation of the properties of silicon monoxide masers associated with evolved giant and supergiant long-period variable stars. Time monitoring studies of a dozen sources were undertaken in order to define the complex relationship between maser intensity and velocity structure variations and the underlying cycle of stellar variability. Nearly simultaneous observations of four maser transitions at a number of epochs over a two-and-a-half year period provide severe constraints both on possible pumping mechanisms and on the locations of masers originating from states with differing excitation requirements. High angular resolution observations using very long baseline interferometry were used to measure the sizes and spatial distribution of maser features at different velocities and to compare properties of masers in the first two excited vibrational states. The purpose of this research was twofold: to come to a better understanding of the SiO masers themselves and to use their properties to elucidate the physical conditions and kinematics in the innermost regions of the circumstellar envelopes of evolved stars.

Detailed analysis of observable maser characteristics constitutes a crucial input to models of maser excitation. Although time monitoring

and VLBI have been widely exploited in the last decade to help understand OH and H_2O masers, these techniques have not previously been applied in a comprehensive way to the study of SiO masers. The information available from these techniques is quite complementary since the questions of maser location and excitation are intimately related.

Masers are important objects for study not only because they represent an extreme astrophysical phenomenon, but because they serve as unique probes of conditions in molecular regions near stars in both the early and late stages of stellar evolution. OH, H_2O, and SiO masers sample different locales in the circumstellar envelopes and thus provide information on different physical regimes. That both OH and H_2O masers are pumped by stellar infrared radiation has been well-established. Although models for SiO masers have been developed which utilize either radiative pumping (Kwan and Scoville 1974; Deguchi and Iguchi 1976; Bujarrabal and Nguyen-Q-Rieu 1981) or collisional pumping (Elitzur 1980a), SiO is currently the least well-understood of the celestial masers and none of the available models is in complete accord with the data. The observations reported in this thesis comprise the most detailed record presently available regarding the SiO maser phenomenon.

§2. SiO Maser Emission

SiO masers are particularly useful probes of the stellar environment because of the availability of observable lines from many different

transitions. An energy level diagram for the SiO molecule is shown in Figure 1, where transitions in which maser emission has been detected are indicated by solid arrows. Rotational transition frequencies for SiO (and its istopes) may be found in Manson et al. (1977). Einstein A coefficients for various rotational and vibrational transitions of SiO are given by Hedelund and Lambert (1972) and by Tipping and Chackerian (1981). Masers in one or more rotational transitions of the first three excited vibrational states of SiO have now been detected toward over 60 late type stars. A catalogue of stellar maser sources has been published by Engels 1979.

Because population inversions are evidently maintained in states with energies as high as 5200 K, it is likely that SiO maser emission originates in the innermost regions of the circumstellar envelope, close to the stellar photosphere where the effective temperature is in the range 1800-3000 K. The proximity of the masers to the pulsating stellar atmosphere and to the region where matter is accelerated outward leads one to expect the maser emission to exhibit time variations both in intensity and velocity structure. Possible causes of maser intensity variations are changes in pump rate, variations in SiO abundance caused by changes in the rate of SiO production or destruction, and turbulence, which might affect the maser gain length or the angle of beamed radiation. Monitoring of OH (Harvey et al. 1974; Fillit, Proust, and Lepine 1977; Jewell et al. 1979) and H_2O (Schwartz et al. 1974; Cox and Parker 1979) emission from several infrared stars has demonstrated

Figure 1. SiO energy level diagram. Several of the lowest rotational states are shown for the ground and first three excited vibrational states. The (discontinuous) equivalent temperature scale is shown at the right. Solid arrows mark transitions in which SiO maser emission has been detected in at least one source; broken arrows indicate detection of non-maser emission. Detections of the various transitions are reported by the following authors:

v=0	J=1-0 :	Snyder et al. 1978; McIntosh, Lane, and Clemens 1980; Genzel et al. 1980
	J=2-1 :	Dickinson 1972; Buhl et al. 1975; Wolff and Carlson 1982
	J=3-2 :	Wilson et al. 1971; Wolff and Carlson 1982
	J=4-3 :	Schwartz, Zuckerman, and Bologna 1982
	J=5-4 :	Schwartz, Zuckerman, and Bologna 1982
v=1	J=1-0 :	Thaddeus et al. 1974; Buhl et al. 1974; Snyder and Buhl 1975
	J=2-1 :	Snyder and Buhl 1974; Kaifu, Buhl, and Snyder 1975
	J=3-2 :	Davis et al. 1974
	J=4-3 :	Schwartz, Zuckerman, and Bologna 1982
	J=5-4 :	Clemens and Lane 1982
v=2	J=1-0 :	Buhl et al. 1974
	J=2-1 :	Clark et al. 1981; Olofsson et al. 1981
	J=3-2 :	Schwartz, Zuckerman, and Bologna 1982
	J=4-3 :	Schwartz, Zuckerman, and Bologna 1982
	J=5-4 :	Clemens and Lane 1982
v=3	J=1-0 :	Scalise and Lepine 1978

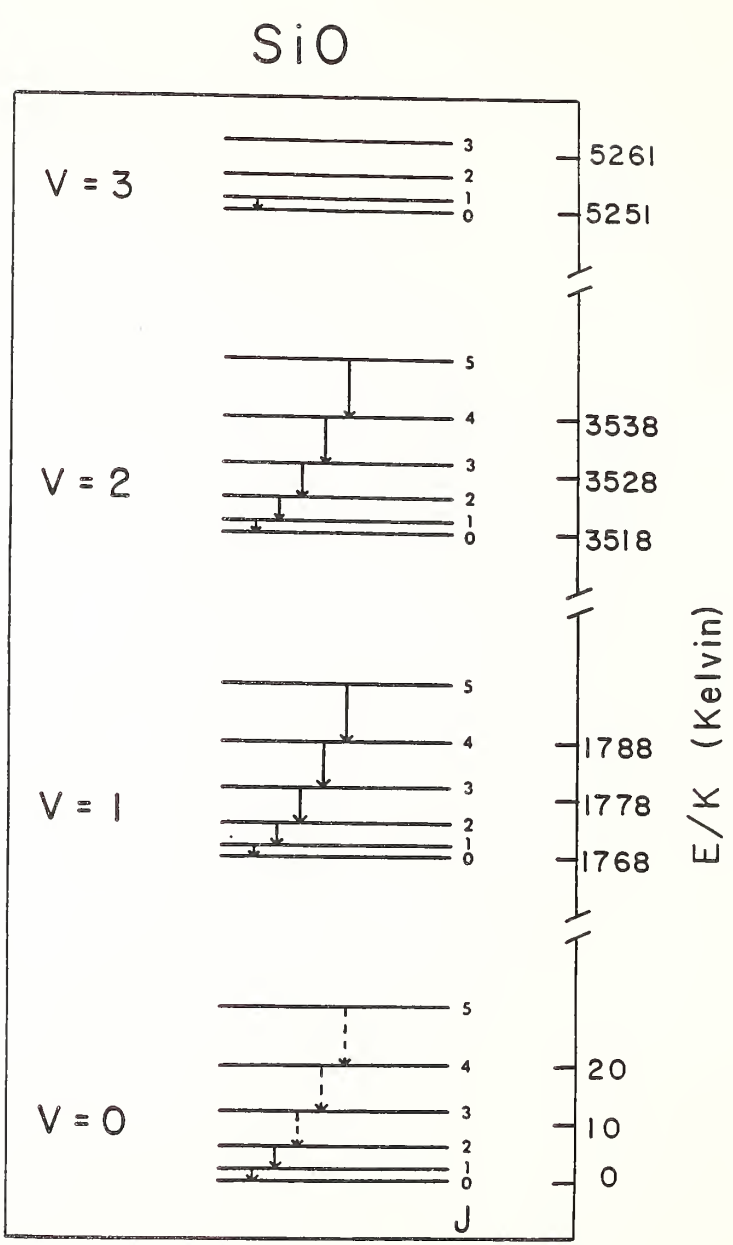
SiO
V = 3
V = 2
V = 1
V = 0
3
2
1
0
5
4
3
2
1
0
5
4
3
2
1
0
5
4
3
2
1
0
J
5261
5251
3538
3528
3518
1788
1778
1768
20
10
0
E/K (Kelvin)

that these masers often vary in phase with the stellar infrared light cycle, indicating pumping by stellar infrared photons. While previously published observations of SiO masers have suggested that a similar correlation may exist for SiO emission in the v=1 state toward two or three stars, (Spencer and Schwartz 1975; Hjalmarson and Olofsson 1979; Ukita and Kaifu 1980), well-sampled, consistently calibrated, simultaneous observations of several transitions have been lacking.

Variations in the velocity structure of SiO profiles have been even more difficult to decipher, due to the diversity and complexity of the physical and dynamical processes which are thought to be occurring in the atmospheres of long-period variables. Theoretical models of pulsating atmospheres (Hill and Wilson 1979) suggest that the regions near the stellar surface are traversed by an outwardly propagating shock wave once each cycle. If the shock passes through the SiO line formation region, its effects on the line profiles should be observable at consistent stellar phase and might even serve to locate the masers (Clark et al. 1981). The existence of photospheric oscillations, condensation of dust grains, and gas motions associated with convective cells, rotation, and turbulence might also be expected to produce observable changes in the shapes of SiO maser profiles if sufficiently detailed observations are obtained.

Measurements of the apparent sizes of maser features are important for determination of brightness temperatures and can provide estimates of the degree of saturation of the masers. While an unsaturated maser

responds exponentially to small changes in physical parameters (such as pump rate, density, or velocity perturbations), the output of a saturated maser is much less sensitive to such variations. Knowledge of the spatial extent and distribution of the maser features can help discriminate among kinematic and pumping models and can aid in determination of the input source for the masers.

§3. Properties of Long-Period Variables and Circumstellar Envelopes

The giant and supergiant variable stars which emit SiO maser radiation have been carefully studied in the visible region of the spectrum for decades and in the radio and infrared for the past fifteen years. The fact that these stars are immersed in cold, expanding envelopes of gas and dust is revealed by the blueshifted absorption cores of optical resonance lines, by infrared observations of thermal emission from dust, and by the microwave thermal and maser lines of molecules. Properties of the circumstellar envelopes of late-type stars have recently been reviewed by Zuckerman (1980). The evolutionary status and current problems of red long-period variables are discussed by Wood (1979).

Although the most popular explanation for the stellar winds of long-period variables has been radiation pressure on dust grains formed in the outer atmospheric layers (Gehrz and Woolf 1971; Kwok 1975; Menietti and Fix 1978), various difficulties with this theory remain

unresolved and alternative mass-loss mechanisms have recently received attention. These include triggering from photospheric convection (Schwartzschild 1975), sonic waves resulting from pulsational or dynamic instabilities (Fusi-Pecci and Renzini 1976; Tuchman et al. 1978, 1979; Barkat and Tuchman 1980), shock waves in the lower atmosphere (Willson and Hill 1979), Alfven waves (Hartmann and MacGregor 1980), radiation pressure on molecules (Maciel 1977), and Lyman α radiation pressure (Haisch et al. 1979). Recent review papers which discuss mass-loss from late type stars have been published by Salpeter (1977), Reimers (1977), Weymann (1977), and Cassinelli (1979).

In order to analyze the velocities of SiO maser features, the radial velocity of the central star must be known. Published measurements of the stellar velocities and terminal expansion velocities of circumstellar envelopes of stars observed in the present study are summarized in Table 1, where underlined values have been used in this thesis. The values used in the SiO analysis were chosen by consideration of both the stated formal errors and independent appraisal of the accuracy of the various available measurements. Columns 4 and 5 of Table 1 indicate the spectral line used and the reference for the determination. The OH maser lines are formed in the outer parts of the circumstellar envelope and their characteristic double-peaked profiles result from radial amplification path lengths through gas which is expanding at constant velocity. In this case, the stellar velocity corresponds to the midpoint between the velocities of the two OH peaks

TABLE 1

STELLAR AND EXPANSION VELOCITIES

SOURCE	V_* (km s^{-1})	V_{exp} (km s^{-1})	REFERENCE	
R LEO	-1.0 ± 1.0	6.5 ± 1.0	(CO 2-1)	1
	0.5 ± 0.4	5.0 ± 0.7	(v=0 SiO)	2
	0.0 ± 2.0	8.0 ± 2.5	(v=0 SiO)	3
	0.0 ± 0.8	6.3 ± 1.0	(v=0 SiO)	4
MIRA	46.3 ± 0.8	4.9 ± 0.8	(CO 2-1)	1
	42.0 ± 1.0	6.0 ± 1.0	(CO 1-0)	5
	45.0	4.0	(CO 1-0)	6
U ORI	-39.0(uncertain)	3.0	(OH)	7
		3.5	(1665 OH)	8
W HYA	40.0 ± 0.5	8.4 ± 0.7	(v=0 SiO)	2,9
	40.0	3.0	(OH)	7
		4.0	(1665 OH)	8
U HER	-13.4 ± 0.8	8.3 ± 1.3	(v=0 SiO)	2
	-15.0	4.0	(OH)	7
		6.0	(1665 OH)	8
χ CYG	9.5 ± 0.5	9.0 ± 0.5	(CO 1-0)	5
	9.5 ± 2.5	11.3 ± 2.5	(CO 2-1)	1
	9.0 ± 2.0	7.0 ± 2.0	(v=0 SiO)	3
	10.7 ± 0.6	8.8 ± 1.0	(v=0 SiO)	2,9
	12.0 ± 0.8	9.4 ± 0.8	(v=0 SiO)	4
R CAS	24.7 ± 0.5	8.9 ± 0.9	(v=0 SiO)	2,9
	24.0 ± 2.0	10.5 ± 2.0	(CO 1-0)	3
	22.0 ± 2.0	13.0 ± 1.5	(v=0 SiO)	3
	24.3 ± 0.8	8.0 ± 0.8	(v=0 SiO)	4
	24.5	10.5	(1667 OH)	10
	25.5	3.5	(OH)	7
		5.5	(1665 OH)	8

TABLE 1 continued

SOURCE	V_* (km s^{-1})	V_{exp} (km s^{-1})	REFERENCE	
IK TAU	34.0	20.0	(CO 1-0)	11
	34.0	19.0	(1612 OH)	14
	34.0	17.0	(OH)	7
	33.5	16.5	(1612 OH)	8,12
	33.0		(v=0 SiO)	13
TX CAM	7.0	7.0	(v=0 SiO)	13
	10.0	13.0	(CO 1-0)	15
VX SGR	6.0	21.0	(OH)	16
	5.5	19.5	(1612 OH)	7,8
	7.3 ± 1.0	22.7 ± 3.3	(v=0 SiO)	2
	1.4 ± 1.0	22.7 ± 3.3	(v=0 SiO)	9
VY CMA	17.6 ± 1.5	36.7 ± 2.0	(v=0 SiO)	2

Note to Table 1:
Underlined values have been used in this thesis.

References:

1 Knapp et al. 1982
2 Dickinson et al. 1978a
3 Lambert and Van den Bout 1978
4 Olofsson et al. 1982
5 Lo and Bechis 1977
6 Zuckerman 1981
7 Reid 1976
8 Dickinson, Kollberg, and Yngvesson 1975
9 Morris et al. 1979
10 Nguyen-Q-Rieu et al. 1979
11 Zuckerman et al. 1977
12 Wilson, Barrett, and Moran 1970
13 Deguchi 1981 (private communication)
14 Silverglate et al. 1979
15 Zuckerman et al. 1978
16 Moran et al. 1980 (quoted by Elitzur 1980b)

and the expansion velocity is given by one half the total velocity width of the profile. Ground vibrational state rotational lines of SiO (J=2-1) and CO (J=1-0 and J=2-1) exhibit broad emission profiles corresponding to thermal emission from the entire circumstellar envelope. The stellar velocity is determined from the central velocity of the line and the expansion velocity from half the line width at zero intensity. Most of the stellar velocity determinations used in this thesis are probably accurate to ~1 km s^{-1} or better.

The results from the SiO maser time monitoring program are presented and analyzed in Chapter II. Very long baseline interferometry measurements of SiO masers are presented in Chapter III. The results of both studies are summarized in Chapter IV and the observed SiO maser properties are compared with several published maser models. The probable location of the SiO masers is discussed in the context of recent work on the structure and dynamics of atmospheric layers and circumstellar envelopes.

CHAPTER II

TIME VARIABILITY OF SiO MASERS

§1. Observations

This chapter presents the results of a two and a half year program undertaken with the Five College Radio Astronomy Observatory (FCRAO) 13.7 m telescope and the Haystack Observatory 36.6 m telescope to monitor the time variations of SiO maser emission in several transitions. On the basis of preliminary observations made at 86 GHz at FCRAO in early 1978, thirteen of the strongest sources of SiO maser emission were selected for further observation and detailed study of intensity and line shape variations. The source list for the monitoring program is given in Table 2. Most of these sources are oxygen-rich Mira or supergiant long-period variables of late M spectral type. Periods associated with variations in the optical/IR light from the stars range from 313 to 732 days. The Orion SiO maser, the only one so far detected in a region of star formation, was also included in the monitoring, although the nature of the underlying object is still unclear.

Approximately 10,000 scans, representing some 900 hours of λ7mm and λ3mm observing time (17 runs) at FCRAO were obtained as part of the SiO monitoring project. After calibration and averaging, these scans produced 356 distinct "observations" on thirteen sources, where an "observation" means a spectrum of a given source on a given day in a

TABLE 2

SOURCE LIST FOR SiO MONITORING

SOURCE	IRC	RA(1950)	DEC(1950)	VARIABLE TYPE*	SPECTRAL TYPE	PERIOD (days)
Mira	+00030	$2^h16^m49.1^s$	$-3^o12'13"$	M	M5e-M9e	332
IK Tau	+10050	3 50 43.7	11 15 32	M	M6e-M10e	470
TX Cam	+60150	4 56 43.0	56 06 48	M	M8	557
Orion	-	5 32 47.0	-5 24 23	-	-	-
U Ori	+20127	5 52 51	20 10 06	M	M6e-M9e	372
VY CMa	-30087	7 20 55	-25 40 11	-	M5 pec	-
R Leo	+10215	9 44 52.2	11 39 42	M	M6e-M9e	313
W Hya	-30207	13 46 12.2	-28 07 03	SR	M8e-M9e	382
U Her	+20298	16 23 34.9	19 00 18	M	M6e-M9e	405
VX Sgr	-20431	18 05 03.2	-22 14 06	SR	M4e-M9e	732
χ Cyg	+30395	19 48 39	32 47 12	M	S7e-S10e	407
R Aqr	-20642	23 41 14.2	-15 33 42	M	M7e pec	387
R Cas	+50484	23 55 51.7	51 06 36	M	M6e-M10e	431

* M = Mira; SR = semi-regular.

given SiO transition. In addition, another 76 observations were obtained at Haystack at λ7mm during five observing runs. A log of the observing runs is given in Table 3. Observations were made in a total of ten SiO transitions (cf. Table 3, col. 3), with extensive monitoring data obtained in four transitions (J=1-0, v=1, 2, 3; J=2-1, v=1).

The original intent was to monitor the maser emission at either monthly or bi-monthly intervals, in order to achieve regularly spaced observations to facilitate comparisons with the stellar light curves and to aid in source-to-source comparisons. Telescope scheduling constraints and receiver availability, however, frequently necessitated more irregular sampling. Spectra were obtained at FCRAO in the v=1, J=2-1 transition (86.243350 GHz) at approximately monthly intervals during the period November 1978 to April 1979. These were augmented during the 1979-80 and 1980-81 observing seasons by observations in December 1979, January, May, and November 1980, and in June 1981, providing data in this transition over a time period which corresponds to 2-3 stellar light cycles for most sources. Spectra at 43 GHz of the J=1-0 SiO transitions in the v=1, 2, and 3 vibrational states (43.122027 GHz, 42.820539 GHz, 42.51934 GHz) were obtained during 12 observing sessions at FCRAO and Haystack starting in March 1979, with intervals between runs ranging from one week to $4\frac{1}{2}$ months. On four occasions, it was possible to obtain nearly simultaneous observations (within 1-2 weeks) at 43 GHz and 86 GHz.

At both FCRAO and Haystack the observations were made with linearly polarized feeds oriented parallel to the horizon. Since the

TABLE 3

LOG OF OBSERVATIONS

DATES	TELESCOPE	TRANSITIONS OBSERVED*	T_{RX} (SSB)
86 GHz (J = 2 - 1):			
13-17 Nov. 1978	FCRAO	v = 1	1280 K
12-13 Dec. 1978	FCRAO	v = 1	1160
13-15 Feb. 1979	FCRAO	v = 1	1340
12-16 Mar. 1979	FCRAO	v = 1	1400
23-24 Apr. 1979	FCRAO	v = 1	1550
4-5 Dec. 1979	FCRAO	v = 1	1490
29 Dec. 1979-1 Jan. 1980	FCRAO	v = 1	1430
21-23 May 1980	FCRAO	v = 1, 2	420-485
12-14 Nov. 1980	FCRAO	v = 1, 2	500-530
6-15 Jun. 1981	FCRAO	v = 1, 2	475-500
43 GHz (J = 1 - 0):			
24-25 Mar. 1979	Haystack	v = 1	1600-2000
7-9 Apr. 1979	FCRAO	v = 1, 2, 3	650-750
27-28 Aug. 1979	Haystack	v = 1	1900
24 Sept. 1979	FCRAO	v = 1, 2	700-750
23-26 Nov. 1979	FCRAO	v = 1, 2, 3	700-800
12-17 Feb. 1980	FCRAO	v = 1, 2, 3	700-800
4-9 Jul. 1980	FCRAO	v = 1, 2, 3	650-750
18-21 Aug. 1980	Haystack	v = 1, 2, 3, (4)	800-1100
27-29 Sept. 1980	FCRAO	v = 0, 1, 2, 3, (4)	650-800
4-12 Oct. 1980	FCRAO	v = 0, 1, 2, (5), (^{29}SiO v=1), (^{30}SiO v=1)	650-800
4-6 Nov. 1980	Haystack	v = 1, 2, 3	800-1400
26-27 Mar. 1981	Haystack	v = 1, 2	800-1400

* Transitions enclosed in parentheses were observed with no positive detections.

position angle of received polarization changes as the source changes hour angle, each source was consistently observed at the same hour angle from run to run (and in each transition) to eliminate variations which might be caused by source polarization effects. On several occasions, tests were performed to determine whether observations at different hour angles produced significant changes in values of total integrated flux. For most sources checked, the differences were $\lesssim$10%, i.e., less than the absolute calibration uncertainty (see §2). For one source, R Cas, in which large fractional polarization in some features at 86 GHz has been measured (Troland et al. 1979), integrated flux varied by 20-30% (Nov. 1978) for observations several hours before and after transit. Since deviations from the "normal" observing schedule were relatively rare, it is believed that the results presented in this chapter are not significantly compromised by the lack of complete polarization information.

Receiver and antenna modifications at FCRAO provided a system of continually improving quality. Prior to March 1980, the FCRAO observations at 86 GHz were made with an uncooled mixer receiver with single sideband receiver temperature in the range 1200-1500 K (see Table 3). A factor of three improvement in system noise at λ3mm was achieved beginning in the spring of 1980 by the introduction of a cooled mixer receiver. The receiver and quasi-optical sideband filter are described in detail by Predmore et al. (1980). The λ7mm receivers at both FCRAO and Haystack consisted of uncooled mixers; their measured receiver temperatures ranged from 650 to 2000 K (SSB) and are also listed in Table 3.

At FCRAO the spectral line data were processed by a 256 channel digital autocorrelation spectrometer operating with total bandwidth of either 5 or 10 MHz. Corresponding velocity resolutions were 0.12 and 0.24 km s^{-1} at 86 GHz and 0.24 and 0.49 km s^{-1} at 43 GHz. For most runs, spectra were also obtained simultaneously with two filterbanks of 256 channels of 250 kHz width and 256 channels of 1 MHz width. These data provided useful information on low-level SiO emission in the line wings and provided sufficient baseline coverage to confirm the confinement of the velocity extent of the emission to velocities close to the stellar velocity.

Spectral information at Haystack was provided by an autocorrelator operating either with 1024 channels and total bandwidth of 6.67 MHz or 512 channels and total bandwidth of 13.3 MHz. Cosine weighting of the autocorrelation function was used to provide velocity resolution of either 0.11 km s^{-1} (6.67 MHz bandwidth) or 0.45 km s^{-1} (13.3 MHz bandwidth).

All observations were made in a total power, position switching mode. At FCRAO, a reference position typically 0.1^{o} away in azimuth was observed alternately with the source at intervals of 15-30 sec to provide a blank-sky reference spectrum. At Haystack, a reference spectrum was obtained by offsetting the telescope in R.A. every 5 minutes to track the same portion of sky (and radome) as for the on-source integration.

Particular care was taken to insure accurate telescope pointing. Pointing observations on planets were made several times during each run. In addition, a five-point map (a cross in azimuth and elevation with spacing equal to the telescope half-power beamwidth) was made of each maser source prior to observation. A least-squares fit of a two-dimensional gaussian was made to the integrated intensities at the five positions to determine pointing offsets. Frequently the five-point map was then repeated one or more times at the updated position; repeatability of offsets was typically better than 1 millidegree. For each source, a typical observation consisted of 15-30 minutes spent on five-point observations, followed by 1-2 hours of integration. Observations in the weak v = 3, J = 1-0 transition utilized pointing offsets determined at similar azimuth and elevation in one of the stronger transitions.

At FCRAO, a pointing error of 2 millidegrees produces an error in line intensity of ~1% at 43 GHz and ~3.5% at 86 GHz. With the smaller Haystack beam, 2 mdeg corresponds to an intensity error of ~5%, while a 4 mdeg offset corresponds to an error of 22%. It is estimated that pointing was not a significant source of error at FCRAO. Although the rms pointing accuracy at Haystack is typically ~2 mdeg, some observations may have been affected by recently detected anomalies in the pointing and tracking characteristics of the Haystack antenna (Evans and Haschick 1981, private communication); a few Haystack observations have been corrected for pointing errors detected after the data were taken.

§2. Calibration

In order to compare observations of the absolute intensities of maser lines obtained with different telescopes under a variety of observing conditions, particular care must be taken in the absolute calibration of the data. The usual problems encountered in millimeter-wave spectral line calibration were occasionally compounded by changes and improvements made to the FCRAO telescope and receiver system during the $2^1/2$ year period of the observations. In addition to the use of a number of different receivers, the telescope surface panels at FCRAO were reset twice during the observing program, producing changes in the antenna efficiency (cf. Table 4) and pointing characteristics, and a calibration chopper wheel was available only on three of the later runs at λ3mm and on none of the runs at λ7mm.

The ultimate goal of the calibration procedure is a determination of the source flux density, S_ν, from measurement of the spectral line antenna temperature. The observed antenna temperature, T_A, must first be corrected for atmospheric attenuation, receiver gain, and antenna and radome losses. Following the treatment of Ulich and Haas (1976), the "corrected antenna temperature", T_A^*, is defined as:

$$T_A^* = T_A \frac{e^{\tau_o A}}{G_s \eta_l} = \frac{S - R}{R} T_{sys} \frac{e^{\tau_o A}}{G_s \eta_l} \quad , \qquad \text{(II-1)}$$

where $(S - R / R)$ is the normalized difference spectrum obtained from source (S) and reference (R) positions, G_s is the gain in the signal

TABLE 4

FCRAO 13.7m TELESCOPE CHARACTERISTICS* APPLICABLE TO CALIBRATION OF SiO MONITORING DATA

	ν	1978-1980	1980-1981
Aperture efficiency (η_A):	43 GHz	0.45	0.48
	86 GHz	0.29	0.35
Telescope sensitivity (flux density per ^{o}K of corrected antenna temperature):	43 GHz	42 Jy/^{o}K	39 Jy/^{o}K
	86 GHz	65 Jy/^{o}K	53 Jy/^{o}K
Telescope loss efficiency (η_l):	43 GHz	0.93	0.91
	86 GHz	0.89	0.89

* Including radome effects.

sideband, η_l is the telescope loss efficiency, τ_o is the zenith atmospheric opacity in the signal sideband, A is the airmass (=csc(el)), and T_{sys} is the double-sideband system temperature. The system temperature is defined as the antenna temperature observed with the telescope pointed at blank sky. It includes noise contributions due to emission from the receiver/waveguide system, emission from the atmosphere and radome entering all sidelobes which look at sky, and emission at the ambient temperature entering sidelobes which do not look at sky. For the circumstances encountered in the present work (except for minor modifications used in the model for the 'skydip' program, see p. 23), the following terms have been included in the system temperature:

$$T_{sys} = T_{RX} + \eta_l T_{atm} (1 - e^{-\tau_o A}) + (1 - \eta_l) T_{amb} , \qquad (II-2)$$

where T_{RX} is the receiver temperature measured at the feed, T_{atm} is the mean or effective atmospheric temperature, and T_{amb} is the ambient temperature. The loss efficiency η_l gives the fraction of the total power which originates from the sky. Determination of each of the four parameters (T_{RX}, τ_o, T_{atm}, η_l) upon which accurate calibration depends is discussed below.

Receiver temperature. At FCRAO, the receiver temperature was measured with hot/cold loads each time the receiver was tuned to a new frequency. The cold load consisted of a piece of microwave absorber saturated with liquid nitrogen, while the hot load was a piece of absorber at ambient

(radome) temperature. After measuring and subtracting a d.c. bias from the hot and cold load voltages (V_H, V_C), the double-sideband receiver temperature was calculated from

$$T_{RX}\ (DSB) = \frac{T_H - (V_H/V_C)\ T_C}{V_H\ /\ V_C\ - 1}\ , \qquad (II\text{-}3)$$

where T_H is the ambient temperature in the radome and T_C was taken to be 80 K. Since the relative gains in the signal and image sidebands were unknown, they were assumed equal, and T_{RX} (SSB) was obtained by doubling T_{RX} (DSB). For the receiver temperature measurements at 86 GHz, a 30 MHz filter was usually placed in the second IF to restrict the bandwidth during the calibration to the narrow window appropriate to the autocorrelator. In cases where this was not done, the receiver temperature measured over the full 400 MHz IF bandpass was adjusted by an appropriate amount. From the repeatability of measurements of the receiver temperature on a given run, it is estimated that the relative uncertainties in the values of T_{RX} used to calibrate the data are ~5-7%. A primary source of uncertainty is the assumption of equal sideband gain. This uncertainty affects only the absolute intensities; variability of the sources is well-determined from the care taken with the calibrations.

Atmospheric opacity. During each observing run where a calibration chopper wheel was not available, the zenith atmospheric opacity τ_o was determined several times a day by one of several techniques. These

included: a) antenna tipping measurements, using the on-line 'skydip' program at FCRAO (written by the author), b) measurement of the elevation dependence of the brightness of Jupiter, the Sun, or the Moon, and c) measurement of the elevation dependence of the integrated line flux of a strong SiO source at low elevations. These methods are briefly described below and sample results are illustrated in Figs. 2 and 3.

The automatic 'skydip' program makes a series of 15 observations of blank sky at elevations corresponding to airmasses from 4.6 to 1.1 to 4.6, with intervals of 0.5 airmasses. A calibration constant determined by a hot/cold load measurement must be entered into the computer to convert the measured voltages to antenna temperatures. The observed antenna temperature on blank sky at airmass A is assumed to be made up of contributions due to receiver noise, self-absorbed radome emission coming into all sidelobes, ground radiation entering sidelobes not pointed at sky, attenuated by the radome, and self-absorbed atmospheric emission into sidelobes looking at sky, also attenuated by the radome:

$$T_{obs}(A) = T_{RX} + T_{rad}\,(1 - e^{-\tau_{rad}}) + (1 - \eta_l)\,T_{amb}\,e^{-\tau_{rad}} + \eta_l\,T_{atm}\,e^{-\tau_{rad}}\,(1 - e^{-\tau_o A}), \qquad \text{(II-4)}$$

where T_{rad} is the measured radome temperature, τ_{rad} is the radome opacity (including both space frame blockage and membrane attenuation), assumed to be 0.18, and T_{amb} is the ambient temperature. For the 'skydip' model, η_l was assumed to be 0.9 (see below). The program performs an iterative least squares fit to determine the unknowns τ_o, T_{atm},

and $T_{RX}(DSB)$. Under certain conditions, (e.g., when τ_o is small), an improved solution for τ_o is obtained by holding T_{atm} constant at a value specified by the observer (usually T_{amb} minus 10 to 20 K). A quadratic polynomial approximation to the full exponential function is first fit to the data to determine if sufficient curvature is present for a reliable determination of T_{atm}. An example of an opacity measurement produced by the 'skydip' program is shown in Fig. 2. The program is described in more detail by Lane (1978).

When bright solar system objects (e.g., Jupiter, the Sun, or the Moon) were observable at relatively low elevations where airmass changes rapidly, the difference between their intensity and that of blank sky was measured as a function of airmass to derive a value of τ_o. By subtracting the off-source measurement from the on-source measurement, a calibration signal proportional to $e^{-\tau_o A}$ is obtained. A plot of the natural logarithm of such measurements versus airmass produces a straight line with slope $-\tau_o$. Sample measurements at 86 GHz are shown in Fig. 3, where a linear regression has been fit to the observed points to determine the value of τ_o indicated on each plot. In general, this method (although more time-consuming than 'skydip' measurements) provided reliable opacity values which were in agreement with 'skydip' opacities to within 0.02-0.03 on the occasions where comparison was made.

A third method of opacity determination utilized observations of integrated SiO line flux (usually of Orion) at low elevations (cf.

Figure 2. Skydip calibration at 43 Ghz. Each data point represents two observations at the indicated airmass. The solid line is a least squares fit of a quadratic approximation to Eq. II-4 to the data.

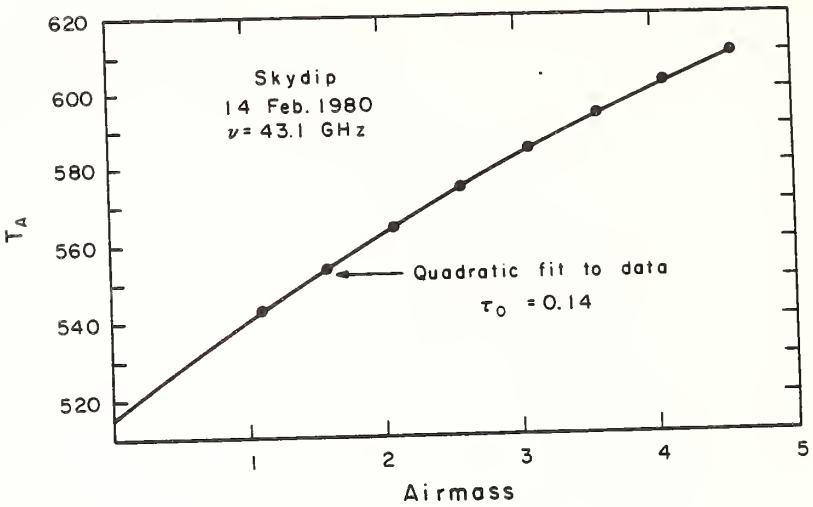
620
600
580
560
540
520
T_A
Skydip
14 Feb. 1980
ν = 43.1 GHz
Quadratic fit to data
τ_0 = 0.14
1
2
3
4
5
Airmass

Figure 3. Opacity measurements at 86 GHz and 43 GHz. Observing procedure is described in the text. The linear least squares fit to the data yields the value for τ_o indicated on each plot.

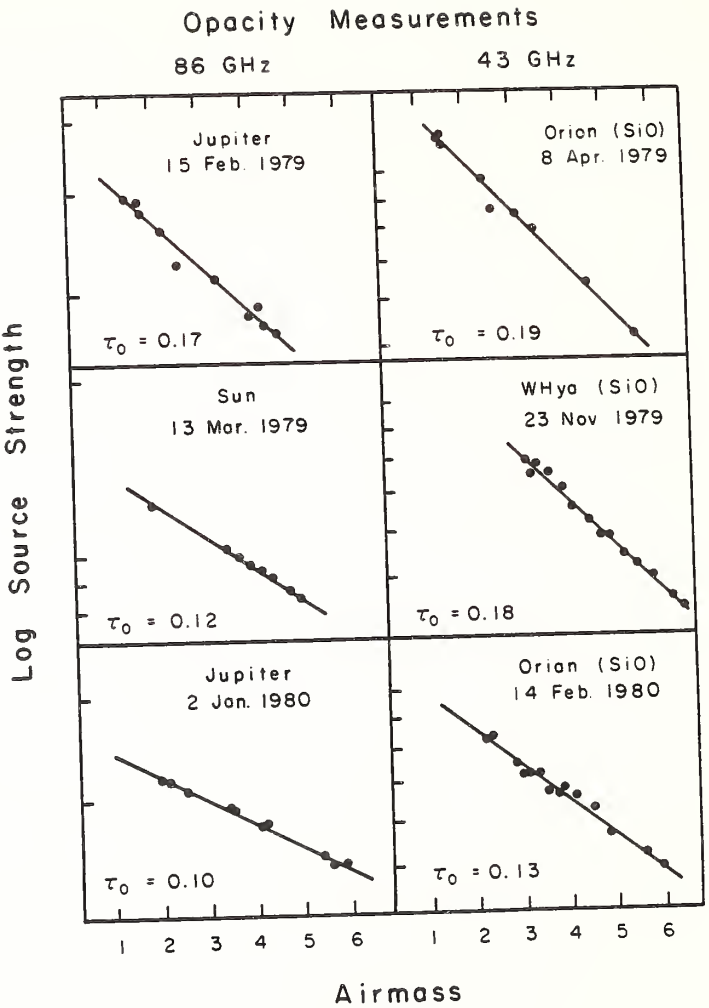
Opacity Measurements
86 GHz
43 GHz
Jupiter
15 Feb. 1979
τ_0 = 0.17
Orion (SiO)
8 Apr. 1979
τ_0 = 0.19
Sun
13 Mar. 1979
τ_0 = 0.12
WHya (SiO)
23 Nov 1979
τ_0 = 0.18
Jupiter
2 Jan. 1980
τ_0 = 0.10
Orion (SiO)
14 Feb. 1980
τ_0 = 0.13
Log Source Strength
1 2 3 4 5 6
1 2 3 4 5 6
Airmass

Figure 3). For these measurements, and also those of the planets, efforts were made to insure that pointing drift was not contaminating low elevation points. As the scatter in the data points in Fig. 3 indicates, reliable measurements of atmospheric opacity were obtainable using masers and solar system objects. In all but the worst weather conditions (e.g., rain, heavy snow), values of τ_o ranged from 0.09 to 0.20 at 43 GHz and from 0.09 to 0.22 at 86 GHz.

Atmospheric temperature. The emission and absorption properties of the atmosphere at millimeter wavelengths are due to both oxygen and water vapor and are notoriously difficult to estimate from ground-based measurements. While the oxygen opacity of the atmosphere is fairly constant with time, the atmospheric temperature and H_2O opacity depend on the time-variable H_2O content of the atmosphere and its distribution with height. Various estimates of appropriate values for the mean or effective atmospheric temperature, T_{atm}, are discussed by Lane (1978). Although 'skydip' observations and data-fitting sometimes produced physically reasonable values for T_{atm}, for simplicity a value of $T_{atm} = T_{amb} - 10$ K was assumed in the final calibration of the SiO data via Eqs. (II-1) and (II-2). Uncertainty of 20 K in the value of T_{atm} produces an uncertainty in source intensity of $\lesssim$1-2% given the total system noise in this study.

Telescope loss efficiency. The telescope efficiency η_l was determined at both λ7mm and λ3mm from "chopper wheel skydip" measurements performed either automatically (λ3mm) or manually (λ7mm). The chopper wheel method utilizes a quantity defined as

$$T_{cw} = \frac{T_{amb}}{\frac{P_{amb}}{P_{sky}} - 1} \qquad \text{(II-5)}$$

as an approximation to the factor $T_{sys}\, e^{\tau_o A} / G_s\, \eta_l$ needed to scale raw spectral line data (cf. Eq. II-1). Here P_{amb} is the noise power from the receiver when observing an ambient temperature load and P_{sky}, the noise power on blank sky, is proportional to T_{sys} as defined by Eq. II-2. The basis for this procedure is discussed in detail by Penzias and Burrus (1973), Davis and Van den Bout (1973), and Schloerb and Snell (1980).

A sample set of measurements of T_{cw} vs. A, obtained at 86 GHz during an SiO run on May 22, 1980, is shown in Fig. 4. By extrapolating the curve to A = 0, a value is obtained for

$$T_{cw}\ (A=0) = \frac{T_{amb}}{\frac{T_{RX} + T_{amb}}{T_{RX} + (1-\eta_l)\, T_{amb}} - 1} \quad . \qquad \text{(II-6)}$$

Solving for η_l gives

$$\eta_l = \frac{T_{RX} + T_{amb}}{T_{cw}(A=0) + T_{amb}} \quad , \qquad \text{(II-7)}$$

where T_{RX} is measured with hot/cold loads. An average of ten such determinations of η_l obtained in July 1980 at λ7mm gave

$$\langle \eta_l \rangle = 0.931 \pm 0.018$$

Figure 4. Chopper wheel skydip at 86 GHz. The observations compare the emission from blank sky with that from an ambient temperature absorber (see text). Extrapolation of the curve to zero airmass yields the telescope loss efficiency η_l.

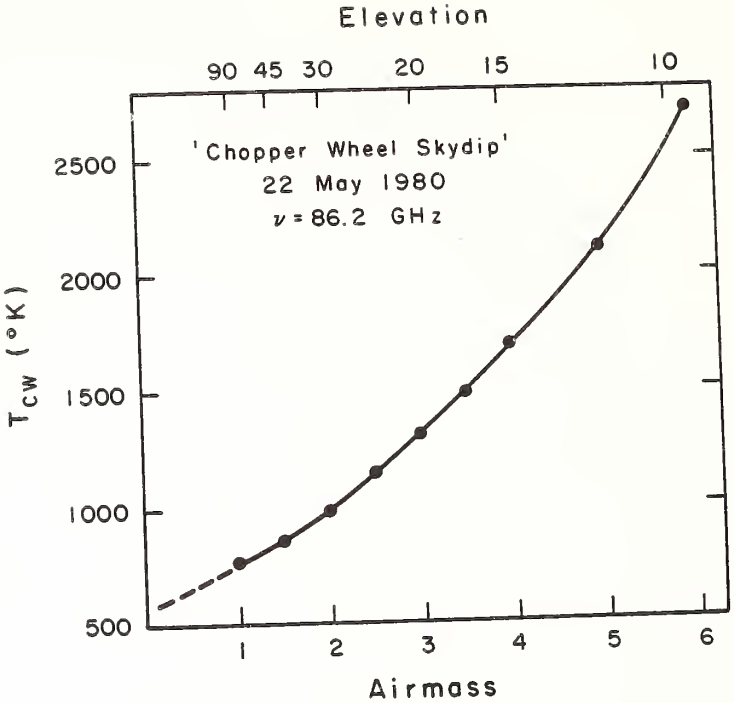
Elevation
90 45 30 20 15 10
'Chopper Wheel Skydip'
22 May 1980
ν = 86.2 GHz
2500
2000
1500
1000
500
T_CW (°K)
1 2 3 4 5 6
Airmass

while six measurements made in Oct. 1980 at λ7mm gave

$$\langle \eta_l \rangle = 0.906 \pm 0.030 \quad .$$

At λ3mm, a value of $\eta_l = 0.891$ was obtained in May 1980. These values were used in the calibration of all of the SiO data from FCRAO.

Summary of calibration and reduction of FCRAO data. Each 3-5 minute scan taken at FCRAO was converted to a corrected antenna temperature scale (T_A^*) by one of two methods. The final three runs at 86 GHz were calibrated using the chopper wheel method (Penzias and Burrus 1973; Schloerb and Snell 1980), which is probably accurate to a few percent at the relevant frequencies. For the May 1980 run, comparison of our chopper wheel calibrated intensities with nearly simultaneous measurements at Onsala Space Observatory of five strong v = 1, J = 2-1 masers showed agreement to within 2-20% (Olofsson et al. 1981). For R Cas, intensities from the two observatories agreed to within ~30%. Some of the differences may be due to the effects of polarization rather than to calibration difficulties at one or both observatories. Spectra from the remaining 14 runs at FCRAO were individually scaled according to Eqs. (II-1) and (II-2) using measured values of T_{RX}, τ_o, and η_l. An error in τ_o of 0.05 produces an intensity error of less than 11% for elevations above 25°; therefore, probably only the three low declination sources (VX Sgr, W Hya, and VY CMa) suffer significant uncertainties due to atmospheric attenuation. Uncertainties in T_{RX} and in relative sideband gain lead to an estimate of 15-20% for the overall uncertainty in the absolute calibration. The relative uncertainty (source-to-source and run-to-run) is probably smaller than this.

A rough check of the relative calibration uncertainty from run to run was made for the runs at 86 GHz by computing the average integrated flux for a set of eight sources observed on each run. Although the number of sources is rather small to expect complete cancellation of time variability effects, these averages deviated from their mean value by $\leq$15% for all runs except Apr. 1979, which was 22% above the mean. A similar test for the 43 GHz runs indicates the relative calibration accuracy from run to run (including comparison of runs at the different observatories) is ~10-15%.

For each observation, a linear baseline was removed from the spectra and scans were averaged with weighting proportional to $(\mathrm{rms})^{-2}$. Since masers are effectively point sources, antenna temperatures were converted to flux densities using the relation:

$$S_\nu = \frac{2\ k\ T_A^*}{A_g\ \eta_A} \quad ,$$

where T_A^* is defined in Eq. (II-1), k is Boltzman's constant, A_g is the telescope geometric area, and η_A is the aperture efficiency. The aperture efficiencies at 43 GHz and 86 GHz were determined from observations of the antenna temperature of Jupiter, corrected for the beam broadening of the source size as follows:

$$T_A^*(\mathrm{Jup.}) = T_B(\mathrm{Jup.})\ \frac{\eta_A\ A_g}{\lambda^2}\ \Omega_s(\mathrm{eff})$$

$$= T_B(\mathrm{Jup.})\ \frac{\eta_A\ A_g}{\lambda^2}\ \frac{\pi\ \theta_s^2}{4}\ \frac{1}{\ln 2}\ \left(\frac{\theta_B}{\theta_s}\right)^2\ \left(1 - \exp\left(-\ln 2\ \left(\frac{\theta_s}{\theta_B}\right)^2\right)\right)$$

where Ω_s(eff) is the effective source size of Jupiter, θ_B is the antenna main beam half-power-beamwidth, and θ_s is the true angular diameter of Jupiter. The brightness temperature of Jupiter was assumed to be 180 K at 86 GHz (Ulich et al. 1980) and 160 K at 43 GHz (Schloerb and Snell 1980). Values of η_A used to scale the SiO data are listed in Table 4; the improved values for 1980-81 are a result of surface panel readjustments made in August 1980.

Summary of calibration and reduction of Haystack data. For ease of manipulation and consistency of data presentation, a tape conversion program was used to translate Haystack data tapes to a format compatible with the FCRAO data reduction programs. All averaging and processing of Haystack data was therefore performed at FCRAO.

Calibration of Haystack 43 GHz data was treated in a manner similar to the (non-chopper wheel) calibration of FCRAO data described above. Availability of a calibration noise tube permitted measurement of the receiver temperature at frequent intervals (usually every 10 minutes). The atmospheric opacity τ_o was computed several times a day by the on-line program using surface measurements of temperature, atmospheric pressure, and water vapor density. As at FCRAO, these values ranged from 0.09 to 0.20 in reasonable observing weather. An empirical telescope gain curve was used to scale the spectra for the elevation dependence of the telescope gain at 43 GHz. Antenna temperatures corrected for atmospheric attenuation and telescope gain were converted to flux densities using a conversion factor of 66 Jy/K. The

low aperture efficiency applicable at this frequency ($\eta_A \leq 0.09$) is due primarily to radome attenuation. The overall uncertainty of the Haystack calibration is estimated to be ~15%, except on a few observations where pointing was a likely source of larger errors.

§3. Results

A general description of the results from the SiO time monitoring program is presented in this section, while a more detailed discussion of the implications of these results follows in Chapter IV. First, a general description of the properties of the SiO emission will be given, noting both similarities and differences between observed sources and between various transitions. Then the time variability will be examined in greater detail and properties of the SiO emission will be compared with the stellar light curves. In all tables and figures which follow in this chapter, sources are arranged in order of increasing period, followed by the non-periodic sources VY CMa and Orion.

Figure 5(a-m) presents the individual SiO spectra for thirteen sources in the 43 GHz transitions (J=1-0, v=1; v=2; v=3), while Figure 6(a-m) shows the 86 GHz data (J=2-1, v=1). The date of observation and the corresponding optical phase (ϕ_v) are indicated on each panel. The optical phases were computed from visual data kindly provided by J. Mattei of the American Association of Variable Star Observers. It should be noted that the flux density scale for the 43 GHz data may vary

Figure 5(a-m). SiO monitoring data for thirteen sources in the J=1-0 (v = 1, 2, 3) transitions. Sources are arranged in order of increasing period (followed by the non-periodic sources VY CMa and Orion), with from one to three pages per source. The date of observation and the corresponding optical phase (ϕ) are shown at the top of each panel. The vertical line marks the stellar velocity. The vibrational level (v) for the rotational transition is shown at the far right. Spectra are from FCRAO, except for those from Mar. 1979, Aug. 1979, Aug. 1980, Nov. 1980, and Mar. 1981, which are from Haystack; data from Aug. 1980 and Mar. 1981 were obtained in collaboration with D. Buhl and G. Chin.

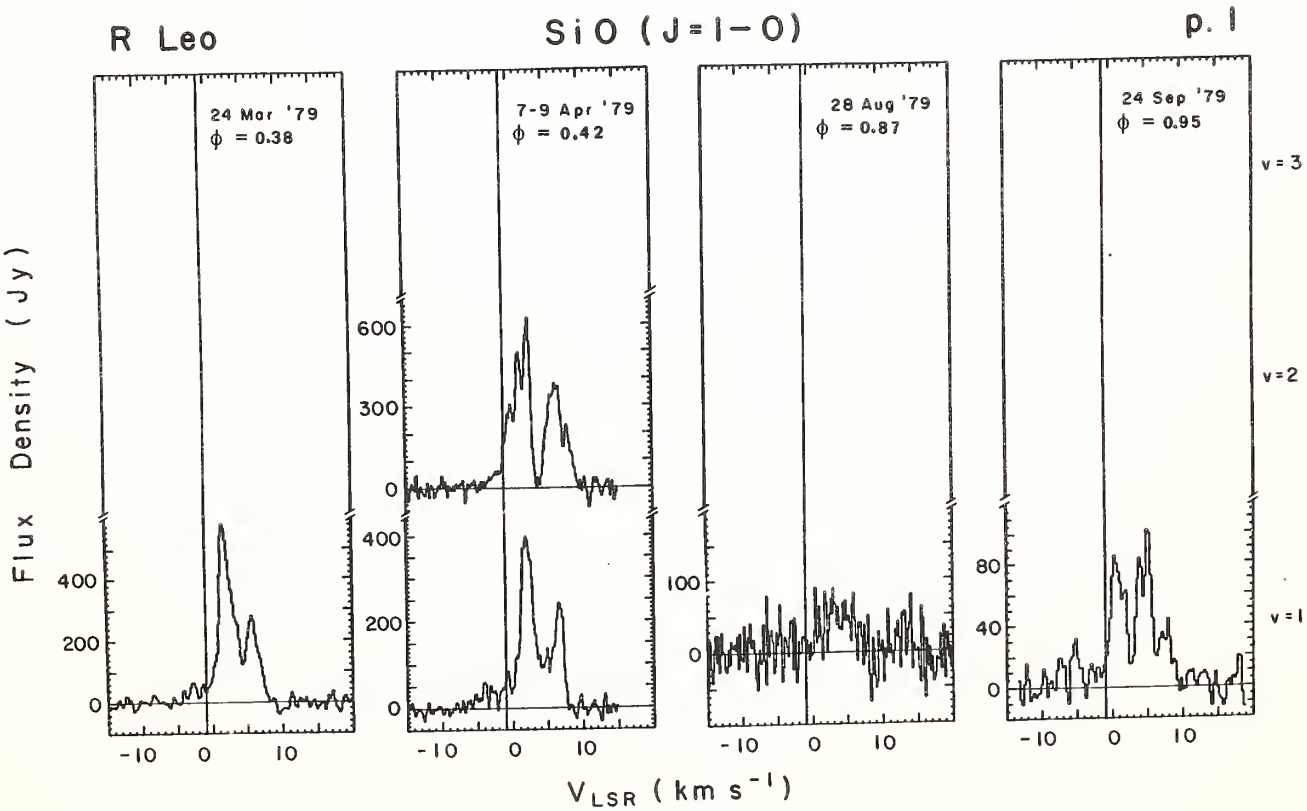
R Leo
SiO (J=1−0)
p. 1
24 Mar '79
ϕ = 0.38
7-9 Apr '79
ϕ = 0.42
28 Aug '79
ϕ = 0.87
24 Sep '79
ϕ = 0.95
v = 3
v = 2
v = 1
Flux Density (Jy)
600
300
0
400
200
0
100
0
80
40
0
-10
0
10
V_{LSR} (km s^{-1})

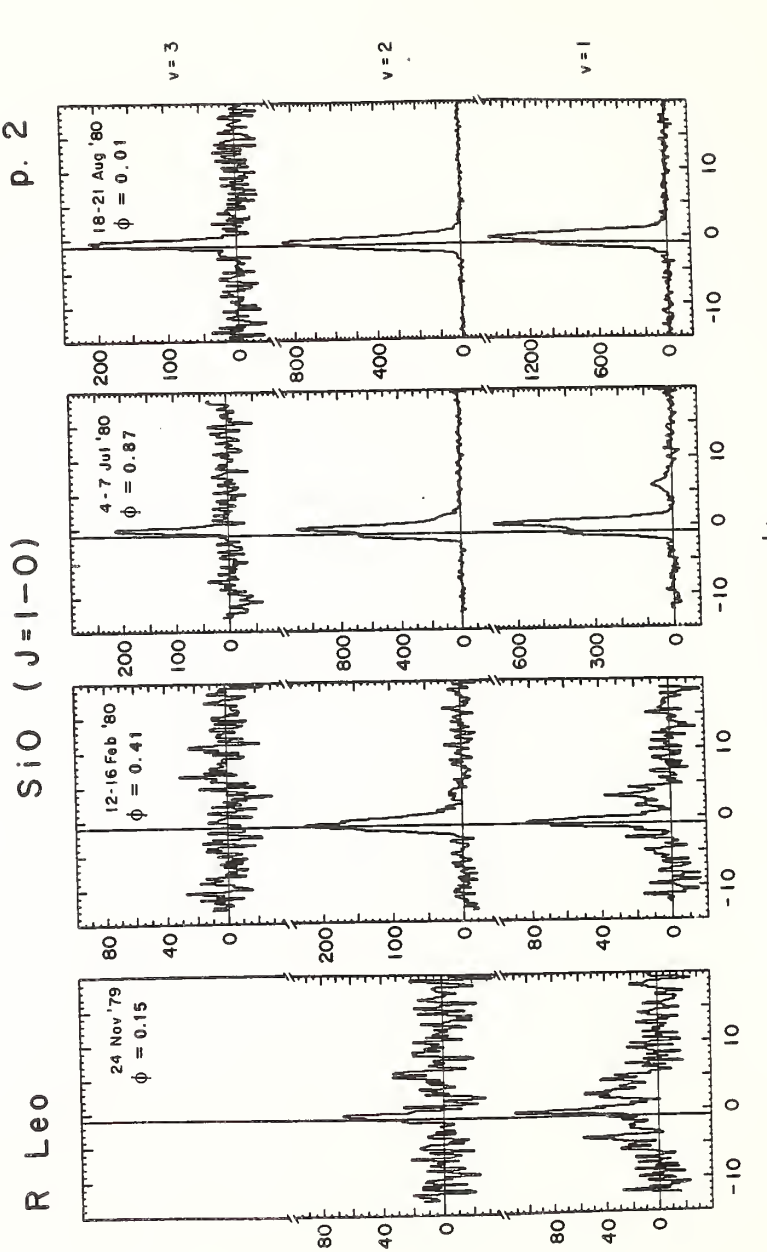
R Leo
SiO (J=1-0)
p. 2
24 Nov '79
φ = 0.15
12-16 Feb '80
φ = 0.41
4-7 Jul '80
φ = 0.87
18-21 Aug '80
φ = 0.01
v = 3
v = 2
v = 1
FLUX DENSITY (Jy)
V_LSR (km s^-1)

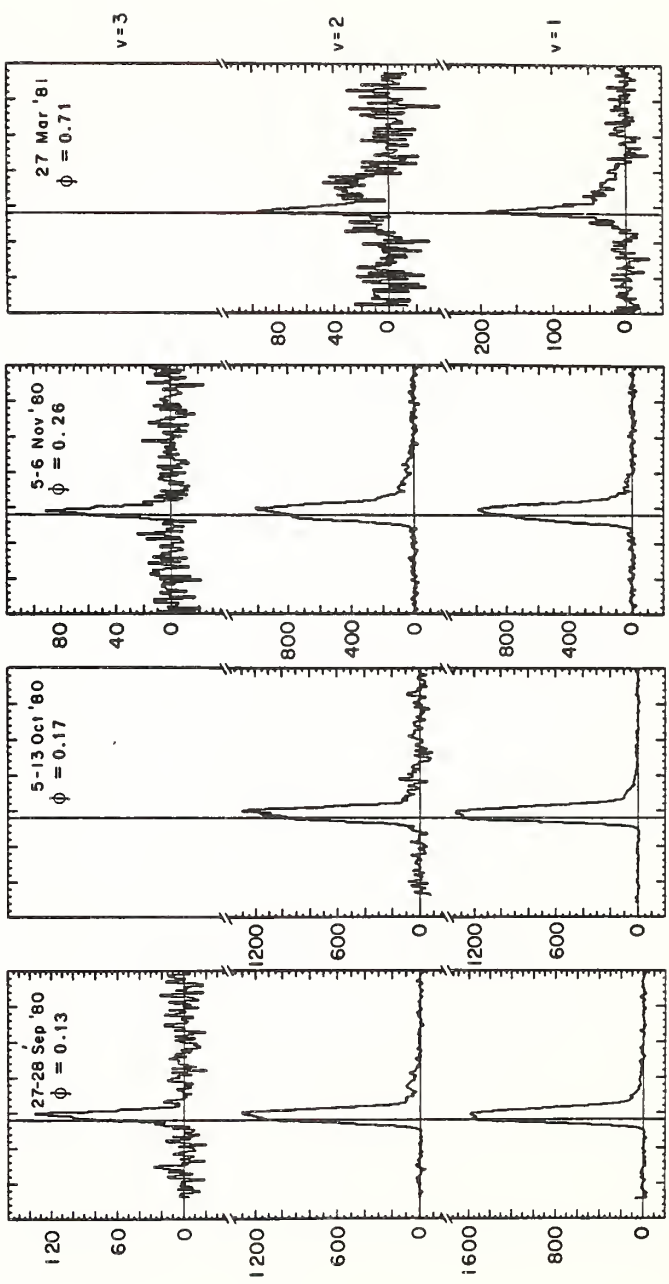
R Leo
SiO(J=1-0)
p. 3
27-28 Sep '80
φ = 0.13
5-13 Oct '80
φ = 0.17
5-6 Nov '80
φ = 0.26
27 Mar '81
φ = 0.71
v=3
v=2
v=1
Flux Density (Jy)
V_LSR (km s^-1)

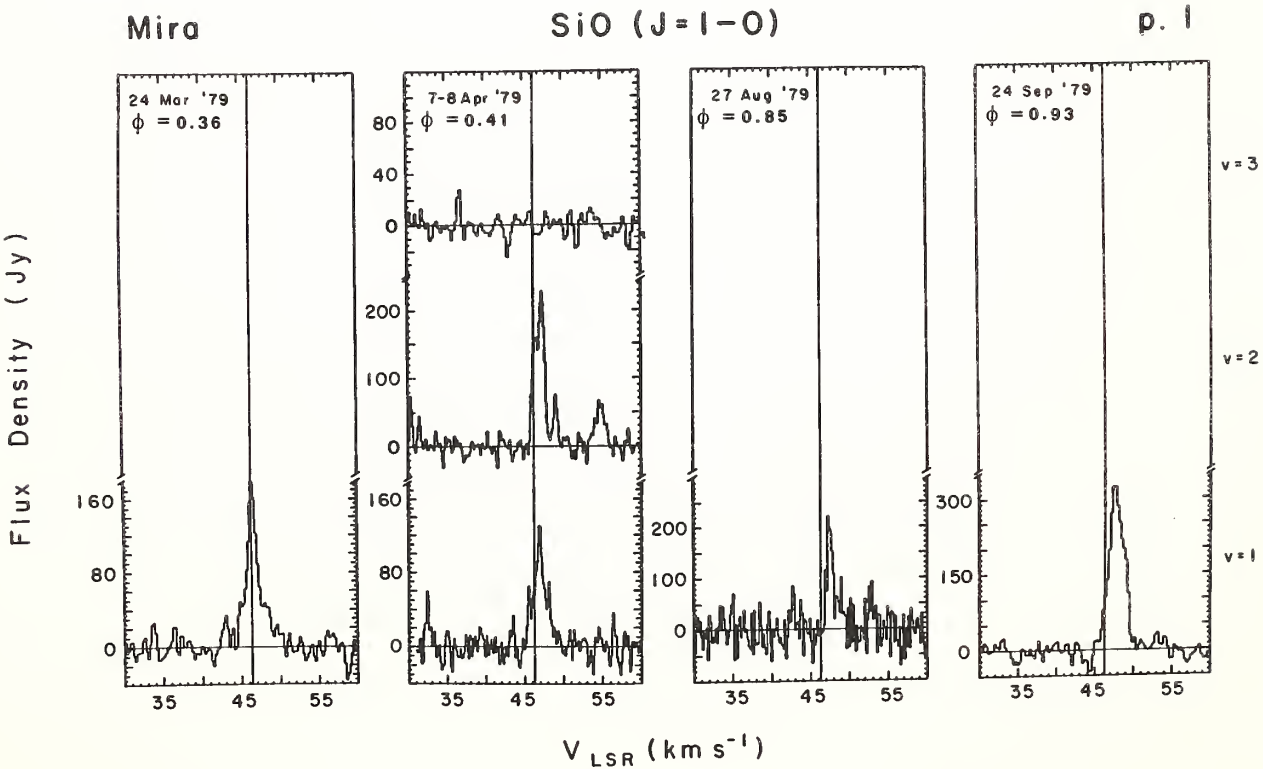
Mira
SiO (J=1−0)
p. 1
24 Mar '79
ϕ = 0.36
7-8 Apr '79
ϕ = 0.41
27 Aug '79
ϕ = 0.85
24 Sep '79
ϕ = 0.93
v=3
v=2
v=1
Flux Density (Jy)
V LSR (km s⁻¹)
35
45
55
0
80
40
100
150
200
300
160

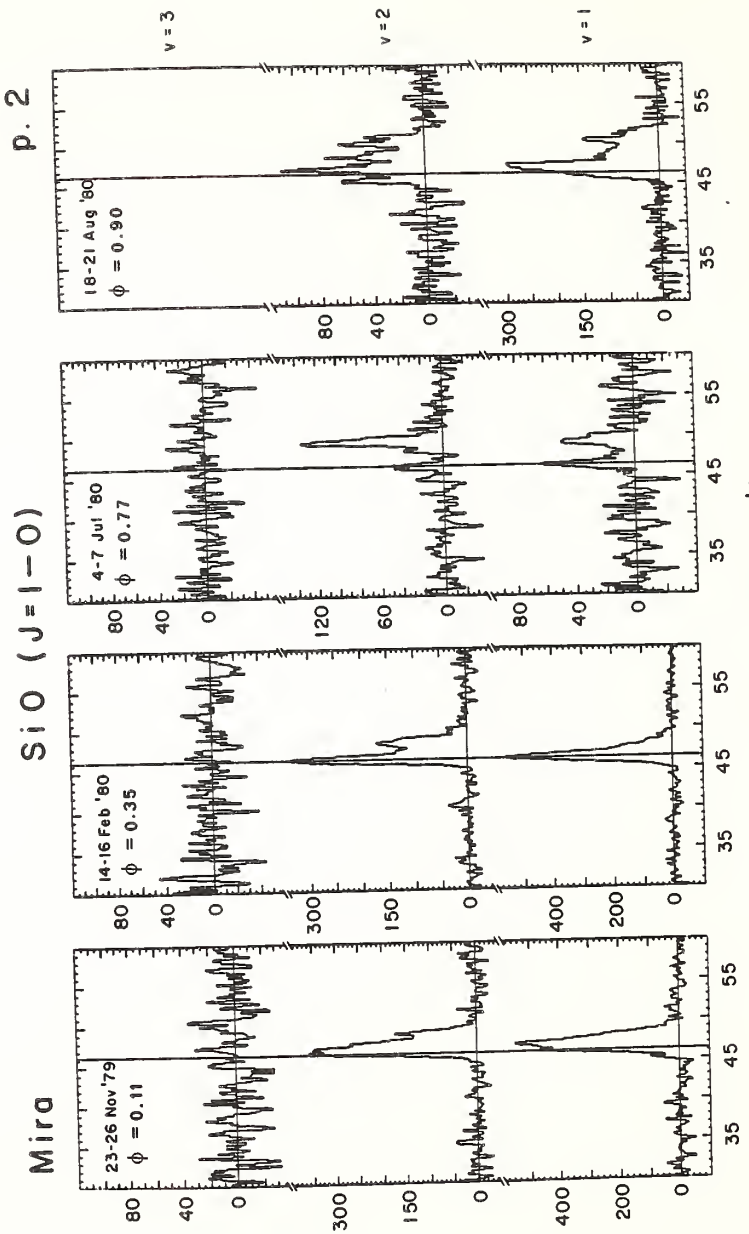
Mira
SiO (J=1−0)
p. 2
v = 3
v = 2
v = 1
23-26 Nov '79
φ = 0.11
14-16 Feb '80
φ = 0.35
4-7 Jul '80
φ = 0.77
18-21 Aug '80
φ = 0.90
FLUX DENSITY (Jy)
V LSR (km s⁻¹)

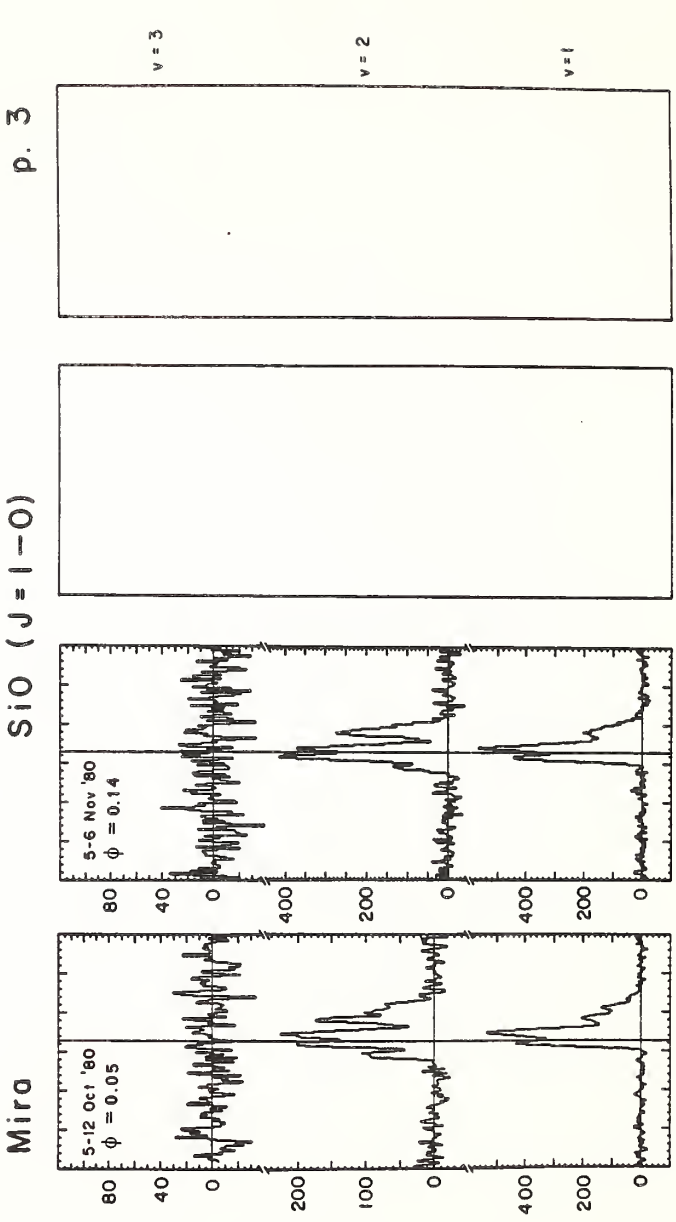
Mira
SiO (J = 1−0)
p. 3
5-12 Oct '80
φ = 0.05
5-6 Nov '80
φ = 0.14
v = 3
v = 2
v = 1
Flux Density (Jy)
V LSR (km s⁻¹)

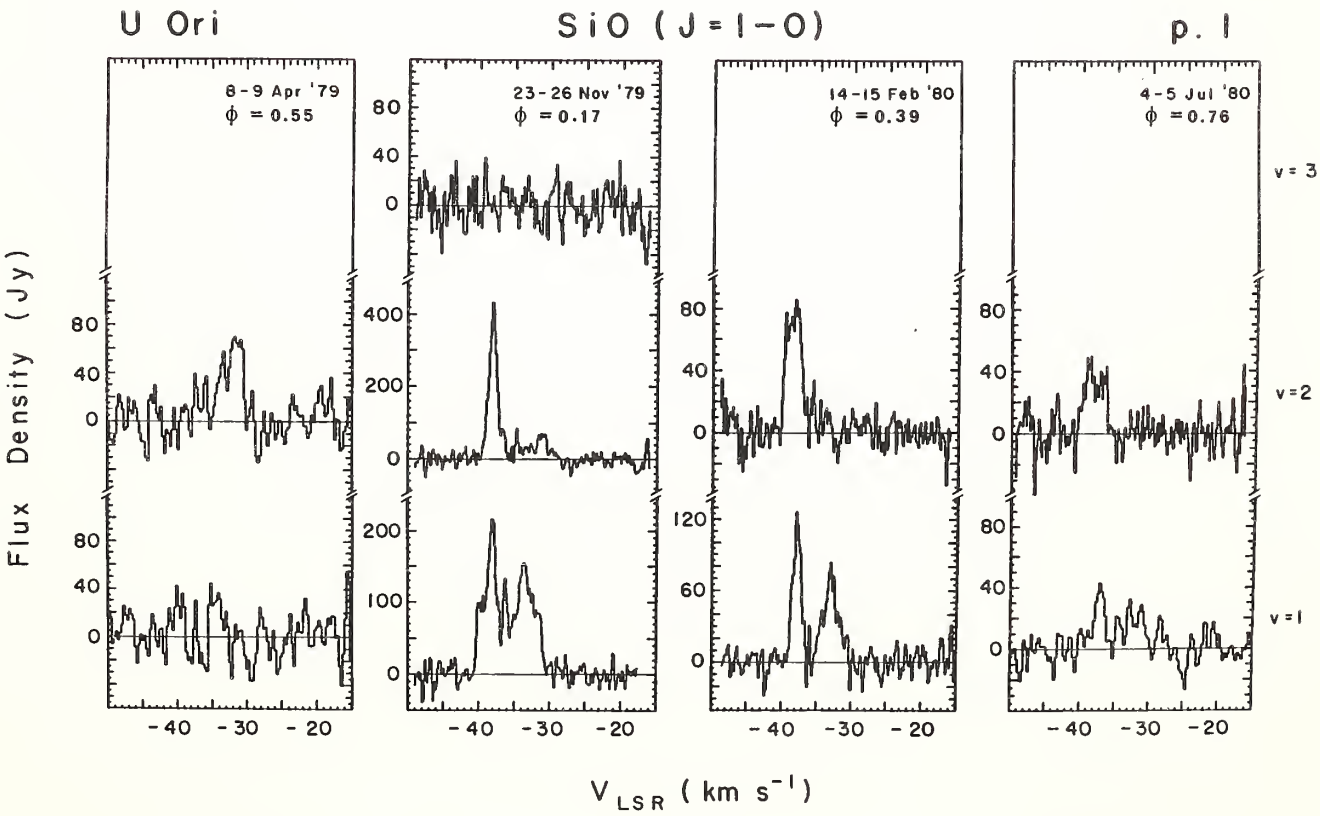
U Ori
SiO (J=1-0)
p. 1
8-9 Apr '79
φ = 0.55
23-26 Nov '79
φ = 0.17
14-15 Feb '80
φ = 0.39
4-5 Jul '80
φ = 0.76
v = 3
v = 2
v = 1
Flux Density (Jy)
V LSR (km s⁻¹)
-40 -30 -20

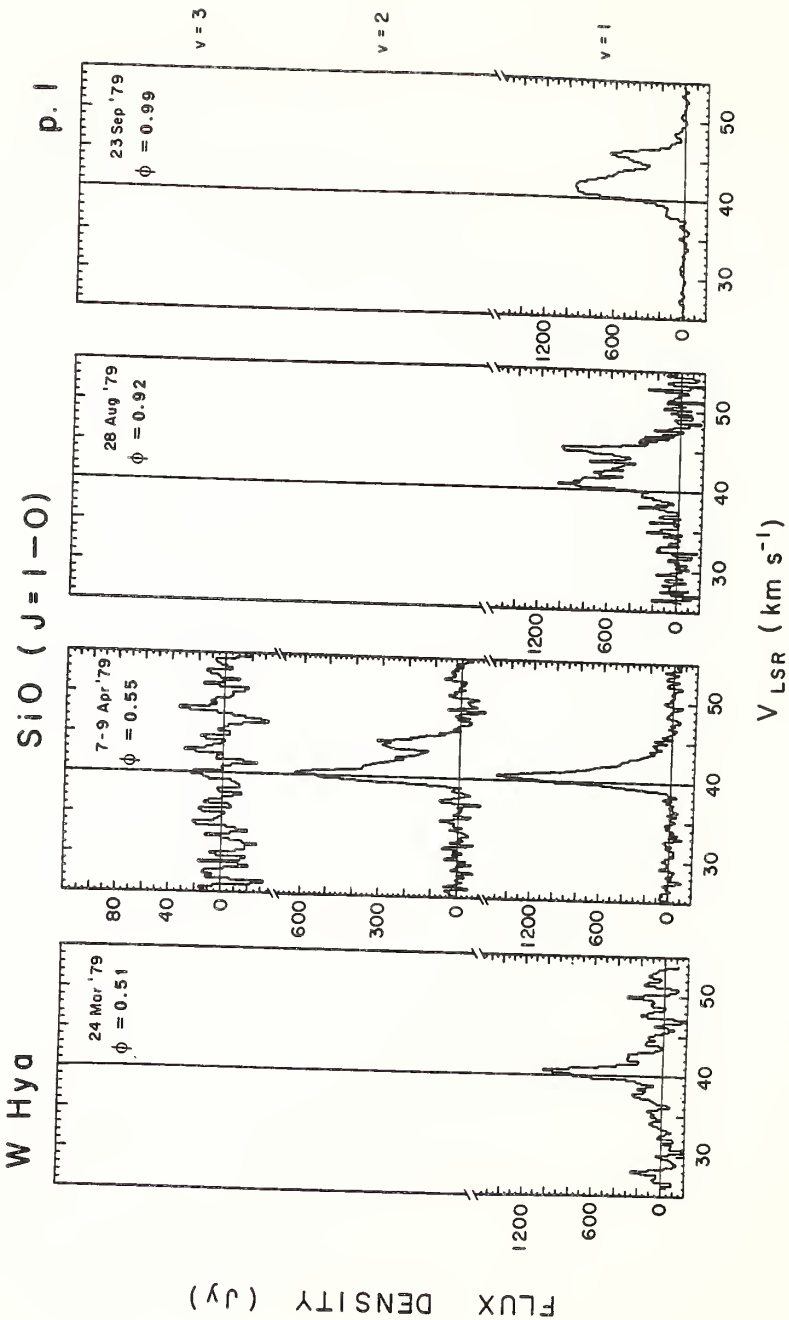
W Hya
SiO (J=1−0)
p. 1
v = 3
v = 2
v = 1
24 Mar '79
φ = 0.51
7-9 Apr '79
φ = 0.55
28 Aug '79
φ = 0.92
23 Sep '79
φ = 0.99
FLUX DENSITY (Jy)
V LSR (km s⁻¹)

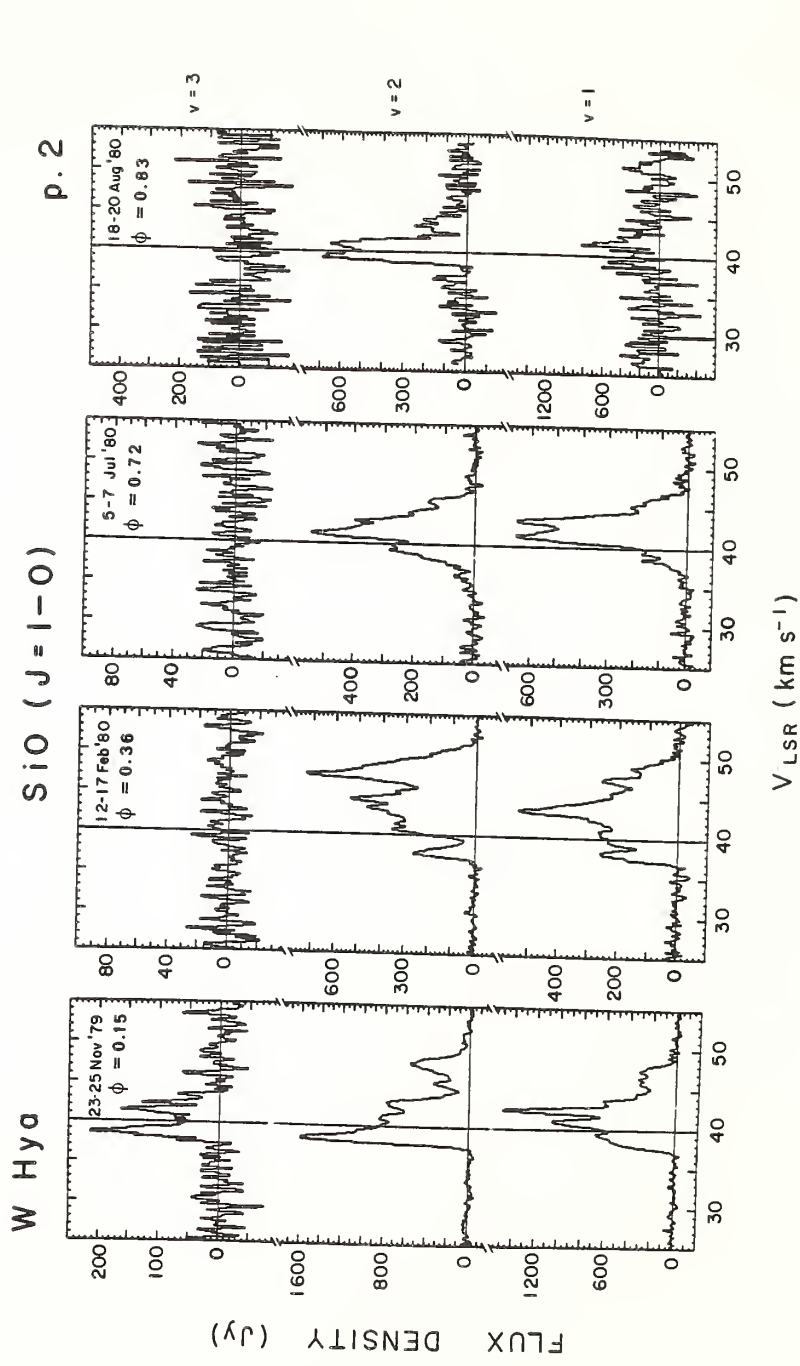
W Hya
SiO (J=1-0)
p. 2
v = 3
v = 2
v = 1
23-25 Nov '79
φ = 0.15
12-17 Feb '80
φ = 0.36
5-7 Jul '80
φ = 0.72
18-20 Aug '80
φ = 0.83
FLUX DENSITY (Jy)
V LSR (km s⁻¹)

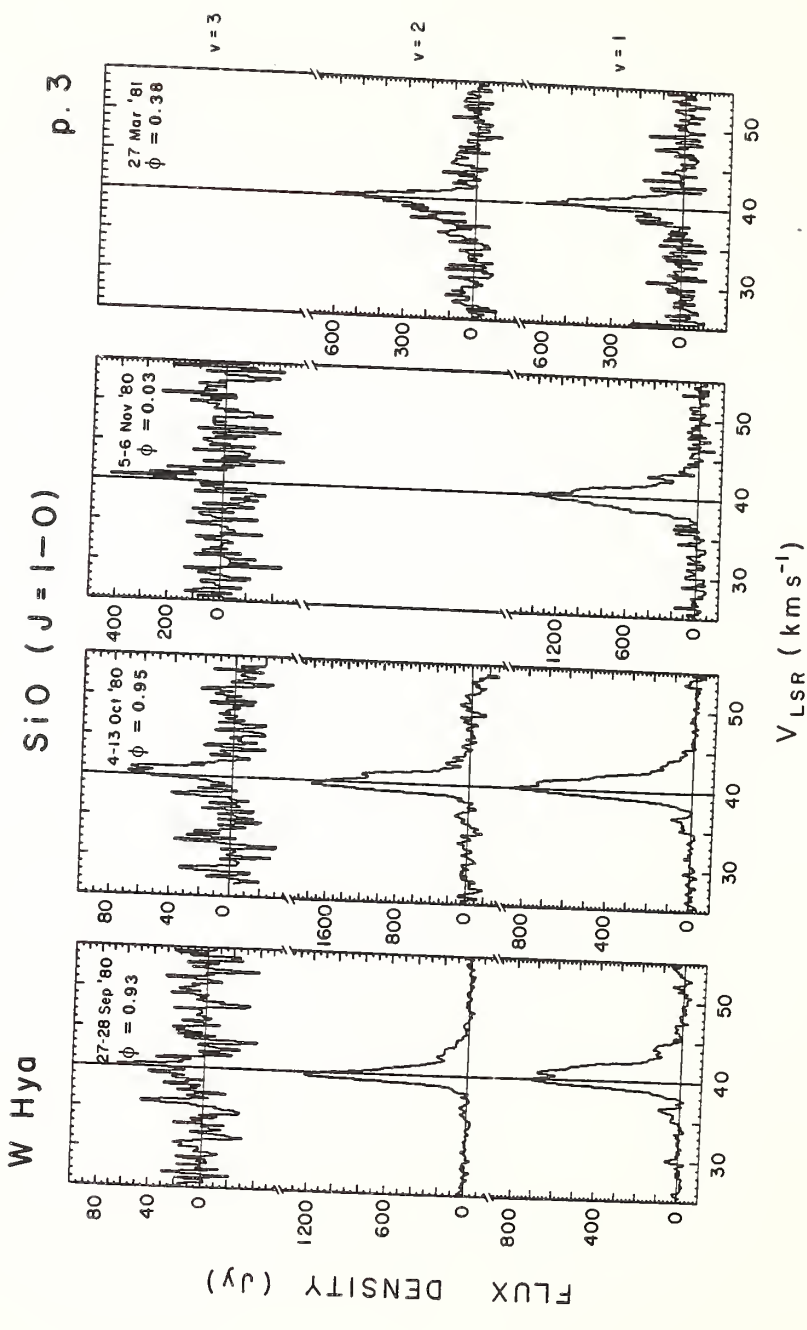
W Hya
SiO (J = 1–0)
p. 3
27-28 Sep '80
φ = 0.93
4-13 Oct '80
φ = 0.95
5-6 Nov '80
φ = 0.03
27 Mar '81
φ = 0.38
v = 3
v = 2
v = 1
FLUX DENSITY (Jy)
V LSR (km s⁻¹)

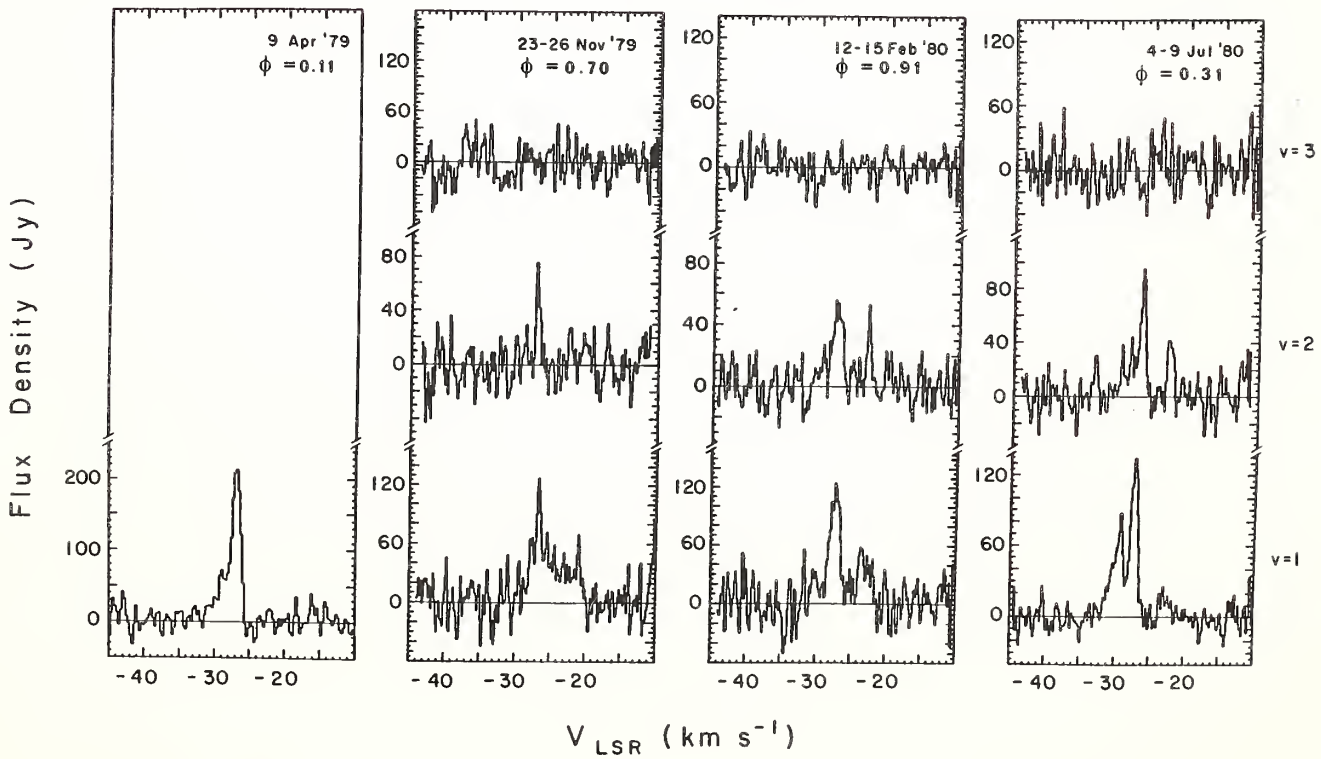
R Aqr
SiO (J=1–0)
p. 1
9 Apr '79
ϕ = 0.11
23-26 Nov '79
ϕ = 0.70
12-15 Feb '80
ϕ = 0.91
4-9 Jul '80
ϕ = 0.31
v=3
v=2
v=1
Flux Density (Jy)
V LSR (km s⁻¹)

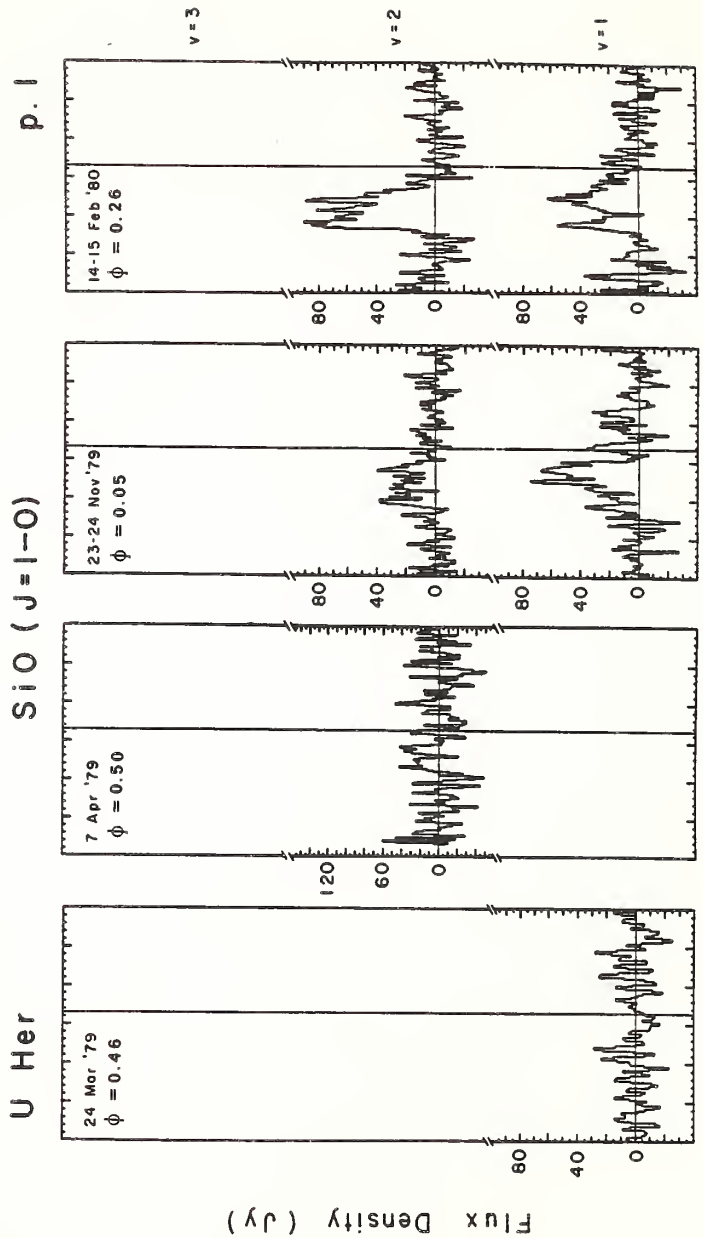
U Her
SiO (J=1–0)
p. 1
v=3
v=2
v=1
24 Mar '79
φ = 0.46
7 Apr '79
φ = 0.50
23-24 Nov '79
φ = 0.05
14-15 Feb '80
φ = 0.26
Flux Density (Jy)
V LSR (km s⁻¹)

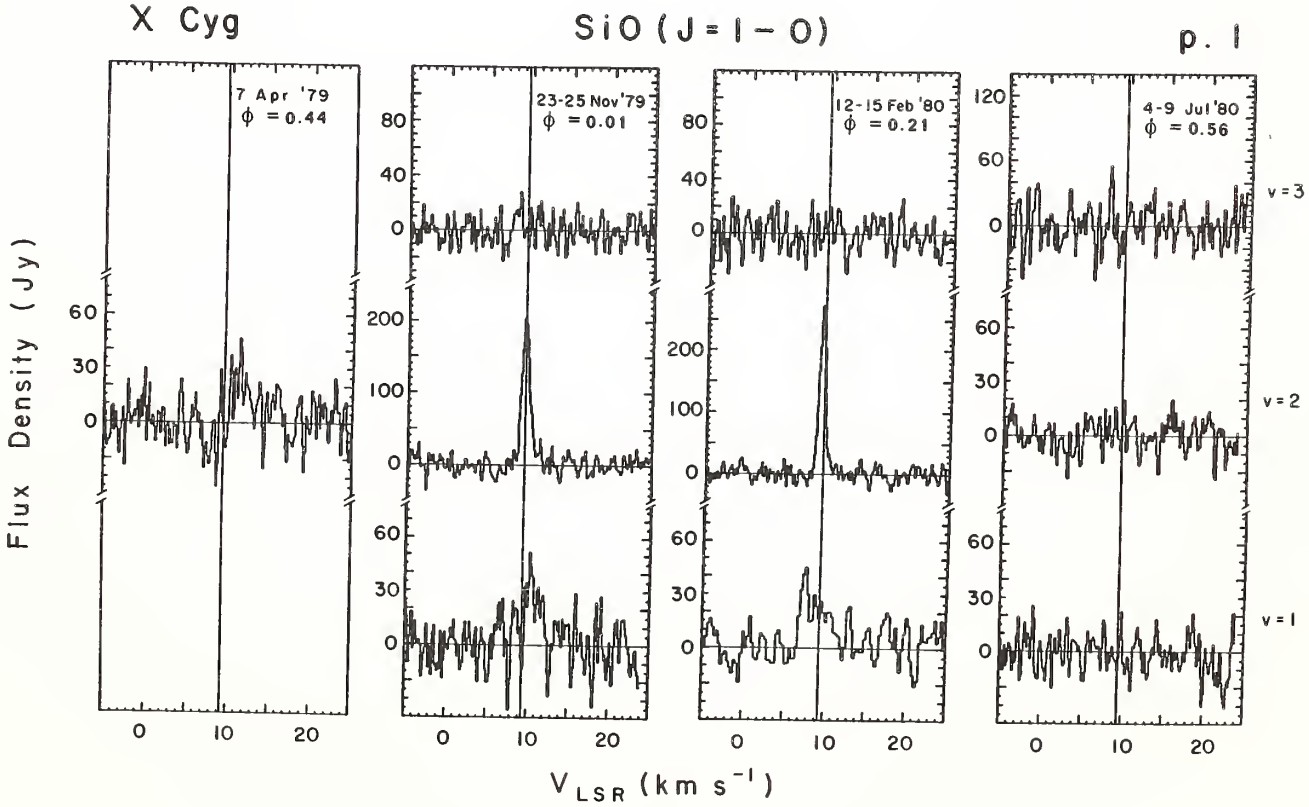
X Cyg
SiO (J = 1 − 0)
p. 1
7 Apr '79
ϕ = 0.44
23-25 Nov'79
ϕ = 0.01
12-15 Feb '80
ϕ = 0.21
4-9 Jul'80
ϕ = 0.56
v = 3
v = 2
v = 1
Flux Density (Jy)
V LSR (km s⁻¹)

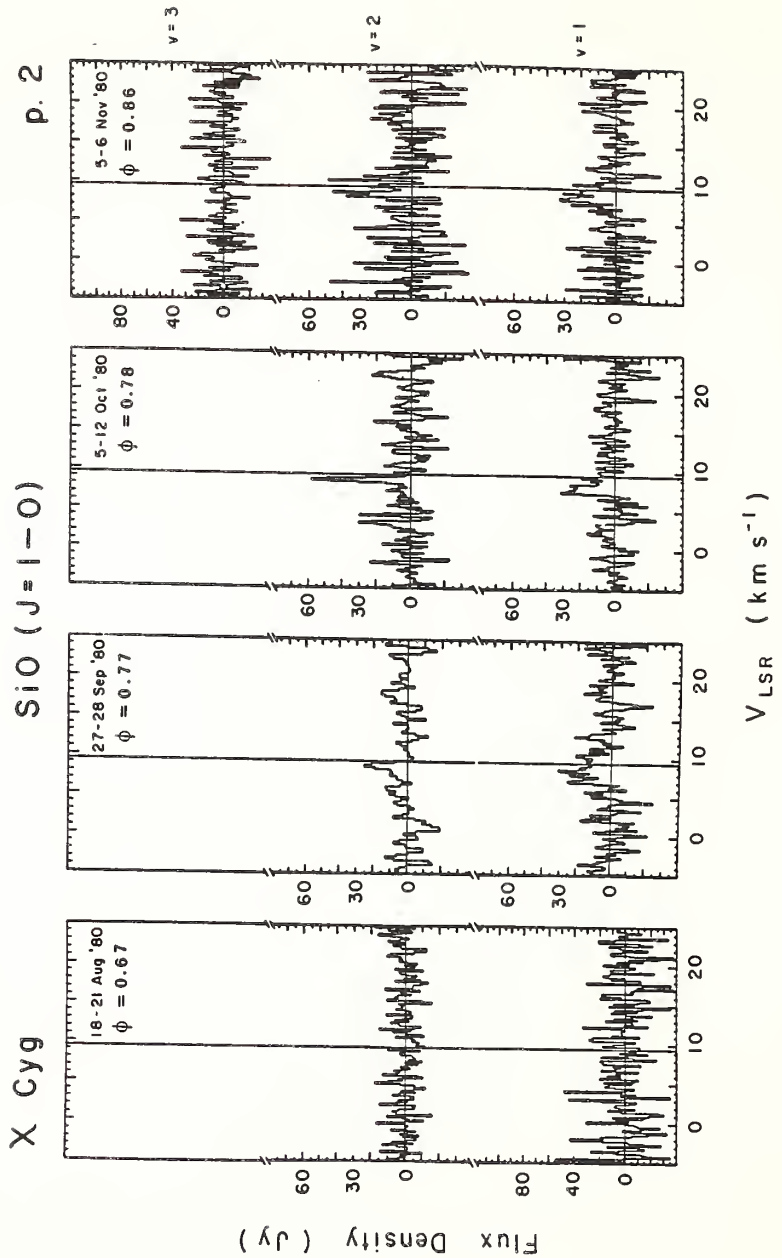
X Cyg
SiO (J=1−0)
p. 2
18-21 Aug '80
φ = 0.67
27-28 Sep '80
φ = 0.77
5-12 Oct '80
φ = 0.78
5-6 Nov '80
φ = 0.86
v = 3
v = 2
v = 1
Flux Density (Jy)
V LSR (km s⁻¹)

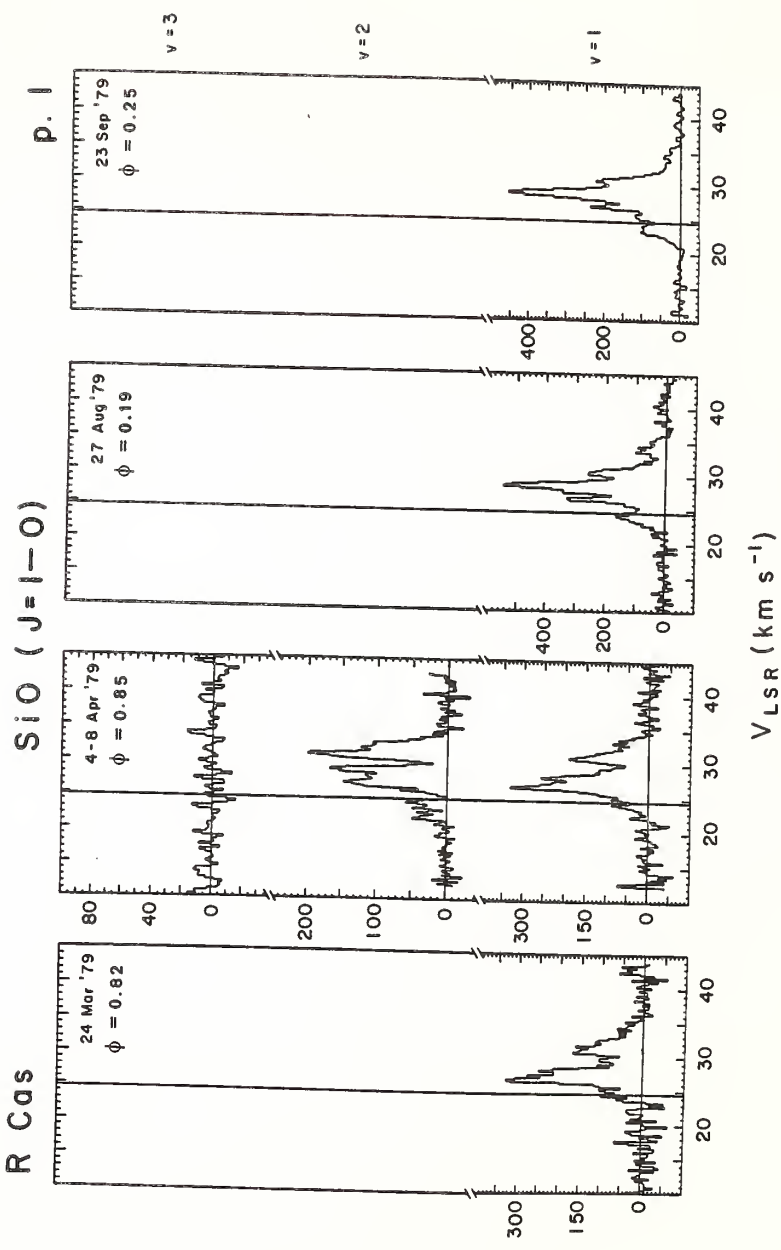
R Cas
SiO (J=1−0)
p. l
24 Mar '79
φ = 0.82
4-8 Apr '79
φ = 0.85
27 Aug '79
φ = 0.19
23 Sep '79
φ = 0.25
v = 3
v = 2
v = 1
FLUX DENSITY (Jy)
V LSR (km s⁻¹)

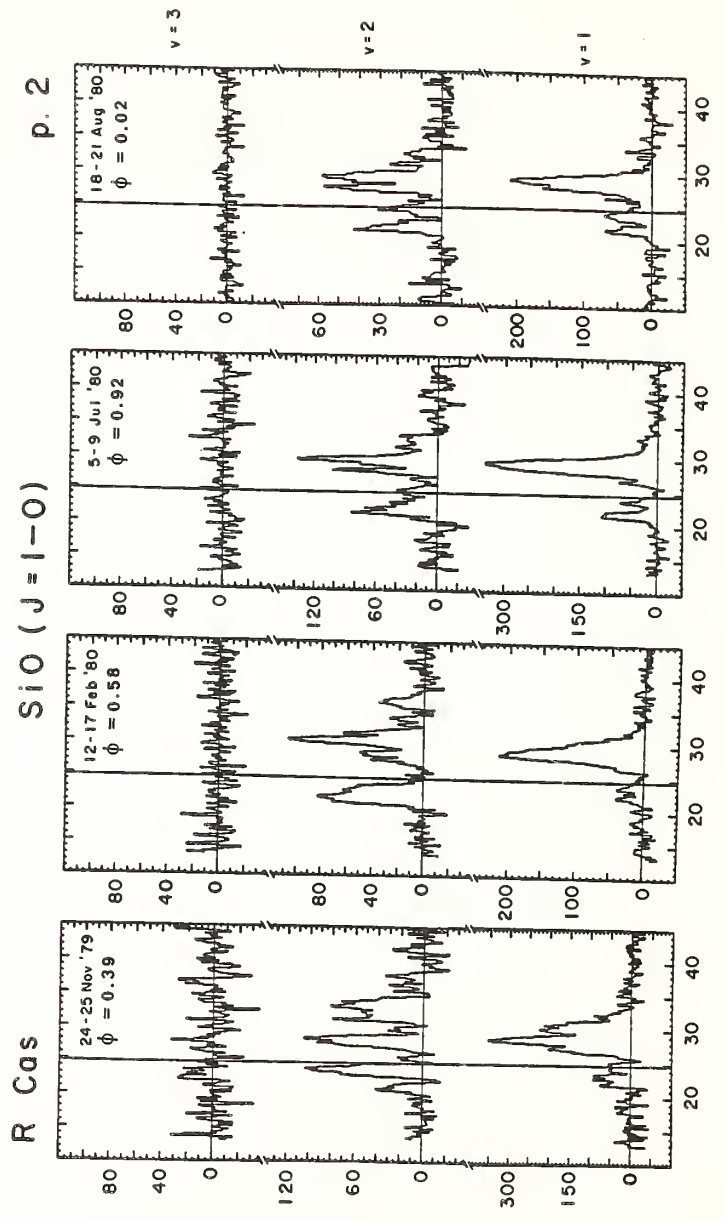
R Cas
SiO (J=1-0)
p. 2
24-25 Nov '79
φ = 0.39
12-17 Feb '80
φ = 0.58
5-9 Jul '80
φ = 0.92
18-21 Aug '80
φ = 0.02
v=3
v=2
v=1
Flux Density (Jy)
VLSR (km s-1)

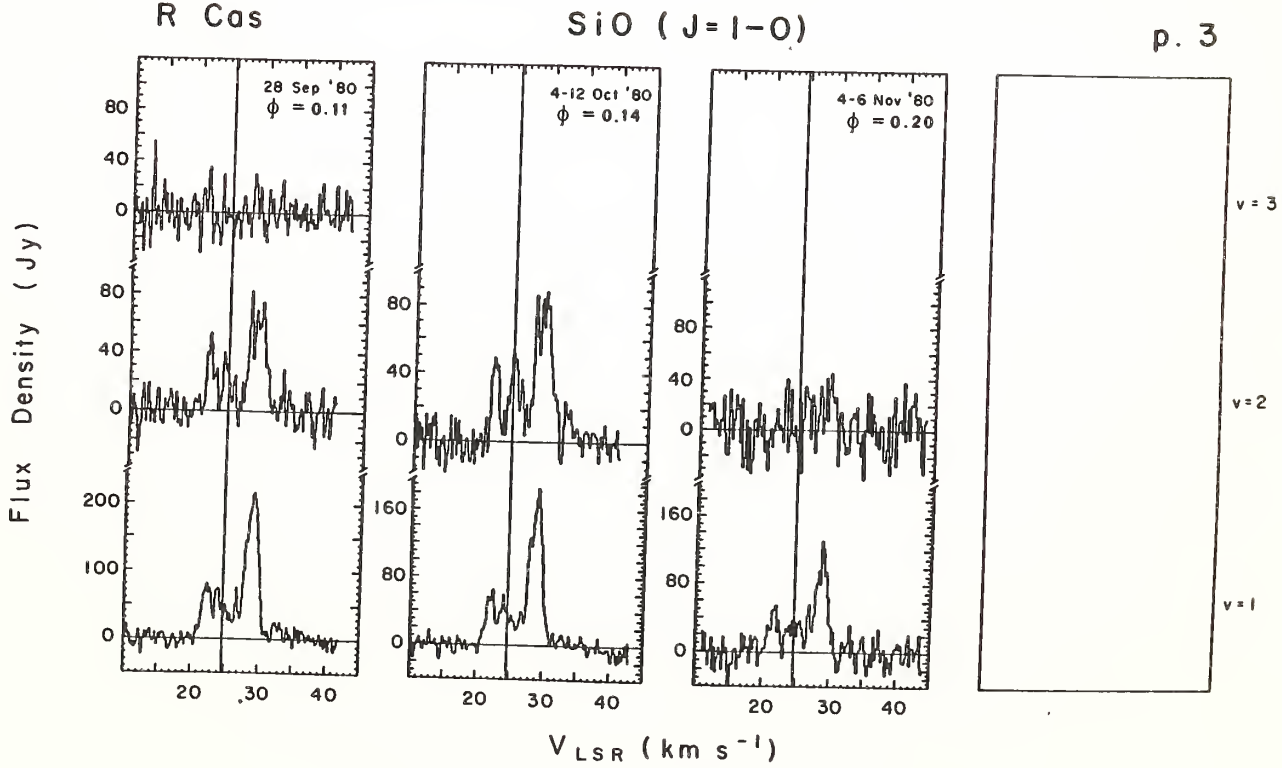
R Cas
SiO (J=1-0)
p. 3
28 Sep '80
ϕ = 0.11
4-12 Oct '80
ϕ = 0.14
4-6 Nov '80
ϕ = 0.20
v = 3
v = 2
v = 1
Flux Density (Jy)
V LSR (km s⁻¹)

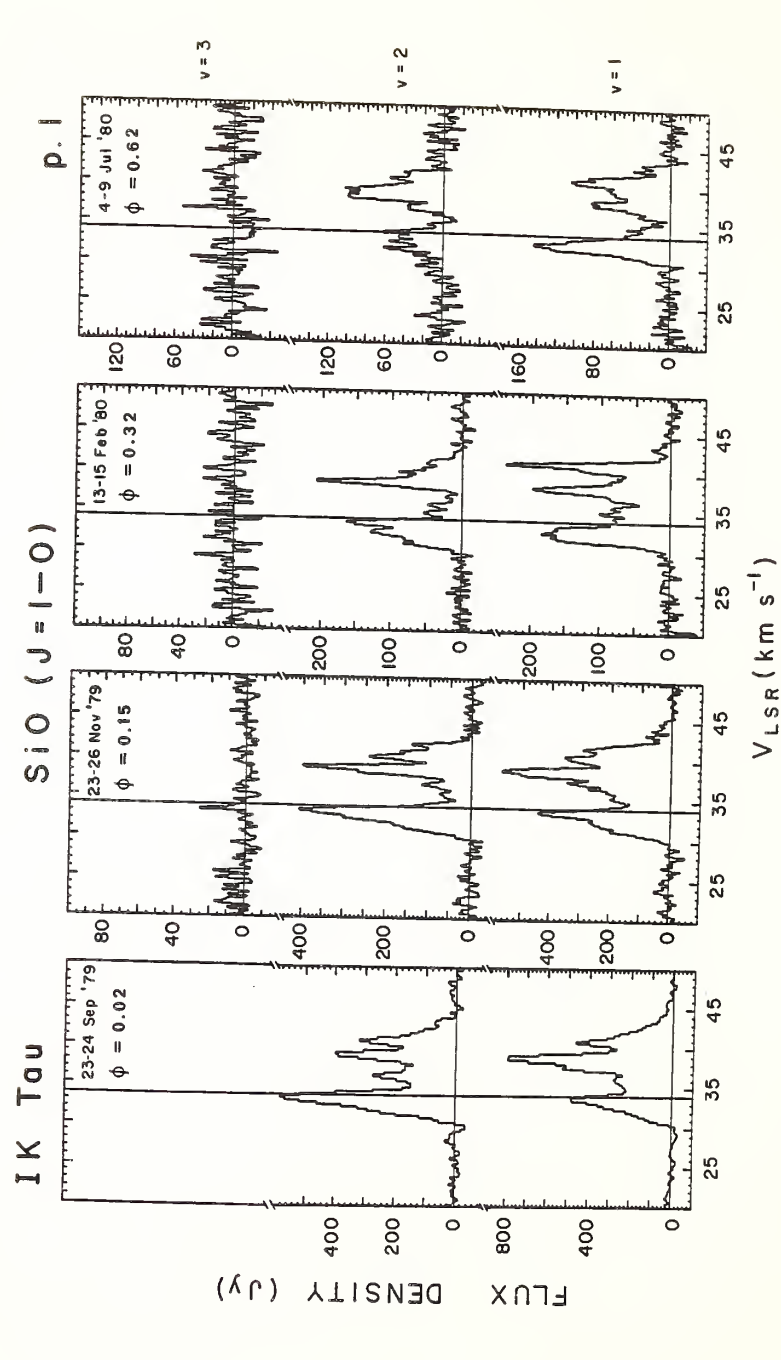
IK Tau
SiO (J = 1−0)
p. I
23-24 Sep '79
φ = 0.02
23-26 Nov '79
φ = 0.15
13-15 Feb '80
φ = 0.32
4-9 Jul '80
φ = 0.62
v = 3
v = 2
v = 1
FLUX DENSITY (Jy)
V LSR (km s⁻¹)

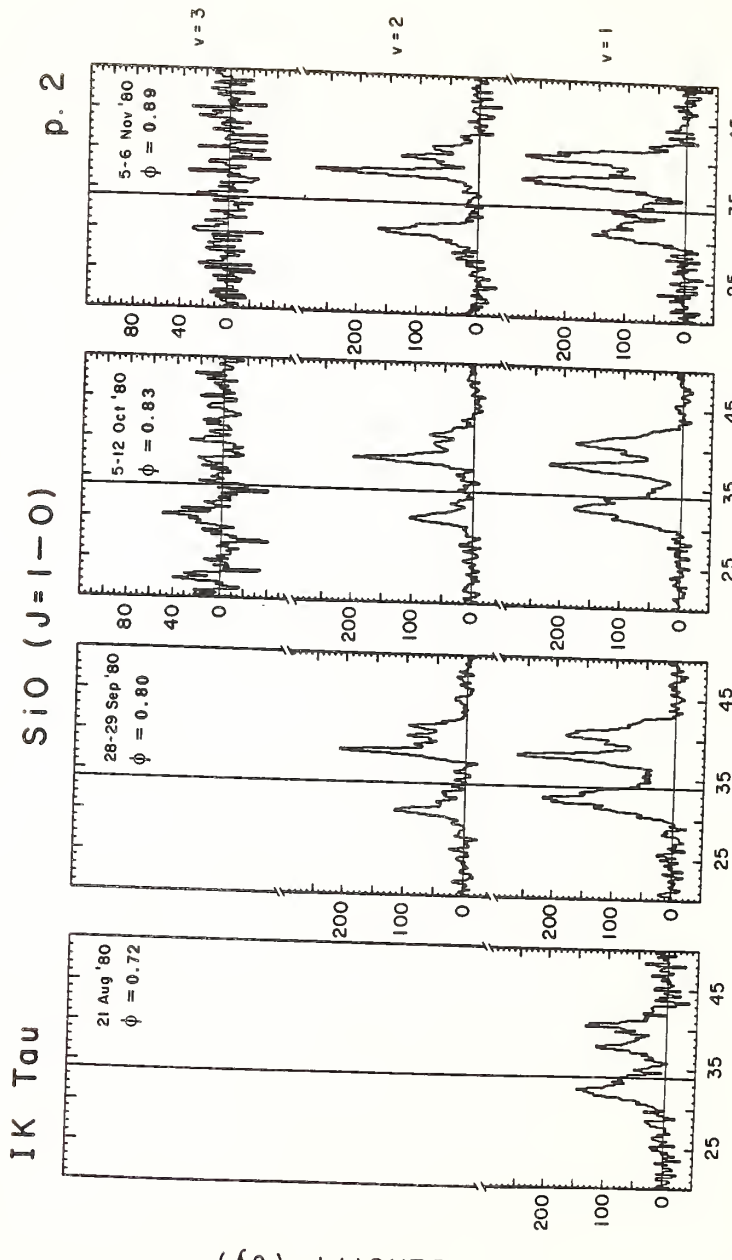
IK Tau
SiO (J=1−0)
p. 2
21 Aug '80
φ = 0.72
28-29 Sep '80
φ = 0.80
5-12 Oct '80
φ = 0.83
5-6 Nov '80
φ = 0.89
v = 3
v = 2
v = 1
FLUX DENSITY (Jy)
V LSR (km s⁻¹)

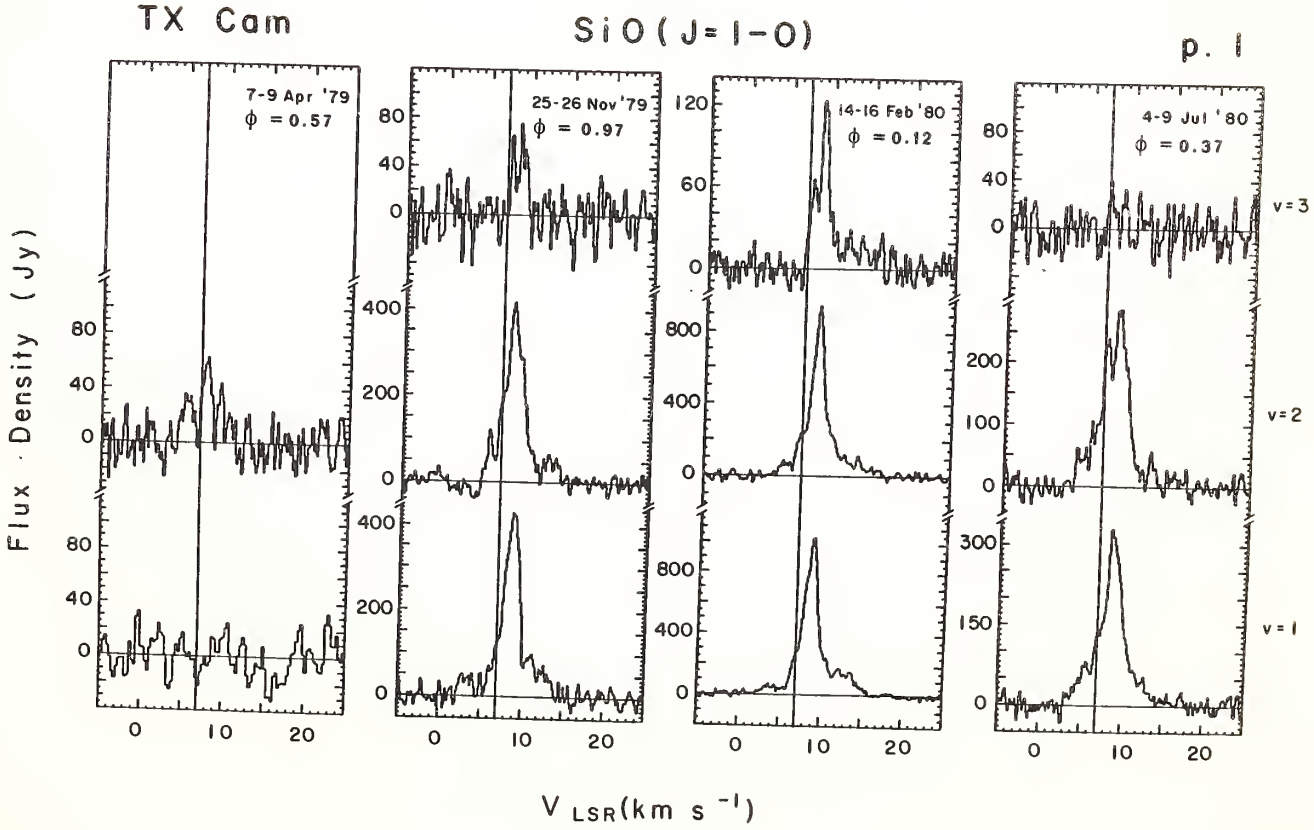
TX Cam
SiO (J=1-0)
p. 1
7-9 Apr '79
ϕ = 0.57
25-26 Nov '79
ϕ = 0.97
14-16 Feb '80
ϕ = 0.12
4-9 Jul '80
ϕ = 0.37
v=3
v=2
v=1
Flux Density (Jy)
V LSR (km s -1)

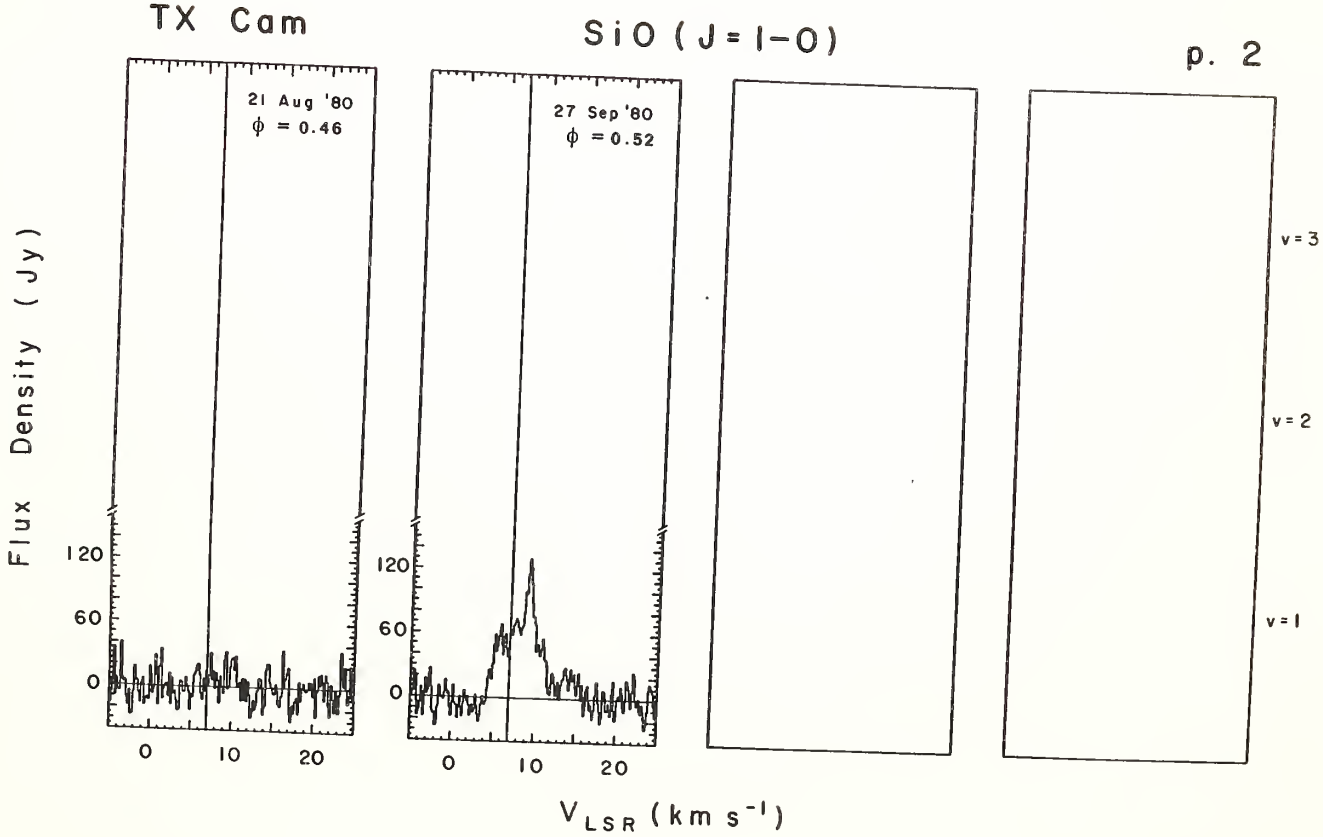
TX Cam
SiO (J=1-0)
p. 2
21 Aug '80
φ = 0.46
27 Sep '80
φ = 0.52
v=3
v=2
v=1
120
60
0
0
10
20
Flux Density (Jy)
V LSR (km s⁻¹)

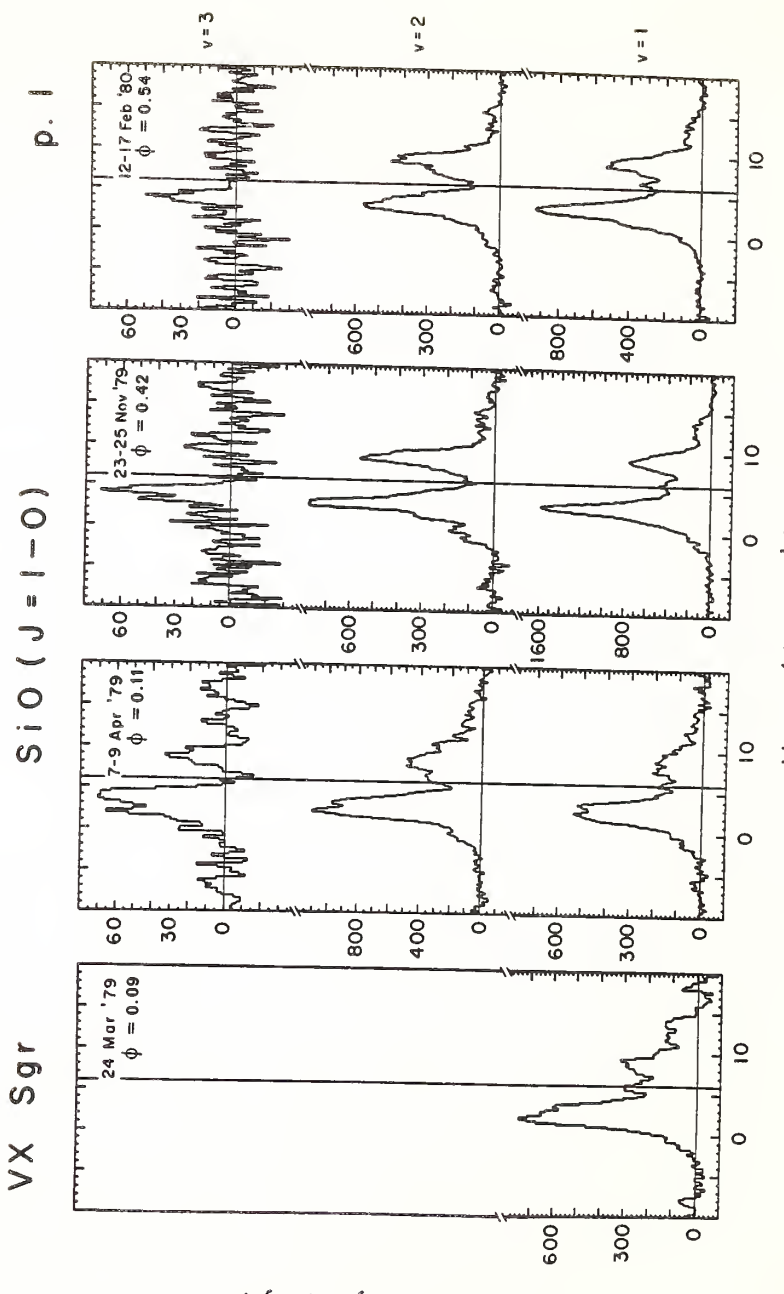
VX Sgr
SiO (J = 1 − 0)
p. 1
24 Mar '79
φ = 0.09
7-9 Apr '79
φ = 0.11
23-25 Nov '79
φ = 0.42
12-17 Feb '80
φ = 0.54
v = 3
v = 2
v = 1
Flux Density (Jy)
V LSR (km s⁻¹)

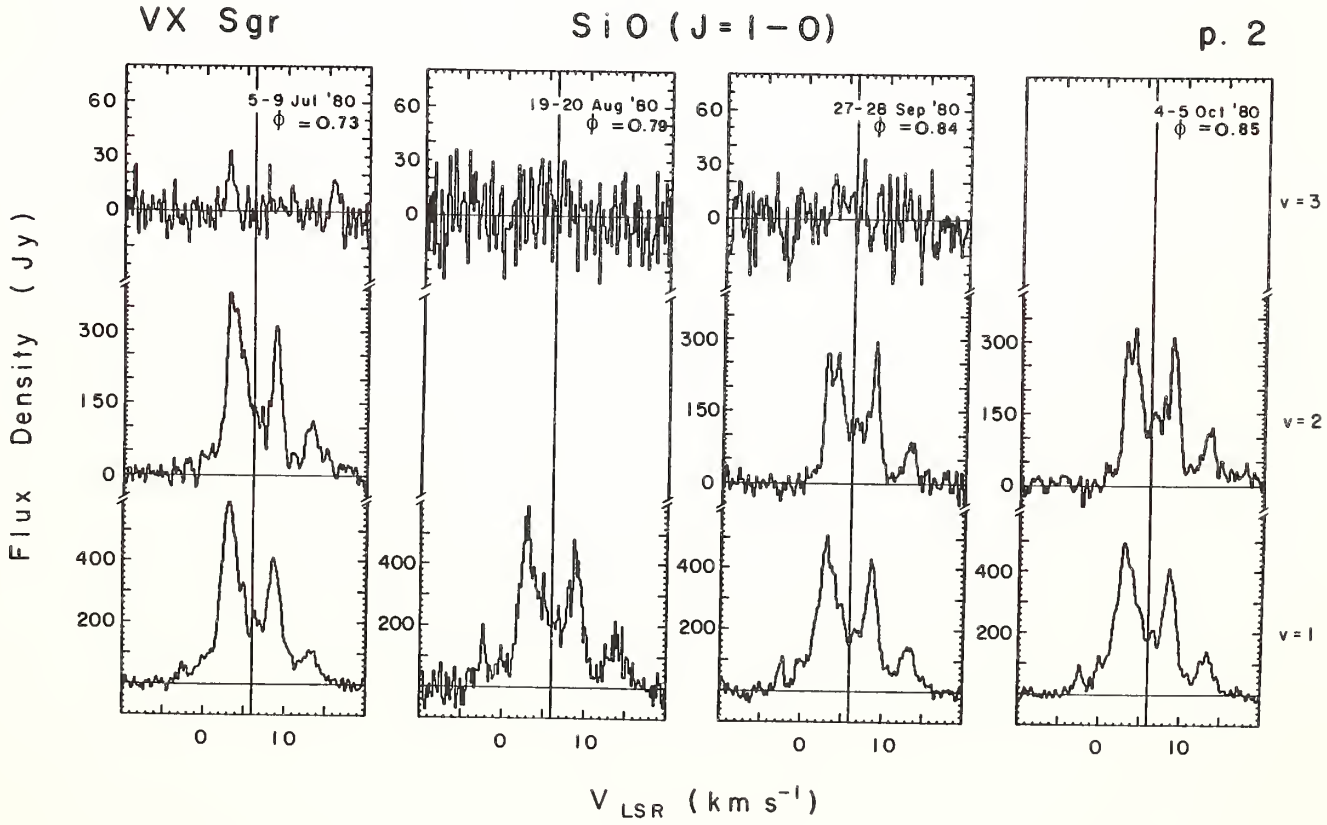
VX Sgr
SiO (J=1−0)
p. 2
5-9 Jul '80
φ =0.73
19-20 Aug '80
φ =0.79
27-28 Sep '80
φ =0.84
4-5 Oct '80
φ =0.85
v = 3
v = 2
v = 1
Flux Density (Jy)
V LSR (km s⁻¹)

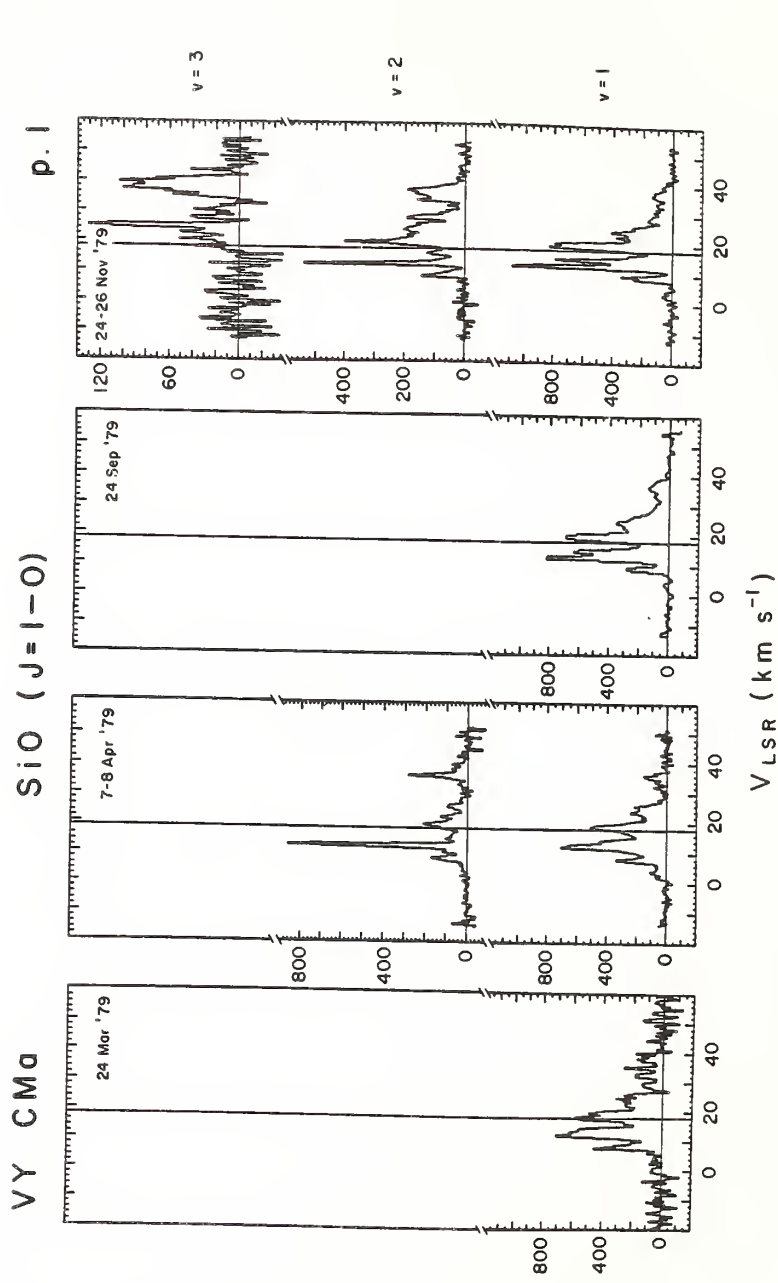
VY CMa
SiO (J=1-0)
p.1
24 Mar '79
7-8 Apr '79
24 Sep '79
24-26 Nov '79
v=3
v=2
v=1
FLUX DENSITY (Jy)
V_{LSR} (km s^{-1})

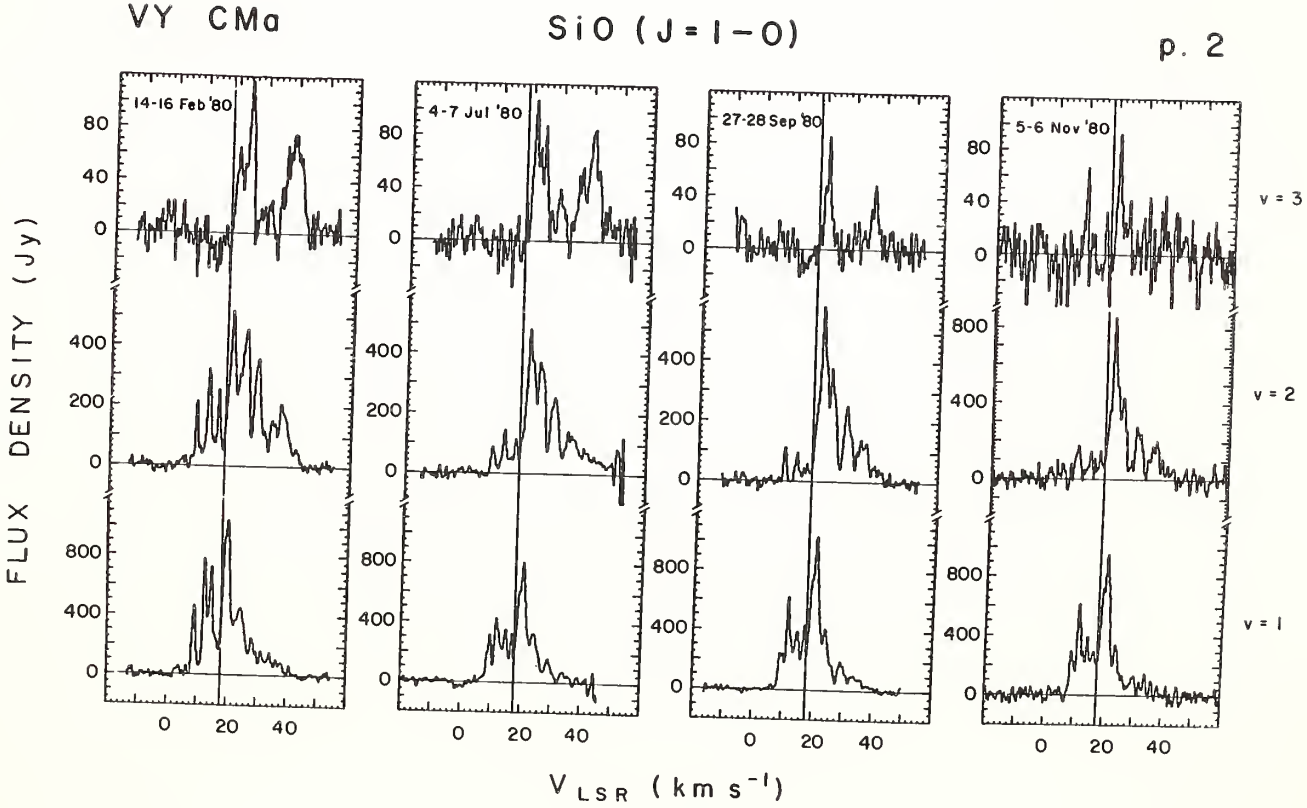
VY CMa
SiO (J = 1 − 0)
p. 2
14-16 Feb '80
4-7 Jul '80
27-28 Sep '80
5-6 Nov '80
v = 3
v = 2
v = 1
FLUX DENSITY (Jy)
V LSR (km s⁻¹)

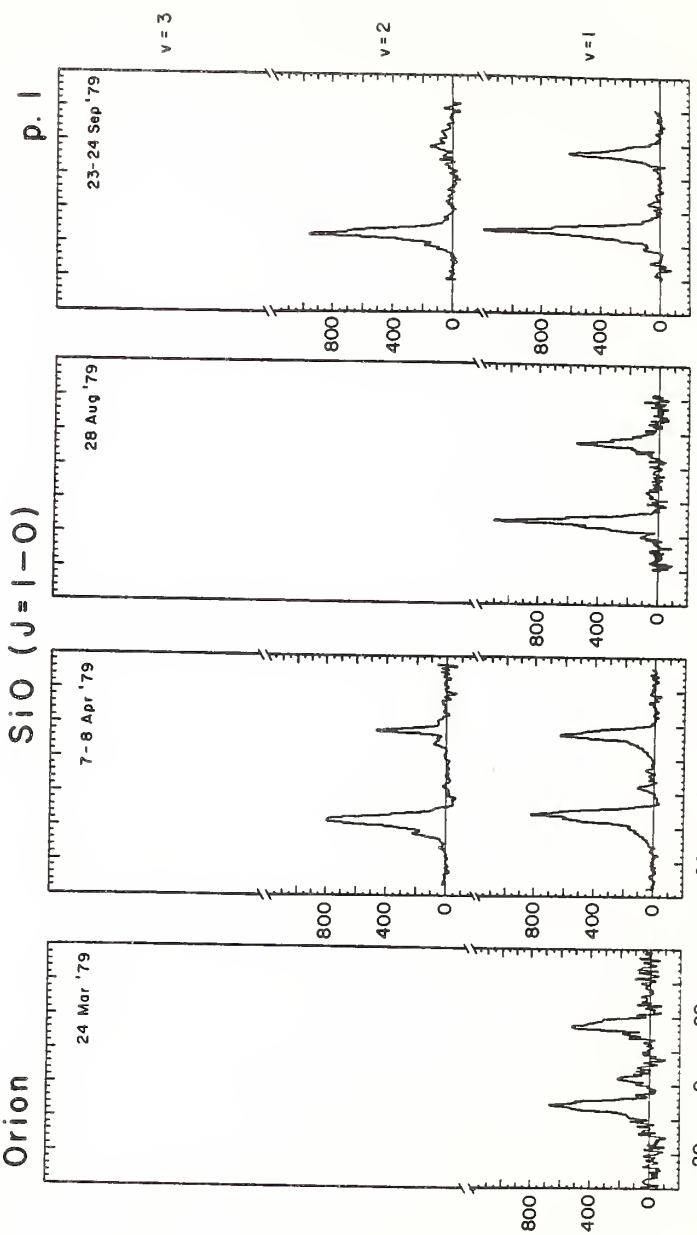
Orion
SiO (J=1-0)
p. 1
24 Mar '79
7-8 Apr '79
28 Aug '79
23-24 Sep '79
v=3
v=2
v=1
800
400
0
-20
0
20
FLUX DENSITY (Jy)
VLSR (km s-1)

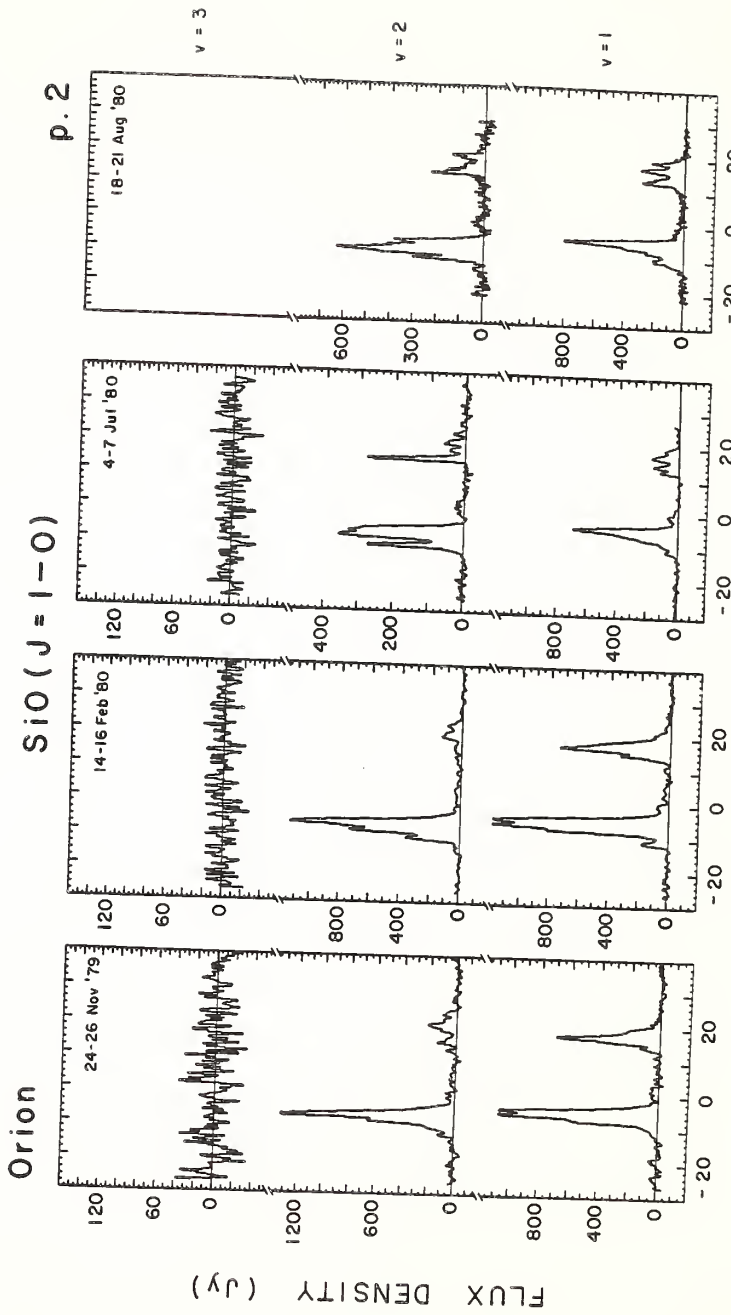
Orion
SiO (J = 1 − 0)
p. 2
24-26 Nov '79
14-16 Feb '80
4-7 Jul '80
18-21 Aug '80
v = 3
v = 2
v = 1
FLUX DENSITY (Jy)
V_{LSR} (km s^{-1})

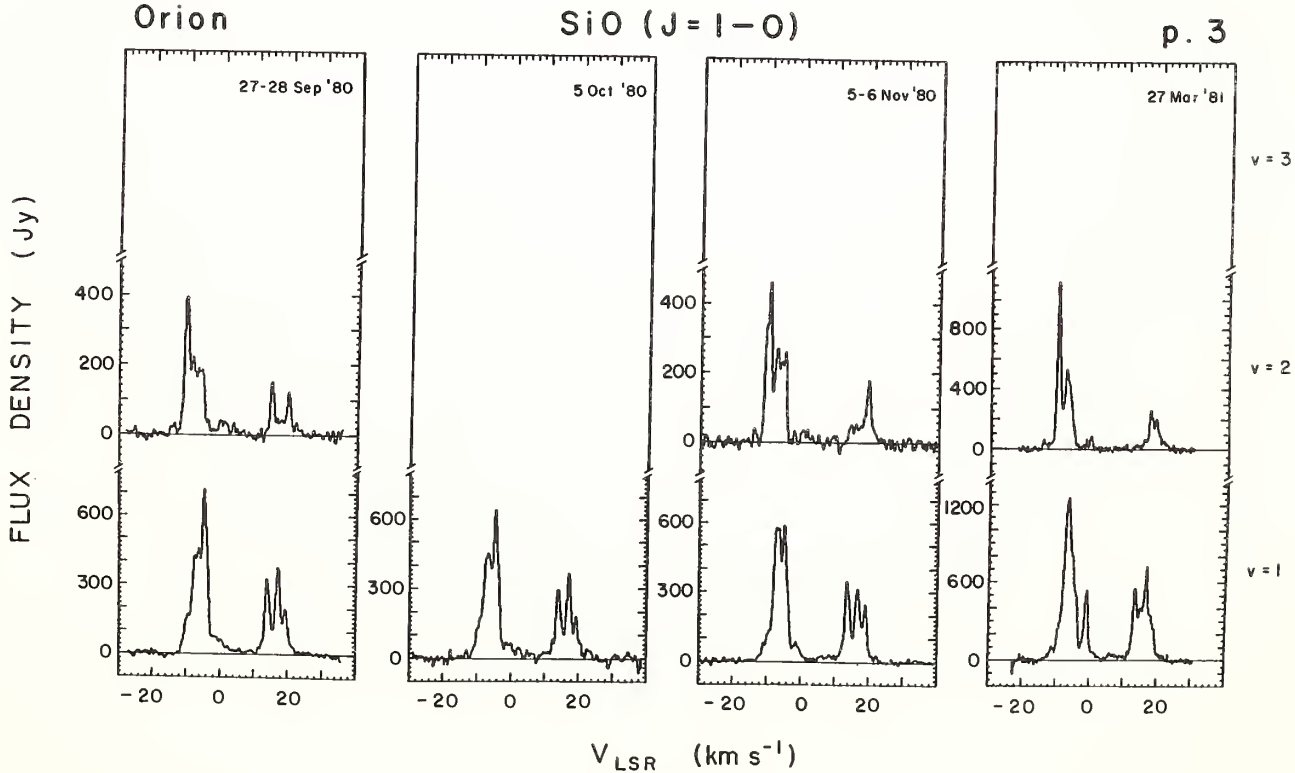
Orion
SiO (J = 1 − 0)
p. 3
27-28 Sep '80
5 Oct '80
5-6 Nov '80
27 Mar '81
v = 3
v = 2
v = 1
FLUX DENSITY (Jy)
400
200
0
600
300
0
800
400
0
1200
600
0
-20
0
20
V_{LSR} (km s^{-1})

Figure 6(a-m). SiO monitoring data for thirteen sources in the J=2-1 (v = 1) transition. Sources are arranged in order of increasing period, followed by the non-periodic sources VY CMa and Orion. The date of observation and the corresponding optical phase (ϕ) are shown. The vertical line marks the stellar velocity. All spectra were obtained with the FCRAO 14 m telescope.

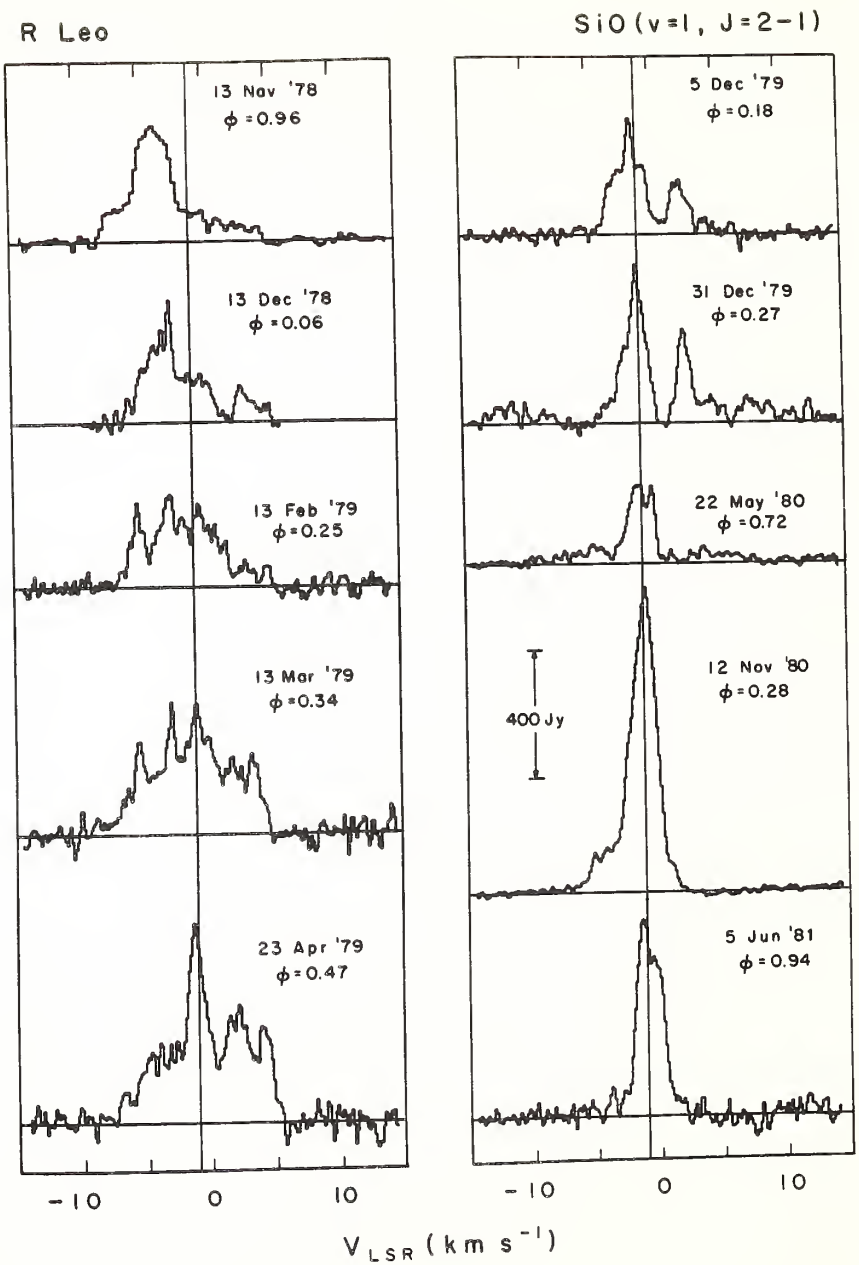
R Leo
SiO (v=1, J=2-1)
13 Nov '78
φ=0.96
13 Dec '78
φ=0.06
13 Feb '79
φ=0.25
13 Mar '79
φ=0.34
23 Apr '79
φ=0.47
5 Dec '79
φ=0.18
31 Dec '79
φ=0.27
22 May '80
φ=0.72
12 Nov '80
φ=0.28
5 Jun '81
φ=0.94
400 Jy
-10
0
10
-10
0
10
V LSR (km s-1)

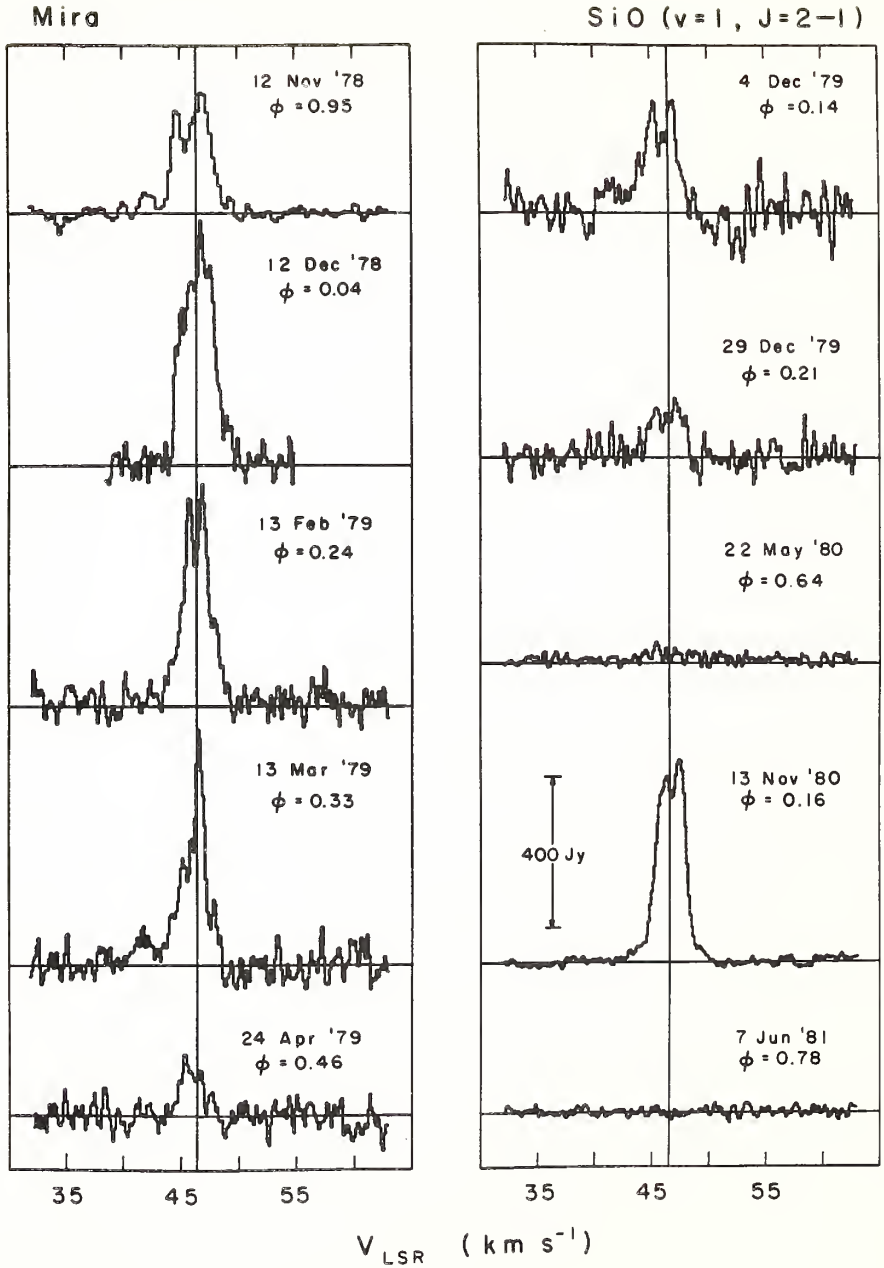
Mira
SiO (v=1, J=2−1)
12 Nov '78
ϕ =0.95
12 Dec '78
ϕ = 0.04
13 Feb '79
ϕ =0.24
13 Mar '79
ϕ = 0.33
24 Apr '79
ϕ = 0.46
4 Dec '79
ϕ =0.14
29 Dec '79
ϕ = 0.21
22 May '80
ϕ = 0.64
13 Nov '80
ϕ = 0.16
400 Jy
7 Jun '81
ϕ = 0.78
35
45
55
35
45
55
V LSR (km s⁻¹)

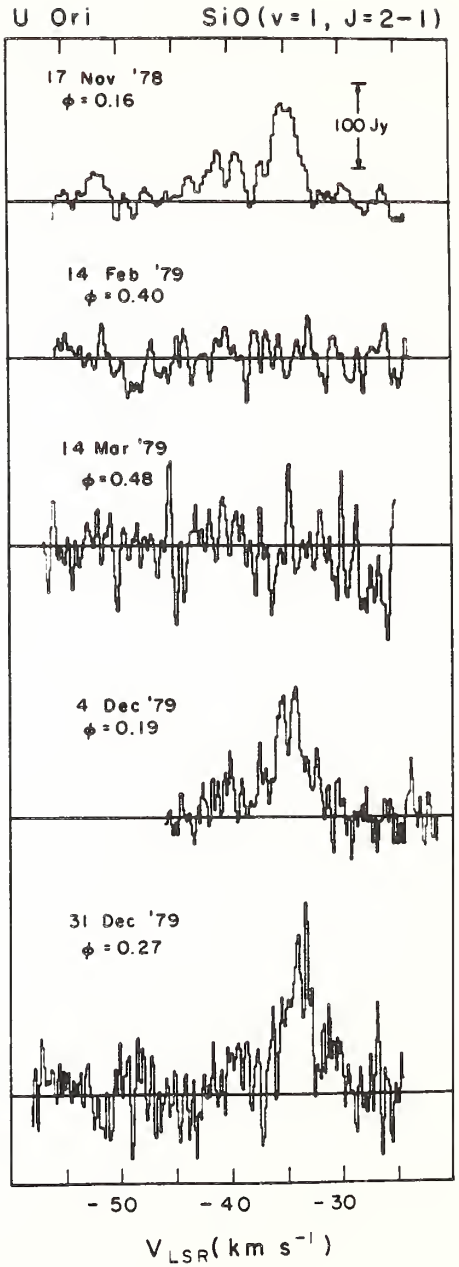
U Ori
SiO (v = 1, J = 2–1)
17 Nov '78
φ = 0.16
100 Jy
14 Feb '79
φ = 0.40
14 Mar '79
φ = 0.48
4 Dec '79
φ = 0.19
31 Dec '79
φ = 0.27
- 50
- 40
- 30
V LSR (km s⁻¹)

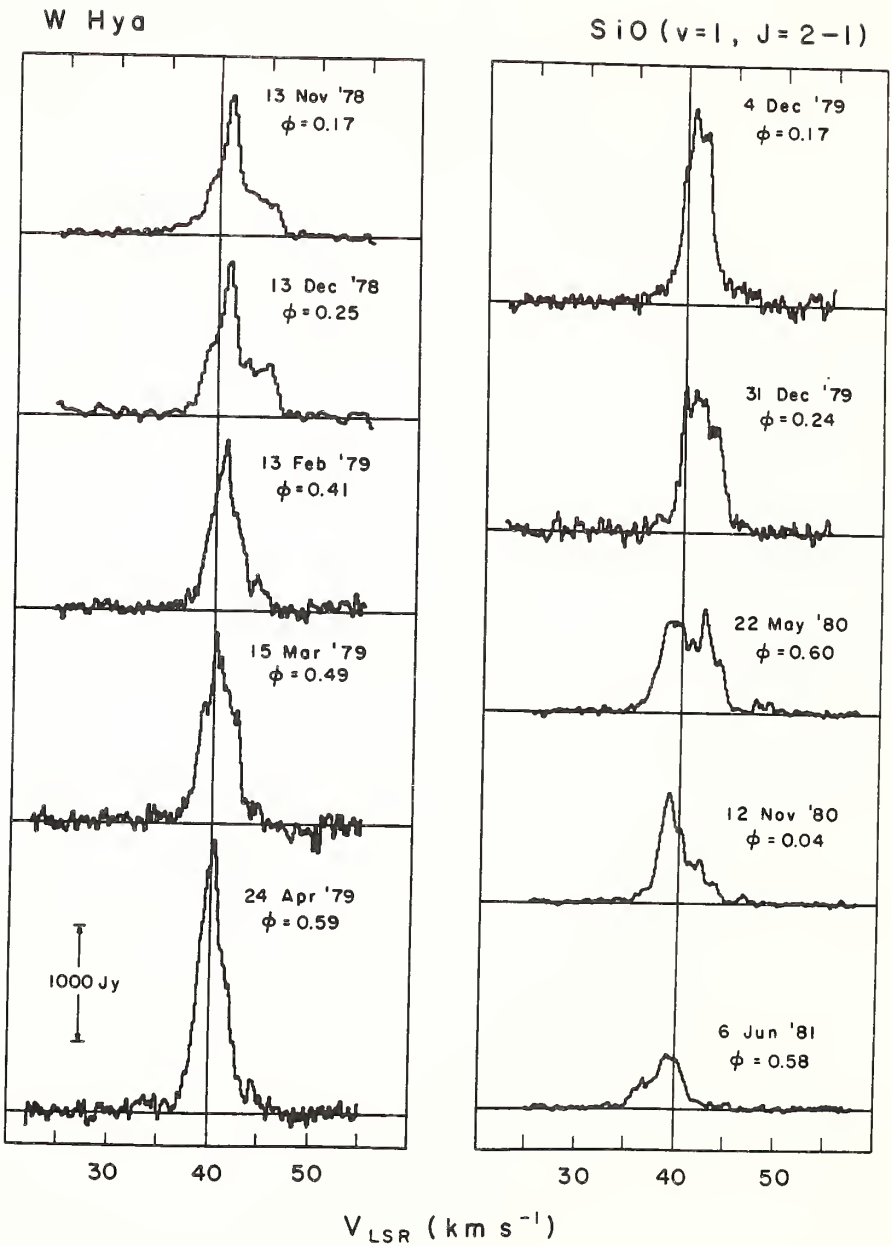
W Hya
SiO (v=1, J=2−1)
13 Nov '78
φ=0.17
13 Dec '78
φ=0.25
13 Feb '79
φ=0.41
15 Mar '79
φ=0.49
24 Apr '79
φ=0.59
1000 Jy
4 Dec '79
φ=0.17
31 Dec '79
φ=0.24
22 May '80
φ=0.60
12 Nov '80
φ=0.04
6 Jun '81
φ=0.58
30
40
50
30
40
50
V_LSR (km s^-1)

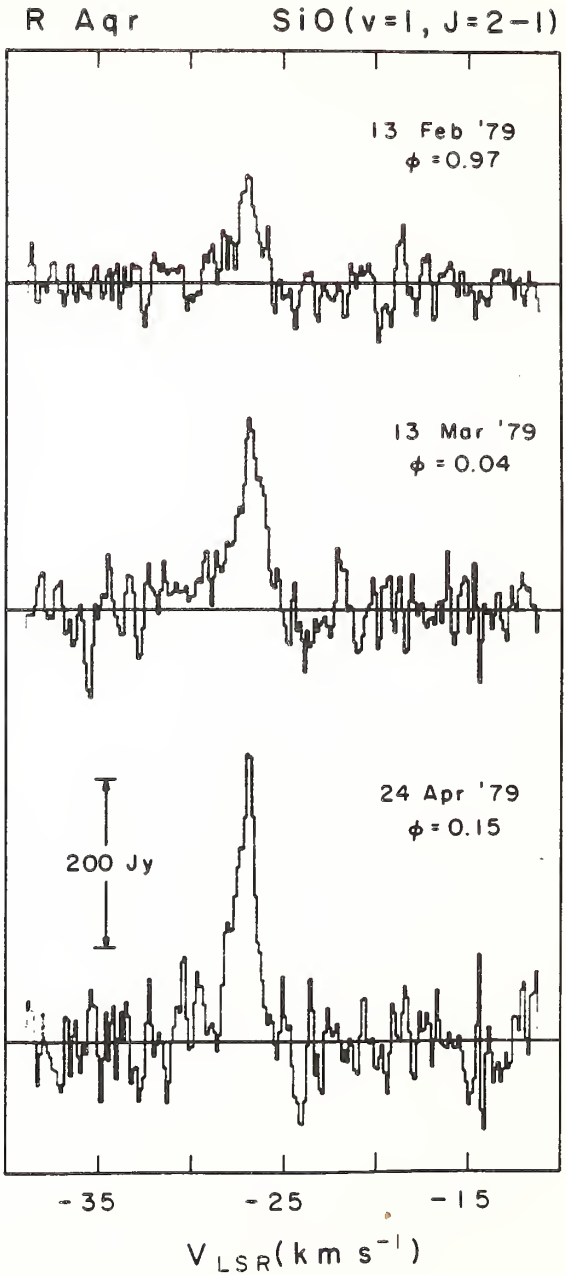
R Aqr
SiO (v=1, J=2−1)
13 Feb '79
φ = 0.97
13 Mar '79
φ = 0.04
24 Apr '79
φ = 0.15
200 Jy
-35
-25
-15
V LSR (km s⁻¹)

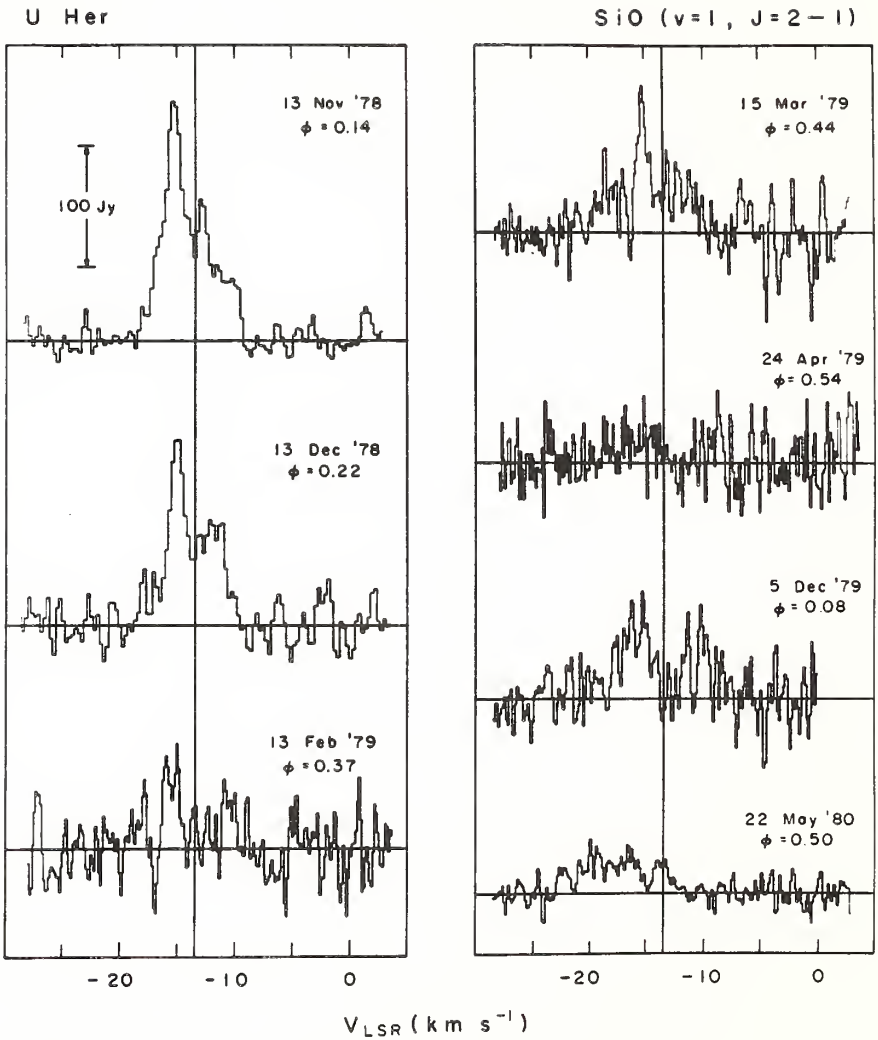
U Her
SiO (v=1, J=2−1)
13 Nov '78
φ = 0.14
100 Jy
13 Dec '78
φ = 0.22
13 Feb '79
φ = 0.37
15 Mar '79
φ = 0.44
24 Apr '79
φ = 0.54
5 Dec '79
φ = 0.08
22 May '80
φ = 0.50
-20
-10
0
V_LSR (km s^-1)

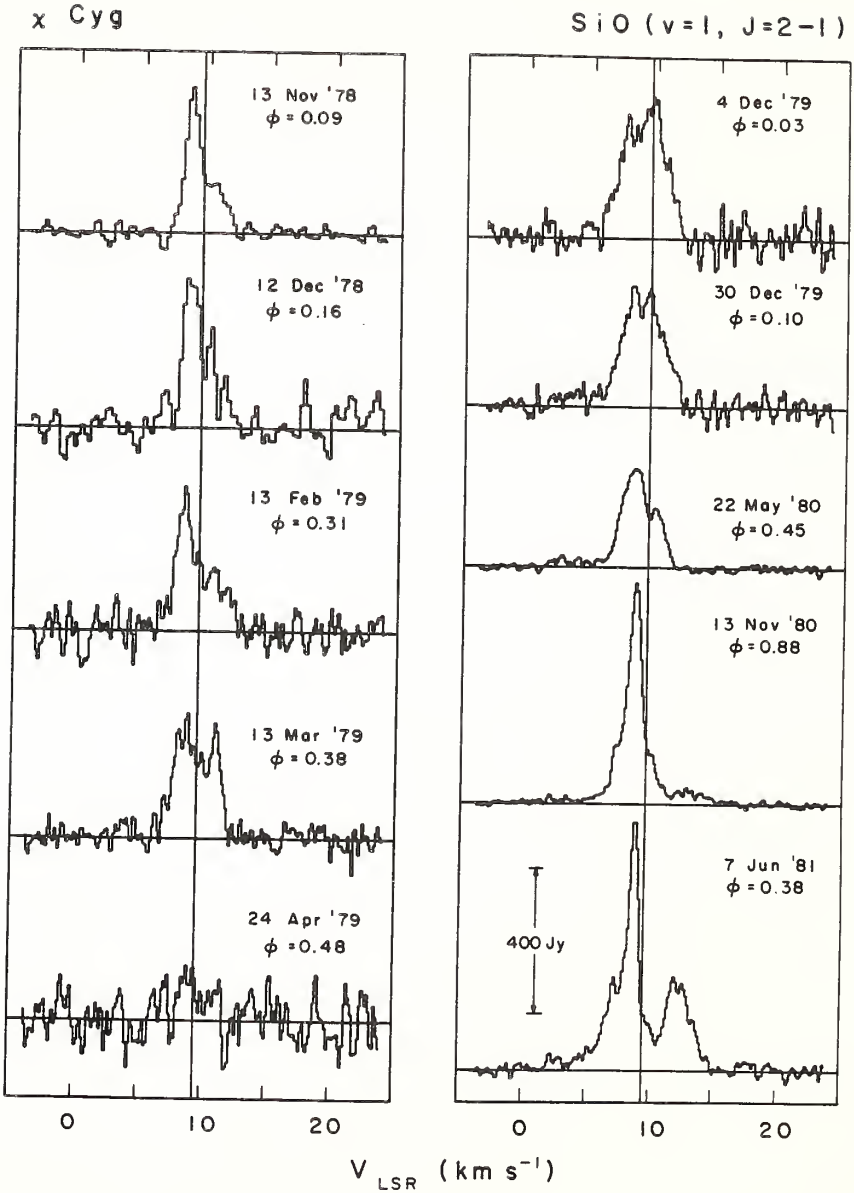
x Cyg
SiO (v=1, J=2−1)
13 Nov '78
ϕ = 0.09
12 Dec '78
ϕ = 0.16
13 Feb '79
ϕ = 0.31
13 Mar '79
ϕ = 0.38
24 Apr '79
ϕ = 0.48
4 Dec '79
ϕ = 0.03
30 Dec '79
ϕ = 0.10
22 May '80
ϕ = 0.45
13 Nov '80
ϕ = 0.88
7 Jun '81
ϕ = 0.38
400 Jy
0
10
20
0
10
20
V LSR (km s−1)

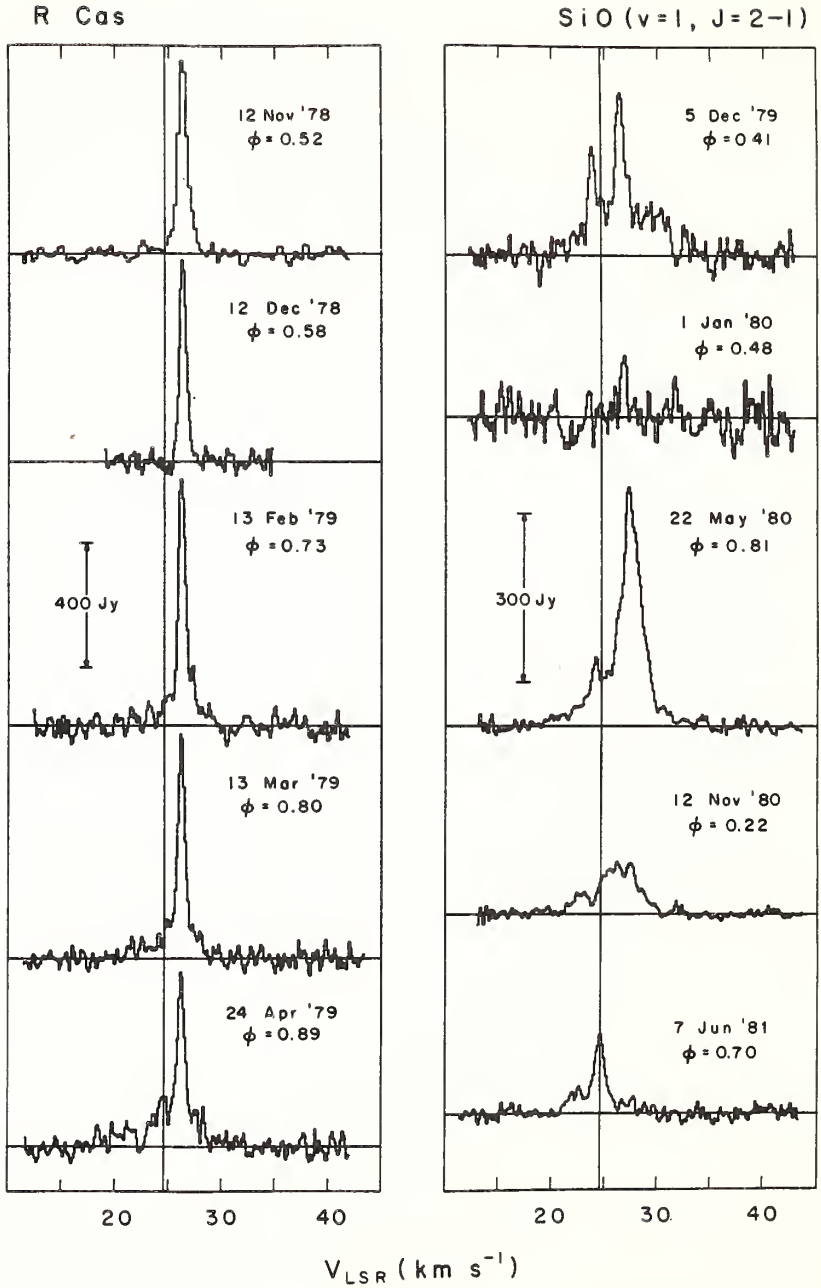
R Cas
SiO (v=1, J=2-1)
12 Nov '78
φ = 0.52
12 Dec '78
φ = 0.58
13 Feb '79
φ = 0.73
400 Jy
13 Mar '79
φ = 0.80
24 Apr '79
φ = 0.89
5 Dec '79
φ = 0.41
1 Jan '80
φ = 0.48
22 May '80
φ = 0.81
300 Jy
12 Nov '80
φ = 0.22
7 Jun '81
φ = 0.70
20
30
40
20
30
40
V_LSR (km s^-1)

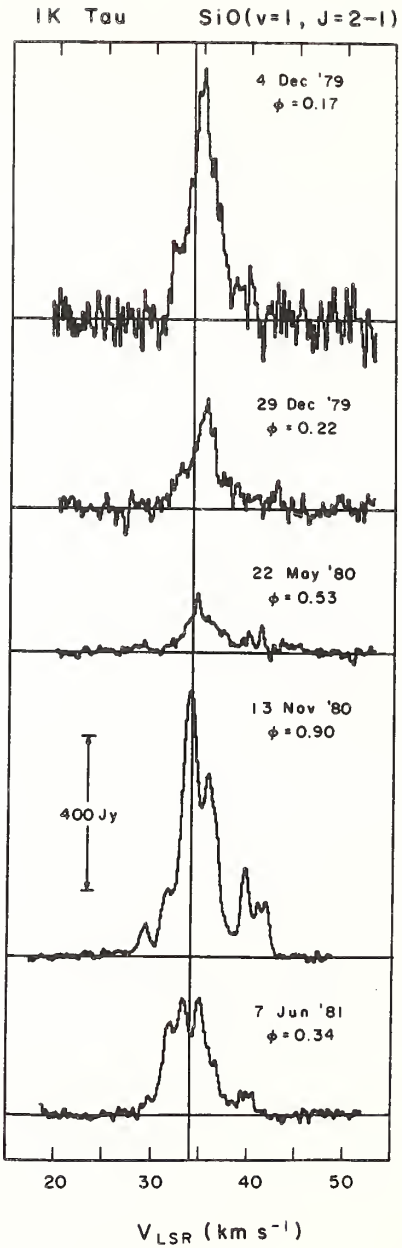
IK Tau
SiO(v=1, J=2-1)
4 Dec '79
φ = 0.17
29 Dec '79
φ = 0.22
22 May '80
φ = 0.53
13 Nov '80
φ = 0.90
400 Jy
7 Jun '81
φ = 0.34
20
30
40
50
V_LSR (km s^-1)

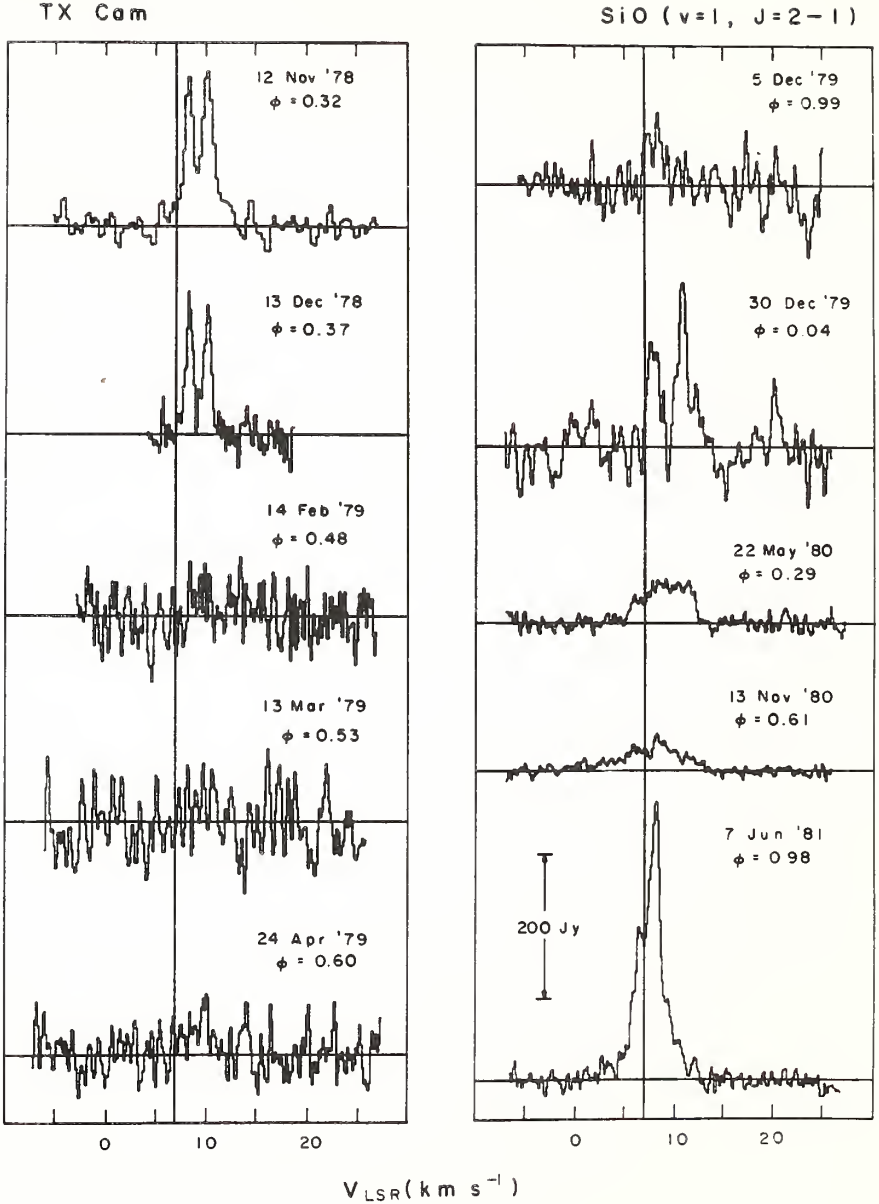
TX Cam
SiO (v=1, J=2−1)
12 Nov '78
φ = 0.32
13 Dec '78
φ = 0.37
14 Feb '79
φ = 0.48
13 Mar '79
φ = 0.53
24 Apr '79
φ = 0.60
5 Dec '79
φ = 0.99
30 Dec '79
φ = 0.04
22 May '80
φ = 0.29
13 Nov '80
φ = 0.61
7 Jun '81
φ = 0.98
200 Jy
0
10
20
0
10
20
V LSR (km s −1)

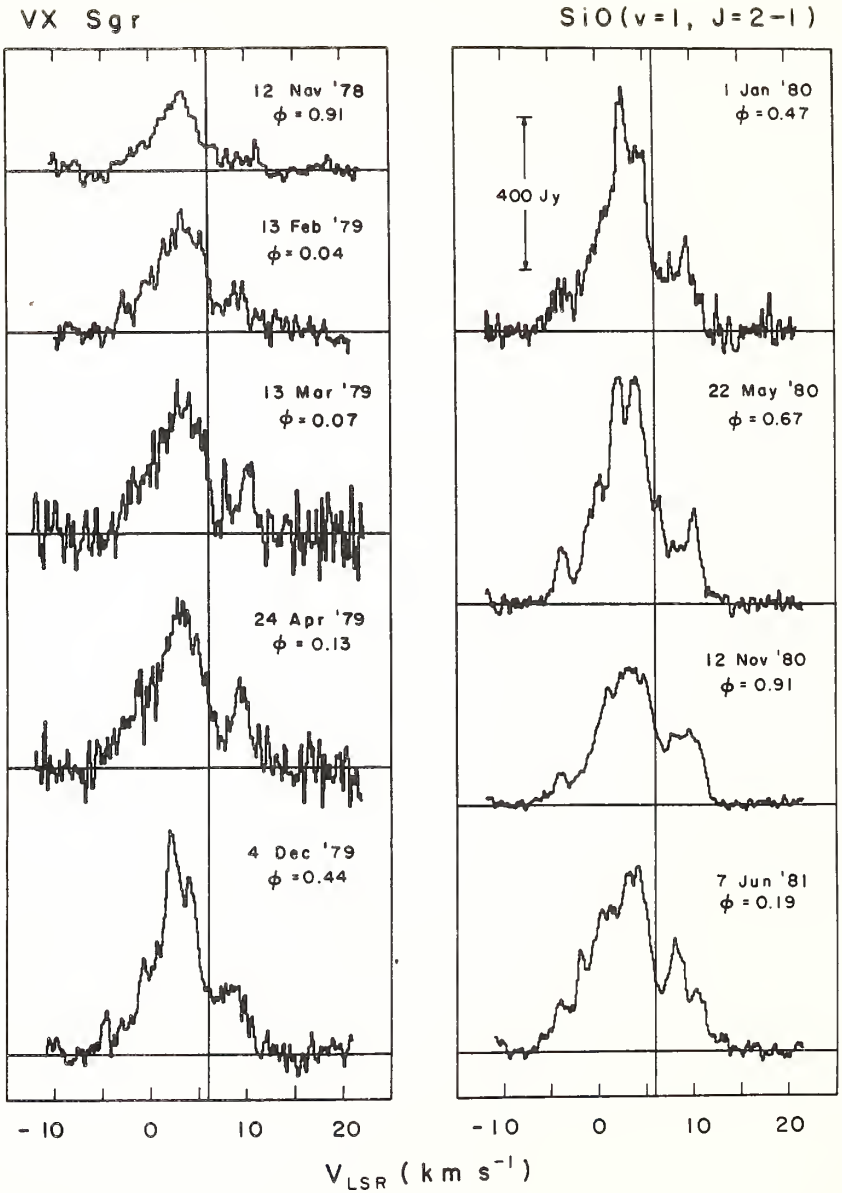
VX Sgr
SiO(v=1, J=2-1)
12 Nov '78
ϕ = 0.91
13 Feb '79
ϕ = 0.04
13 Mar '79
ϕ = 0.07
24 Apr '79
ϕ = 0.13
4 Dec '79
ϕ = 0.44
1 Jan '80
ϕ = 0.47
400 Jy
22 May '80
ϕ = 0.67
12 Nov '80
ϕ = 0.91
7 Jun '81
ϕ = 0.19
-10
0
10
20
-10
0
10
20
V_LSR (km s^-1)

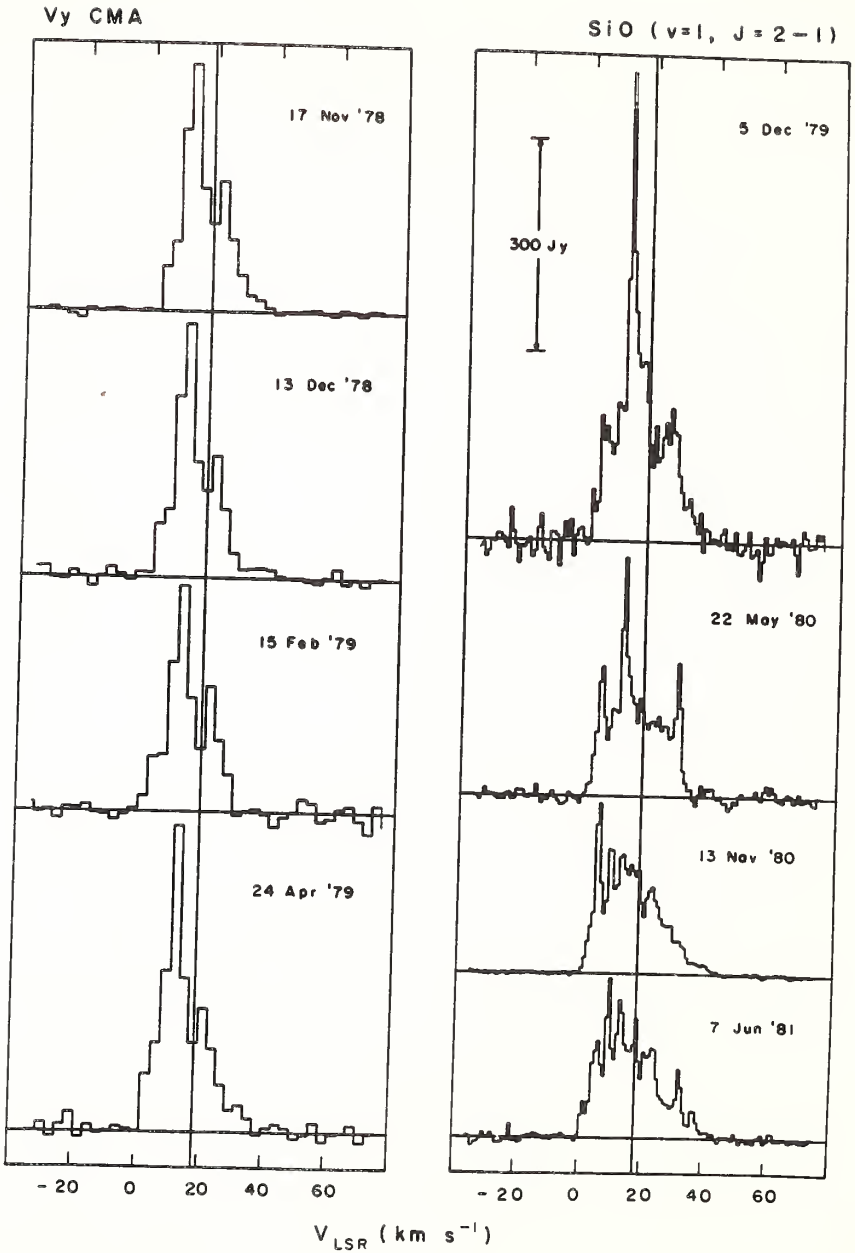
Vy CMA
SiO (v=1, J=2−1)
17 Nov '78
13 Dec '78
15 Feb '79
24 Apr '79
5 Dec '79
300 Jy
22 May '80
13 Nov '80
7 Jun '81
-20
0
20
40
60
V_LSR (km s^-1)

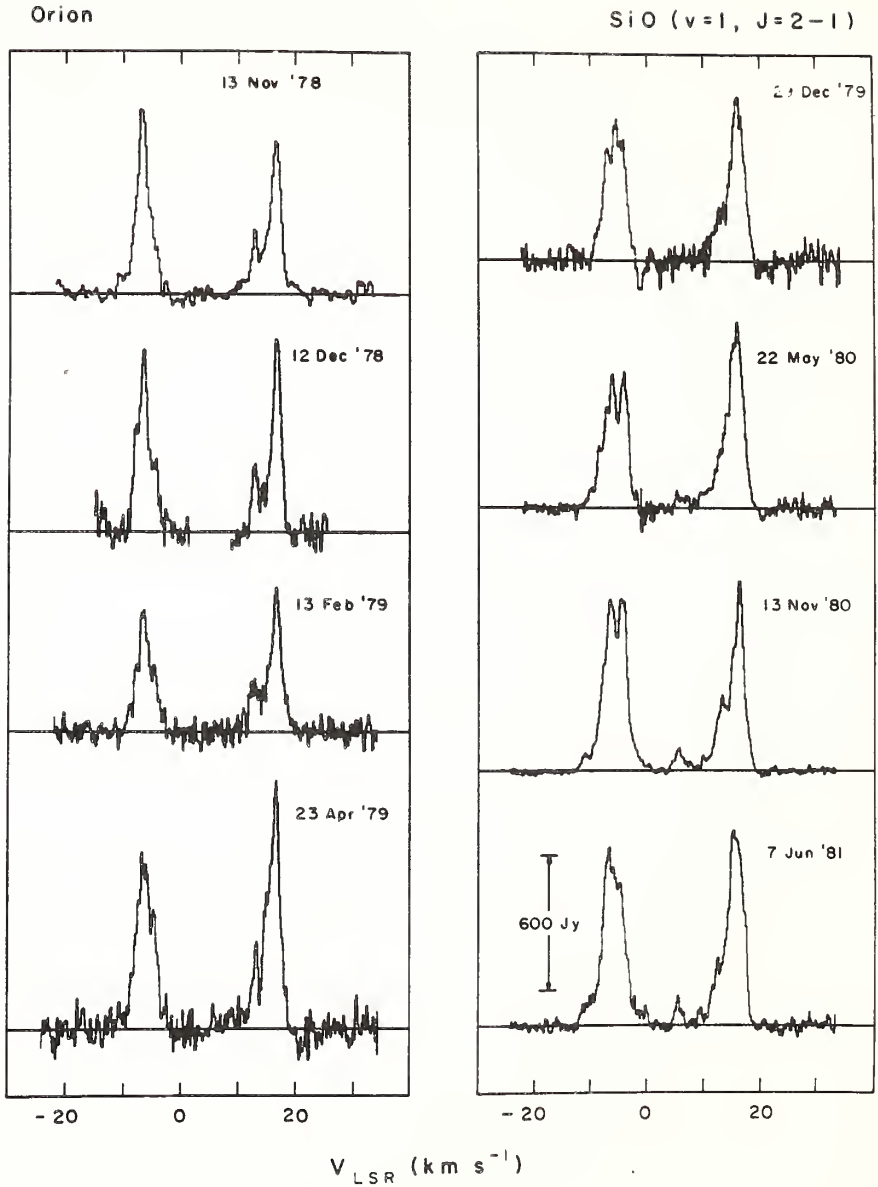
Orion
SiO (v=1, J=2−1)
13 Nov '78
12 Dec '78
13 Feb '79
23 Apr '79
21 Dec '79
22 May '80
13 Nov '80
7 Jun '81
600 Jy
- 20
0
20
- 20
0
20
V LSR (km s⁻¹)

from one spectrum to the next in order to facilitate analysis of velocity structure. For the 86 GHz spectra, because the range of variability is usually less than at 43 GHz, all spectra in a given panel are plotted with the same flux density scale. A vertical line marks the stellar velocity (cf. Table 1) for each source where a reasonably secure determination has been made. Since the values assumed for the stellar velocity have a significant bearing on the interpretation of the SiO emission, the measurement of these velocities and their accuracies are described in Chapter I, section 3.

General profile characteristics. From inspection of Figures 5 and 6, it is obvious that there is no "characteristic" SiO profile, as there is for the double peaked 1612 MHz OH maser in these and similar sources. The SiO maser profiles range from very simple to very complex. Three differentkinds of features (all of which may be present in the same spectrum) can be identified: strong, narrow spikes, typically 0.3 to 3.0 km s^{-1} in width; a broad ($\Delta v \geq 5$ km s^{-1}) blend of weak maser features, sometimes referred to as "pedestal" or "plateau" emission; and broad, low intensity "wings" (more commonly found in the supergiants than in the Mira variables) as illustrated in the high sensitivity filterbank spectrum of VY CMa in Figure 7. Examples of spectra dominated by individual spikes are VY CMa (e.g., Feb. 1980, v=2, J=1-0), R Cas (e.g., Nov. 1979, v=2, J=1-0), and IK Tau (e.g., Nov. 1980, v=2, J=1-0). Examples of spectra showing many blended features ("pedestal" emission) are W Hya (e.g., Jul. 1980, v=2, J=1-0) and R Leo (e.g., Mar. 1979, v=1, J=2-1).

Figure 7. SiO spectrum of VY CMa illustrating low intensity "wings". The data were obtained on Sept. 27, 1980, with the 256 x 250 kHz filterbank. The transition shown is the v=1, J=1-0 line.

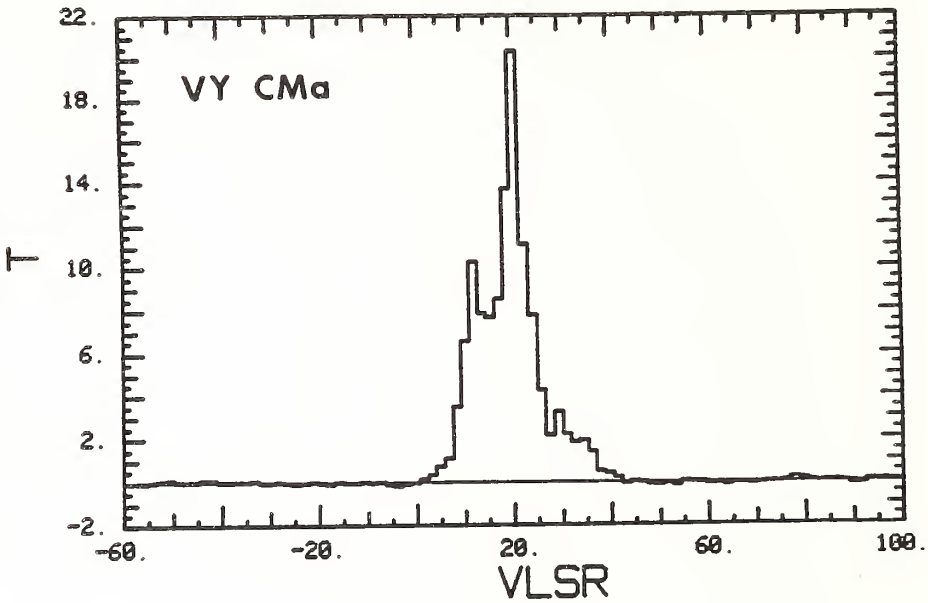
VY CMa
22.
18.
14.
10.
6.
2.
-2.
T
-60.
-20.
20.
60.
100.
VLSR

Just as there is no characteristic profile shape for SiO masers as a class, in general, individual sources usually do not maintain any characteristic appearance for periods longer than a few months. A source which shows simple structure, such as a single, narrow spike, at one epoch (e.g., Mira, Sept. 1979, v=1, J=1-0) may show complex structure at another epoch (cf. same source, Oct. 1980). A conspicuous exception is the Orion maser, which, although quite variable, always exhibits two major groups of components separated by 24 to 30 km s^{-1}. VY CMa and IK Tau always have many spikes and complex structure.

What velocities are present ? It has previously been noticed that, in contrast to the stellar OH masers, SiO maser emission occurs at velocities close to the stellar velocity, suggesting either that the masers lie near the stellar surface (e.g., inside the region where matter is accelerated to its terminal velocity) or that amplification occurs preferentially in a tangential direction (perpendicular to the velocity vector of large-scale mass outflow). The extensive body of data reported here has, however, uncovered a remarkable asymmetry in the velocity structure of the SiO maser emission. Contrary to what might be expected from an expanding shell located sufficiently close to the star for occultation of redshifted (backside) emission, the SiO maser profiles are systematically skewed to the red. This phenomenon is illustrated in Figure 8 (a-d) and the data are presented quantitatively in Table 5. For each source and each SiO transition, the maximum and minimum velocities (V_{max}, V_{min}) at which there was detectable emission were

Figure 8(a-d). Velocity extent of SiO emission relative to V_*. The solid bars show the average velocity extent of emission in the following transitions: a) v=1, J=1-0, b) v=2, J=1-0, c) v=3, J=1-0, d) v=1, J=2-1. The short vertical lines mark the most extreme velocities (relative to V_*) at which SiO emission was observed during the 2-1/2 year observing period. The number of spectra averaged for each source is shown in parentheses. Note that the emission is skewed to redshifted velocities for the v=1, J=1-0 and v=2, J=1-0 lines.

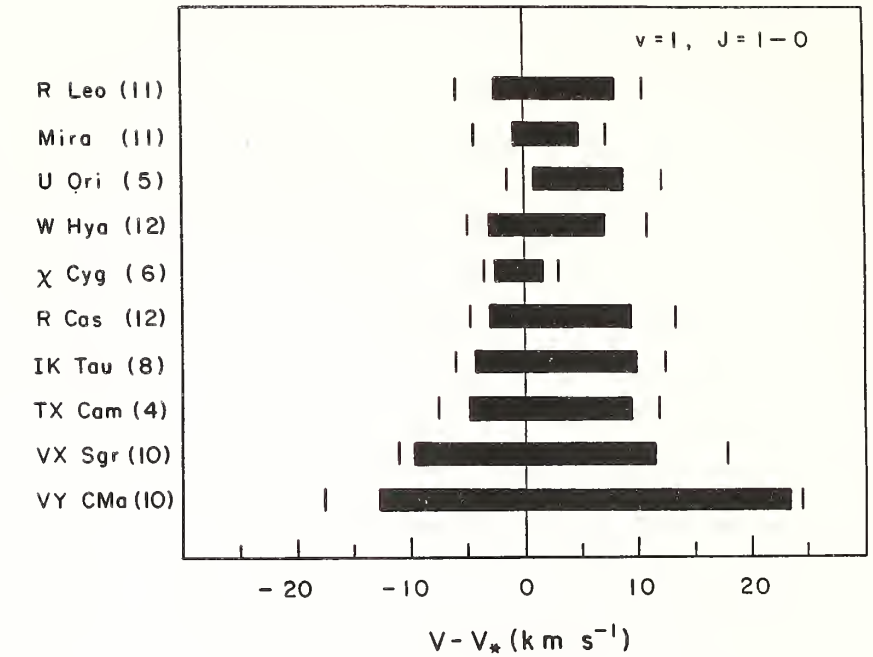
v = 1, J = 1 – 0
R Leo (11)
Mira (11)
U Ori (5)
W Hya (12)
χ Cyg (6)
R Cas (12)
IK Tau (8)
TX Cam (4)
VX Sgr (10)
VY CMa (10)
– 20
– 10
0
10
20
V – V* (km s⁻¹)

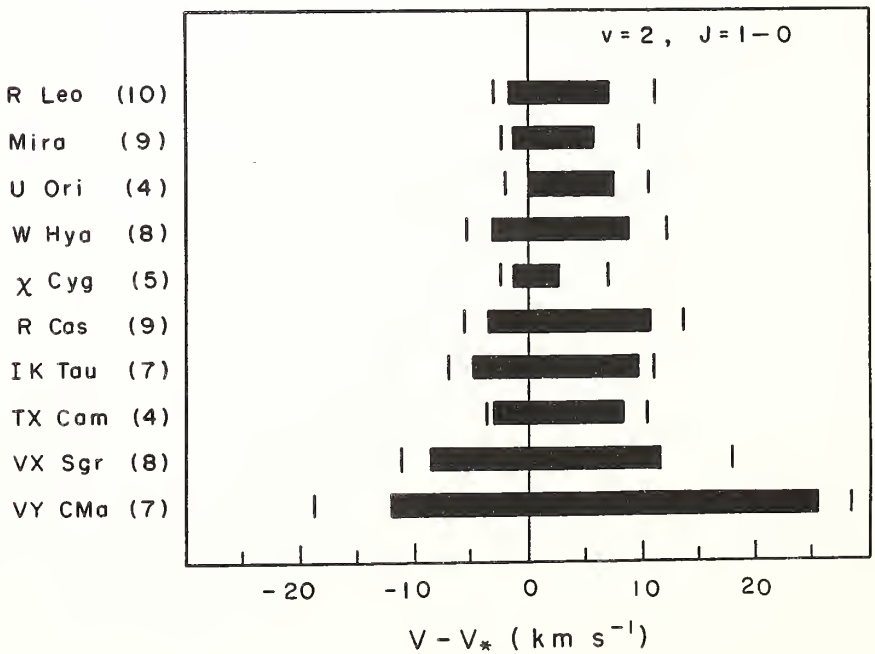
v = 2, J = 1 – 0
R Leo (10)
Mira (9)
U Ori (4)
W Hya (8)
χ Cyg (5)
R Cas (9)
IK Tau (7)
TX Cam (4)
VX Sgr (8)
VY CMa (7)
– 20
– 10
0
10
20
V – V* (km s⁻¹)

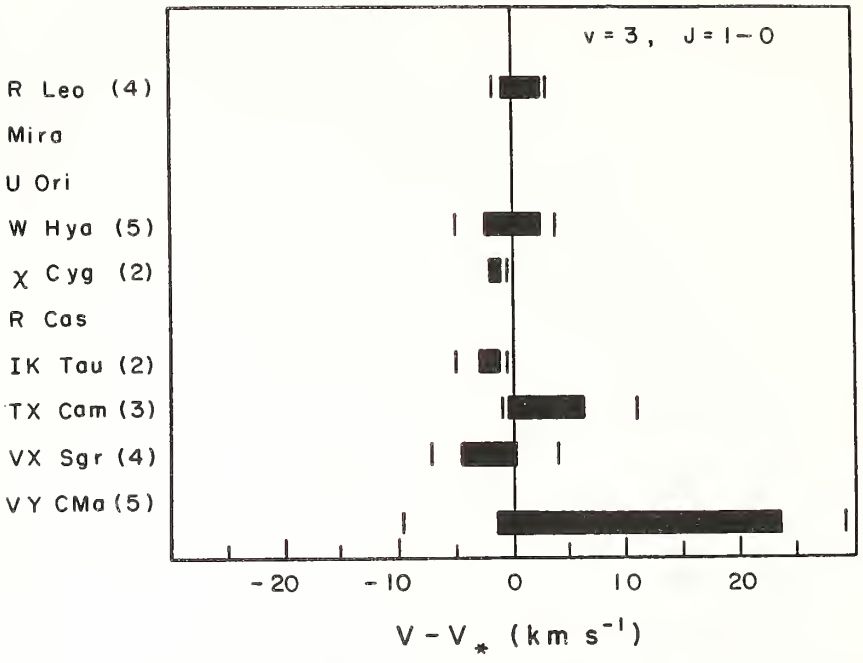
v = 3, J = 1 – 0
R Leo (4)
Mira
U Ori
W Hya (5)
χ Cyg (2)
R Cas
IK Tau (2)
TX Cam (3)
VX Sgr (4)
VY CMa (5)
-20
-10
0
10
20
V - V* (km s-1)

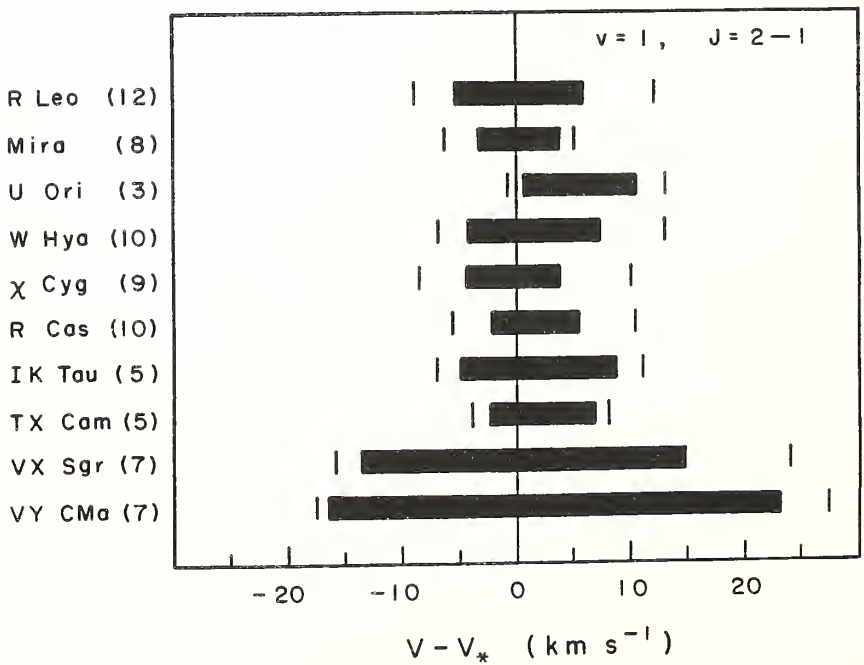
v = 1, J = 2 – 1
R Leo (12)
Mira (8)
U Ori (3)
W Hya (10)
χ Cyg (9)
R Cas (10)
IK Tau (5)
TX Cam (5)
VX Sgr (7)
VY CMa (7)
-20
-10
0
10
20
V - V* (km s-1)

TABLE 5

AVERAGE VELOCITY EXTENT OF SiO EMISSION

		v=1, J=1-0	v=2, J=1-0	v=3, J=1-0	v=1, J=2-1
R LEO	Blue[a]	2.7 ± 1.9[e]	1.9 ± 0.7	1.0 ± 0.4	5.6 ± 2.1
	Red[b]	8.1 ± 2.1	6.7 ± 2.9	2.3 ± 0.5	5.9 ± 2.6
	Total[c]	10.8 ± 2.8	8.6 ± 3.3	3.3 ± 0.7	11.5 ± 3.5
	N[d]	11	10	4	12
MIRA	Blue	1.2 ± 1.5	1.5 ± 0.7		3.7 ± 2.8
	Red	4.8 ± 1.3	5.5 ± 1.8		3.5 ± 1.1
	Total	6.0 ± 2.1	7.0 ± 1.9		7.1 ± 3.5
	N	11	9		8
U ORI	Blue	-0.9 ± 2.5	0.0 ± 2.7		-0.3 ± 2.3
	Red	8.8 ± 2.1	7.3 ± 3.1		10.3 ± 2.3
	Total	7.9 ± 4.0	7.3 ± 2.8		10.0 ± 4.0
	N	5	4		3
W HYA	Blue	3.0 ± 1.3	3.2 ± 1.5	2.4 ± 1.8	4.4 ± 1.3
	Red	7.0 ± 2.5	8.5 ± 2.6	2.4 ± 1.1	7.2 ± 2.4
	Total	10.0 ± 3.0	11.6 ± 3.4	4.8 ± 2.2	11.6 ± 3.4
	N	12	8	5	10
χ CYG	Blue	2.6 ± 0.7	1.5 ± 0.7	2.0 ± 0.0	4.4 ± 2.2
	Red	1.8 ± 0.9	2.5 ± 2.6	-1.3 ± 0.4	3.7 ± 2.6
	Total	4.4 ± 0.9	4.0 ± 2.0	0.8 ± 0.4	8.1 ± 4.0
	N	6	5	2	9
R CAS	Blue	3.1 ± 1.6	3.8 ± 1.7		2.3 ± 2.3
	Red	9.6 ± 2.4	10.6 ± 2.4		5.3 ± 2.7
	Total	12.6 ± 3.0	14.3 ± 3.9		7.5 ± 4.7
	N	12	9		10
IK TAU	Blue	4.2 ± 0.9	4.9 ± 1.2	3.0 ± 2.8	5.1 ± 1.7
	Red	10.0 ± 1.4	9.8 ± 0.9	-1.3 ± 1.1	8.6 ± 1.6
	Total	14.2 ± 1.2	14.7 ± 1.3	1.8 ± 1.8	13.7 ± 3.1
	N	8	7	2	5

TABLE 5 continued

		v=1, J=1-0	v=2, J=1-0	v=3, J=1-0	v=1, J=2-1
TX CAM	Blue	4.9 ± 1.9	3.0 ± 0.4	0.5 ± 0.5	2.5 ± 1.3
	Red	9.8 ± 2.2	8.1 ± 2.8	6.2 ± 4.4	6.7 ± 0.8
	Total	14.6 ± 3.5	11.1 ± 3.0	6.7 ± 4.5	9.3 ± 1.1
	N	4	4	3	5
VX SGR	Blue	9.4 ± 0.7	8.7 ± 1.3	4.5 ± 1.7	13.9 ± 1.6
	Red	11.6 ± 1.6	11.7 ± 1.4	0.1 ± 2.7	14.6 ± 5.9
	Total	21.0 ± 2.2	20.3 ± 2.2	4.6 ± 4.3	28.5 ± 7.3
	N	10	8	4	7
VY CMA	Blue	12.6 ± 3.4	12.0 ± 3.6	1.5 ± 4.7	16.5 ± 1.6
	Red	23.7 ± 0.9	25.5 ± 1.9	23.6 ± 9.0	23.1 ± 3.8
	Total	36.3 ± 3.7	37.5 ± 4.3	25.1 ± 4.8	39.6 ± 4.0
	N	10	7	5	7

Notes to Table 5:

(a) Average velocity extent (in km s^{-1}) of blueshifted emission: $\langle V_* - V_{min} \rangle$.
(b) Average velocity extent (in km s^{-1}) of redshifted emission: $\langle V_{max} - V_* \rangle$.
(c) Average total velocity width (in km s^{-1}) of emission: $\langle V_{max} - V_{min} \rangle$.
(d) Number of spectra averaged.
(e) One standard deviation (a measure of source variability, not of error).

measured at each epoch. For this analysis, information from the autocorrelator spectra shown in Figs. 5 and 6 was combined with the higher sensitivity filterbank data to determine the broadest extent of low level emission. Using the values of stellar velocity (V_*) from Table 1, the average velocity extent of redshifted emission ($\langle V_{max} - V_* \rangle$) and the average velocity extent of blueshifted emission ($\langle V_* - V_{min} \rangle$) were computed. The resulting values, with the one standard deviation measure of the variability in the spectra, are listed in the first two rows of each source entry in Table 5. The average total velocity width of the emission ($\langle V_{max} - V_{min} \rangle$) and the number of spectra contributing to each average (N) are also listed.

The four plots of Figure 8 illustrate the SiO maser velocity extent and the predominance of redshifted or blueshifted velocities for each transition. The solid bars represent the average velocity extent of the emission relative to V_*, while the short vertical lines indicate the extreme velocities at which emission was observed during the $2\frac{1}{2}$ year period of the observations. The number of spectra examined for each source is given in parentheses following the source name. It is clear from the plots that both the average and the extremes of the velocity extent are significantly skewed to the red for the v=1, J=1-0 and v=2, J=1-0 transitions. The only exception is χ Cyg in the v=1, J=1-0 line; here the emission covers the narrowest velocity range of any of the sources and is quite weak, perhaps masking the common effect. Except for the peculiar source VY CMa, the results in the v=3, J=1-0 transition

are ambiguous. Although two sources (TX Cam, R Leo), in addition to VY CMa, appear preferentially redshifted, three sources (χ Cyg, IK Tau, VX Sgr) are exclusively blueshifted and one (W Hya) is well-centered about the stellar velocity. Because the v=3 emission is so weak, these results are probably dominated by the appearance of single maser spikes, rather than by some more global property of the SiO line formation region.

The red-skewing of the SiO maser velocities is not as pronounced in the v=1, J=2-1 line (Fig. 8-d) as in the lower frequency lines. In fact, in this transition, the emission in most sources appears reasonably well-centered about the stellar velocity. (This centering suggests that the effect seen in the J=1-0 lines is probably not due to a systematic skewing to the blue of the stellar velocities used in the analysis, at least for most sources). Two of the sources which do show a pronounced redshift in the v=1, J=2-1 line (U Ori, TX Cam) are sources whose stellar velocity is somewhat less well-determined than the others.

On the average, the centroid of the emission in the v=1, J=1-0 and v=2, J=1-0 lines for the ten sources in Table 5 is skewed to the red by 2.7 km s^{-1}, with a dispersion about the mean of 1.6 km s^{-1}. (If χ Cyg, a source which is anomalous in various ways, is omitted from the average, the mean redshift becomes 3.0 ± 1.4 km s^{-1}). For the v=1, J=2-1 line, the mean velocity is shifted to the red by 1.5 ± 1.7 km s^{-1}.

The predominance of redshifted SiO maser emission is even more strikingly demonstrated by computing the fraction of the total flux

which is emitted at velocities redshifted from V*. As one might expect from the asymmetry in the velocity extent of emission, significantly more flux is received from redshifted gas than from blueshifted gas in the J=1-0, v=1 and v=2 transitions. The total integrated fluxes (in units of 10^{-20} W m^{-2}) are listed in Table 6 for the J=1-0 transitions and in Table 7 for the J=2-1 transitions. The integrated fluxes on the redshifted and blueshifted sides of V* were computed and the fraction of the total flux which is redshifted is given in parentheses following each value for the total flux in Tables 6 and 7.

For all of the M-spectral-type Mira variables except U Her (i.e., seven sources), 65-100% of the total flux is redshifted from V* in almost every instance in the J=1-0 lines. In general, the v=1, J=2-1 transition does <u>not</u> show this clearcut predominance of redshifted emission. Among the seven sources which have high percentages of redshifted flux at 43 GHz, only R Cas, U Ori, and TX Cam have predominantly redshifted emission at 86 GHz. The v=1, J=2-1 flux for U Her, χ Cyg, VX Sgr, and VY CMa is predominantly blueshifted, while R Leo, Mira, IK Tau, and Orion have more or less equivalent amounts of redshifted and blueshifted flux.

Neither the velocity extent nor the percentage of flux which is redshifted were found to have <u>any</u> systematic dependence on stellar phase in any transition for any source. Such a dependence might be expected if the SiO line formation region is mechanically coupled to the pulsating stellar photosphere.

TABLE 6

SiO (J = 1-0) TOTAL INTEGRATED FLUXES (x 10^{-20} W m^{-2})
AND FRACTION OF TOTAL FLUX WHICH IS REDSHIFTED

SOURCE	DATE	v = 1	v = 2	v = 3	OPT.‡ PHASE
R LEO	3/24-25/79	305 (.94)			.38
	4/7-9/79	242 (.90)	403 (.95)		.42
	8/27-28/79	46 (.96)			.87
	9/24/79	84 (.86)			.95
	11/24/79	48 (.69)	14 (.93)		.15
	2/12-16/80	29 (.68)	67 (.65)	[n.d.]*	.41
	7/4-7/80	219 (.79)	294 (.77)	26 (1.0)	.87
	8/18-21/80	482 (.75)	247 (.65)	46 (.74)	.01
	9/27-29/80	556 (.79)	433 (.83)	27 (.95)	.13
	10/4-12/80	485 (.80)	406 (.82)		.17
	11/4-6/80	376 (.70)	396 (.72)	16 (.78)	.26
	3/26-27/81	66 (.81)	35 (.90)		.71
MIRA	3/24/79	51 (.58)			.36
	4/7-8/79	33 (.81)	66 (.92)	[n.d.]	.41
	8/27/79	59 (1.0)			.85
	9/24/79	123 (.96)			.93
	11/23-26/79	173 (.89)	115 (.89)	[n.d.]	.11
	2/14-16/80	129 (.68)	105 (.77)	[n.d.]	.35
	7/4-7/80	20 (.84)	34 (.92)	[n.d.]	.77
	8/18-21/80	132 (.83)	41 (.84)		.90
	10/5-12/80	219 (.82)	122 (.73)	[n.d.]	.05
	11/5-6/80	216 (.72)	188 (.64)	[n.d.]	.14
	3/26-27/81	6 (.94)			.56
U ORI	4/8-9/79	[n.d.]	32 (1.0)		.55
	8/28/79	62 (.84)			.93
	11/24-25/79	152 (.88)	118 (.95)	[n.d.]	.17
	2/14-15/80	52 (.99)	36 (.72)		.39
	7/4-5/80	25 (1.0)	20 (.70)		.76
W HYA	3/24/79	378 (.79)			.51
	4/7-9/79	495 (.88)	277 (.82)	[n.d.]	.55
	8/28/79	758 (.81)			.92
	9/23/79	693 (.92)			.99
	11/23-25/79	863 (.79)	1022 (.62)	87 (.51)	.15
	2/12-17/80	443 (.82)	646 (.91)	[n.d.]	.36
	7/5-7/80	419 (.89)	339 (.76)	[n.d.]	.72
	8/18-20/80	321 (.75)	381 (.64)	[n.d.]	.83
	9/27-28/80	364 (.69)	398 (.56)	16 (.50)	.93
	10/4-13/80	375 (.65)	646 (.58)	19 (.60)	.95
	11/5-6/80	618 (.56)		33 (1.0)	.03
	3/27/81	173 (.64)	217 (.47)		.38

TABLE 6 continued

SOURCE	DATE	v = 1	v = 2	v = 3	OPT.‡ PHASE
R AQR	4/9/79	67			.11
	8/28/79	51			.47
	11/24-26/79	55	9	[n.d.]	.70
	2/12-15/80	49	22	[n.d.]	.91
	7/4-9/80	49	30	[n.d.]	.31
U HER	3/24/79	[n.d.]			.46
	4/7/79		[n.d.]		.50
	11/23-24/79	45 (.24)	21 (.09)		.05
	2/14-15/80	37 (.10)	40 (0.0)		.26
χ CYG	4/7/79		6 (1.0)		.44
	11/23-25/79	14 (.84)	35 (.48)	[n.d.]	.01
	2/12-15/80	16 (.42)	38 (.22)	[n.d.]	.21
	7/4-9/80	[n.d.]	[n.d.]	[n.d.]	.56
	8/18-21/80	[n.d.]	[n.d.]		.67
	9/27-28/80	13 (.39)	6 (0.0)		.77
	10/5-12/80	7 (.29)	7 (0.0)		.78
	11/5-6/80	8 (.13)	7 (.24)	[n.d.]	.86
	3/27/81	66 (.09)	[n.d.]		.21
R CAS	3/24/79	200 (.96)			.82
	4/4-8/79	198 (.94)	145 (.88)	[n.d.]	.85
	8/27/79	341 (.87)			.19
	9/23/79	275 (.88)			.25
	11/24-25/79	198 (.88)	91 (.71)	[n.d.]	.39
	2/12-17/80	105 (.89)	77 (.62)	[n.d.]	.58
	7/5-9/80	162 (.82)	75 (.72)	[n.d.]	.92
	8/18-21/80	106 (.79)	42 (.73)	[n.d.]	.02
	9/28/80	117 (.75)	45 (.68)	[n.d.]	.11
	10/4-12/80	94 (.76)	60 (.80)		.14
	11/4-6/80	61 (.72)	13 (.88)		.20
	3/27/81	[n.d.]	[n.d.]		.53
IK TAU	9/23-24/79	617 (.82)	449 (.68)		.02
	11/23-26/79	492 (.74)	284 (.59)	4 (0.0)	.15
	2/13-15/80	189 (.66)	121 (.55)	[n.d.]	.32
	7/4-9/80	104 (.62)	67 (.71)	[n.d.]	.62
	8/21/80	119 (.57)			.72
	9/28-29/80	203 (.65)	92 (.68)		.80
	10/5-12/80	183 (.64)	88 (.68)	8 (0.0)	.83
	11/5-6/80	220 (.72)	120 (.61)	[n.d.]	.89

TABLE 6 continued

SOURCE	DATE	v = 1	v = 2	v = 3	OPT.‡ PHASE
TX CAM	4/7/79	[n.d.]	20 (.64)		.57
	11/25-26/79	198 (.85)	174 (.89)	14 (1.0)	.97
	2/14-16/80	455 (.89)	370 (.89)	41 (1.0)	.12
	7/4-9/80	167 (.84)	156 (.80)	[n.d.]	.37
	8/21/80	[n.d.]			.46
	9/27/80	65 (.81)			.52
VX SGR	3/25/79	627 (.35)			.09
	4/7-9/79	435 (.31)	897 (.38)	40 (.14)	.11
	8/28/79	1048 (.38)			.30
	11/23-25/79	1090 (.39)	563 (.42)	20 (0.0)	.42
	2/12-17/80	731 (.45)	473 (.45)	11 (0.0)	.54
	7/4-9/80	498 (.43)	304 (.47)	4 (0.0)	.73
	8/19-20/80	513 (.46)		[n.d.]	.79
	9/27-28/80	471 (.46)	212 (.49)	[n.d.]	.84
	10/4-12/80	470 (.44)	294 (.54)		.85
	11/4-5/80		172 (.54)	[n.d.]	.90
VY CMA	3/24/79	1264 (.50)			
	4/7-8/79	1002 (.43)	517 (.47)		
	9/24/79	1251 (.58)			
	11/24-26-79	1368 (.59)	631 (.73)	139 (1.0)	
	2/14-16/80	1424 (.65)	929 (.80)	115 (1.0)	
	7/4-7/80	970 (.64)	719 (.88)	139 (1.0)	
	9/27-28/80	1231 (.66)	638 (.92)	48 (1.0)	
	11/5-6/80	1069 (.62)	732 (.82)	52 (.95)	
ORION	3/24/79	669 (.43)			
	4/7-8/79	820 (.39)	619 (.23)		
	8/28/79	715 (.33)			
	9/23-24/79	827 (.32)	553 (.18)		
	11/24-26/79	963 (.34)	808 (.18)	[n.d.]	
	2/14-16/80	1200 (.34)	785 (.14)	[n.d.]	
	7/4-7/80	431 (.27)	319 (.23)	[n.d.]	
	8/18-21/80	662 (.34)	476 (.24)		
	9/27-28/80	719 (.35)	330 (.24)		
	10/5/80	677 (.36)			
	11/5-6/80	696 (.37)	367 (.21)		
	3/27/81	1285 (.36)	574 (.22)		

* Non-detections are indicated by "[n.d.]".

‡ Phases are from optical light curves kindly provided by J. Mattei of the American Association of Variable Star Observers.

TABLE 7

SiO (J = 2-1) TOTAL INTEGRATED FLUXES (x 10^{-20} W m^{-2})
AND FRACTION OF TOTAL FLUX WHICH IS REDSHIFTED

SOURCE	DATE	v = 1	v = 2	OPT.‡ PHASE
R LEO	11/13/78	480 (.18)		.96
	12/13/78	339 (.26)		.06
	2/13/79	468 (.37)		.25
	3/13/79	759 (.44)		.34
	4/23/79	901 (.51)		.47
	12/5/79	356 (.47)		.18
	12/31/79	344 (.57)		.27
	5/22/80	230 (.44)	[n.d.]*	.72
	11/12/80	690 (.41)	[n.d.]	.28
	6/5/81	425 (.44)		.94
MIRA	11/12/78	322 (.51)		.95
	12/12/78	520 (.60)		.04
	2/13/79	421 (.48)		.24
	3/13/79	367 (.43)		.33
	4/24/79	88 (.28)		.46
	12/4/79	308 (.37)		.14
	12/29/79	107 (.40)		.21
	5/22/80	23 (.48)	[n.d.]	.64
	11/13/80	454 (.58)	[n.d.]	.16
	6/7/81	[n.d.]		.78
U ORI	11/17/78	153 (.68)		.16
	2/14/79	[n.d.]		.40
	3/14/79	[n.d.]		.48
	12/4/79	174 (.84)		.19
	12/31/79	183 (.94)		.27
	5/22/80	44 (.69)		.65
W HYA	11/13/78	1225 (.75)		.17
	12/13/78	1364 (.79)		.25
	2/13/79	1280 (.73)		.41
	3/15/79	1516 (.64)		.49
	4/24/79	2115 (.59)		.59
	12/4/79	1682 (.79)		.17
	12/31/79	1494 (.83)		.24
	5/22/80	1413 (.57)	[n.d.]	.60
	11/12/80	951 (.41)	[n.d.]	.04
	6/6/81	546 (.29)		.58

TABLE 7 continued

SOURCE	DATE	v = 1	v = 2	OPT.‡ PHASE
R AQR	2/13/79	56		.97
	3/13/79	127		.04
	4/24/79	144		.15
U HER	11/13/78	215 (.33)		.14
	12/13/78	157 (.38)		.22
	2/13/79	49 (.19)		.37
	3/15/79	118 (.36)		.44
	4/24/79	[n.d.]		.54
	12/5/79	109 (.33)		.08
	5/22/80	65 (.07)	[n.d.]	.50
χ CYG	11/13/78	220 (.30)		.09
	2/13/79	292 (.37)		.31
	3/13/79	326 (.43)		.38
	4/24/79	[n.d.]		.48
	12/4/79	412 (.30)		.03
	12/30/79	378 (.28)		.10
	5/22/80	260 (.24)	7	.45
	11/13/80	350 (.19)	[n.d.]	.88
	6/7/81	560 (.39)	230 (.68)	.38
R CAS	11/12/78	225 (.96)		.52
	12/12/78	152 (1.0)		.58
	2/13/79	291 (.88)		.73
	3/13/79	283 (.85)		.80
	4/24/79	330 (.72)		.89
	12/5/79	289 (.73)		.41
	1/1/80	35 (.92)		.48
	5/22/80	386 (.83)	[n.d.]	.81
	11/12/80	129 (.74)	[n.d.]	.22
	6/7/81	85 (.44)		.70
IK TAU	12/4/79	640 (.76)		.17
	12/29/79	294 (.76)		.22
	5/22/80	190 (.74)	[n.d.]	.53
	11/13/80	881 (.60)	[n.d.]	.90
	6/7/81	456 (.49)		.34

TABLE 7 continued

SOURCE	DATE	v = 1	v = 2	OPT.‡ PHASE
TX CAM	11/12/78	174 (.97)		.32
	12/13/78	101 (.98)		.37
	2/14/79	[n.d.]		.48
	3/13/79	[n.d.]		.53
	4/24/79	55 (1.0)		.60
	12/5/79	40 (1.0)		.99
	12/30/79	160 (.92)		.04
	5/22/80	94 (.79)	[n.d.]	.29
	11/13/80	76 (.57)		.61
	6/7/81	271 (.72)		.98
VX SGR	11/12/78	343 (.14)		.91
	2/13/79	617 (.23)		.04
	3/13/79	730 (.20)		.07
	4/24/79	927 (.22)		.13
	12/4/79	1011 (.21)		.44
	1/1/80	1097 (.18)		.47
	5/22/80	1260 (.21)	[n.d.]	.67
	11/12/80	923 (.21)		.91
	6/7/81	1246 (.24)		.19
VY CMA	11/17/78	1434 (.34)		
	12/13/78	1423 (.32)		
	2/15/79	1243 (.30)		
	3/13/79	1765 (.32)		
	4/24/79	1655 (.35)		
	12/5/79	1639 (.32)		
	5/22/80	1082 (.43)		
	11/13/80	1066 (.40)	[n.d.]	
	6/7/81	1054 (.45)		
ORION	12/12/78	1674 (.49)		
	2/13/79	1372 (.55)		
	3/13/79	1962		
	4/24/79	1998 (.53)		
	12/29/79	1671 (.52)		
	5/22/80	1642 (.54)		
	11/13/80	1995 (.43)		
	6/7/81	2273 (.50)		

* Non-detections are indicated by "[n.d.]".

‡ Phases are from optical light curves kindly provided by J. Mattei of the American Association of Variable Star Observers.

Total velocity extent of emission. From Figure 8 it is evident that for red giant variable stars, SiO maser emission is confined within the range -8 to +14 km s^{-1} relative to the stellar velocity, while the terminal expansion velocities in the circumstellar envelopes of these sources are in the range 4-20 km s^{-1} (cf. Table 1, column 3). The average total velocity extent of the emission is 10 km s^{-1}, with no significant difference in width between the J=1-0 and J=2-1 lines. For the supergiants (VX Sgr, VY CMa), both the expansion velocities and the SiO maser velocity extent are considerably larger than for the Mira variables, reaching values as large as 25-30 km s^{-1} for the relative velocity of SiO and ~35 km s^{-1} for V_{exp}.

Several sources in the present study (e.g., R Leo, W Hya, R Cas) exhibit SiO maser emission at relative velocities which exceed the (admittedly not well-determined) envelope terminal expansion velocity. The SiO velocities may, therefore, be unrelated to mass outflow, or, on the other hand, may indicate a high degree of turbulence in the SiO line formation region.

Comparison of different transitions: Coincidence of features. At a single epoch, the spectra of the J=1-0 rotational transitions in different vibrational states show a marked resemblance to each other in velocity structure, while the J=2-1, v=1 profile looks quite different (and is usually simpler). In an effort to quantify the extent of the coincidence of velocity structure in the v=1, J=1-0 and v=2, J=1-0 transitions, 32 pairs of simultaneous spectra covering ten different sources

were examined for coincidence of features in the two transitions. A feature was taken to be coincident in the two transitions only if a strong, easily distinguishable emission spike in one transition coincided to within 0.5 km s^{-1} with a spike in the other transition which clearly stood out from the background or general blending of features. From this sample, 18 features were found to be present only in the v=1 transition, 26 features only in v=2, while 110 pairs of "matched" features (within 0.5 km s^{-1}) were identified. Thus there is a very high probability (~71%) that distinguishable spikes at the same velocity will be present in both transitions. None of the sources examined were deficient in coincident features.

Emission features in the weak v=3, J=1-0 transition are also found to correspond closely in velocity with prominent features in the lower J=1-0 states. Although not all strong features in the v=1 and 2, J=1-0 states have detectable counterparts in v=3, J=1-0, the v=3 features always occur at velocities which also emit strongly in v=1 and v=2. Due to sensitivity limitations, v=3 profiles usually consist of one or more maser spikes, although "pedestal" emission over a range as broad as 6-9 km s^{-1} is also sometimes seen (e.g., W Hya, Nov. 1979; TX Cam, Feb. 1980). High sensitivity filterbank spectra of the v=3, J=1-0 line in VY CMa show continuous broad emission over the entire range of velocities from ~18 km s^{-1} to 44 km s^{-1} (V_{lsr}), with stronger narrow spikes rising out of the background.

A similar test for velocity coincidence between the J=1-0 and J=2-1 transitions was made but was necessarily less stringent due to

non-simultaneity of the 43 GHz and 86 GHz observations. For this reason, comparisons were made only of spectra from closely spaced runs in April 1979, November-December 1979, and November 1980. Of ~107 identifiable features (from 11 different sources) in the v=1, J=1-0 transition, only ~24% were found to be also emitting in the v=1, J=2-1 line. A similarly low percentage of the total number of identifiable features in v=1, J=2-1 were also found at v=1, J=1-0. Although selection and matching of "features" is obviously a fairly subjective process, the conclusion of low correspondence of velocity structure between different rotational transitions of the same vibrational state and high similarity of profiles in the same rotational transition of different vibrational states is quite secure.

Comparison of different transitions: Intensity ratios. Knowledge of the intensity ratios of different transitions observed at the same time is important for elucidation of the SiO maser pump mechanism and for construction of detailed source models. Such comparisons have been hindered in the past because of the limited data available and because the existence of systematic phase-dependent variations in the line ratios could not be ruled out. From their observations of 11 stars at two different epochs, Schwartz, Waak, and Bologna (1979) concluded that the peak and integrated intensities of the v=2, J=1-0 line are usually greater than in v=1, J=1-0. From their sample, they obtained an average value for the ratio Q of the v=1 and v=2 integrated intensities of

$$\langle Q \rangle = \left\langle \frac{I\ (v=1,\ J=1-0)}{I\ (v=2,\ J=1-0)} \right\rangle = 0.94 \quad ,$$

On the other hand, the integrated flux values in Table 1 of Spencer et al. (1981) for 39 sources observed at a single epoch yield a value of $\langle Q \rangle = 1.60$, suggesting that on the average, the v=1, J=1-0 line is in fact stronger than the v=2, J=1-0 line in the same star.

The present large data set confirms the conclusion of Spencer et al. that the v=1, J=1-0 integrated fluxes tend to be stronger than those for v=2, J=1-0. The total integrated fluxes in the J=1-0 transitions are listed in Table 6. The average value of Q obtained for 74 pairs of v=1 and v=2 integrated fluxes is 1.49, in good agreement with Spencer et al.'s value of 1.6.

Values of the ratio Q for each source were plotted versus stellar optical phase to determine if flux ratios in the two vibrational states exhibit any systematic variations related to the stellar pulsation cycle. Although the v=1, J=1-0 to v=2, J=1-0 integrated flux ratio varied with time, (for some sources by factors as large as 6 to 8), no systematic phase-dependent variations were detected for any of the sources in Table 6. Instead, the variations appear to be due to the combined effects of essentially random changes in the ratios of individual features.

Ratios of the integrated fluxes in the J=2-1 and J=1-0 lines of the v=1 state were likewise examined by comparing observations at the

two frequencies made within 1-2 weeks of each other. The total integrated fluxes in the J=2-1, v=1 transition are listed in Table 7. The 32 pairs of integrated flux values obtained from four near-simultaneous 86 GHz and 43 GHz observing sessions result in an average value for the ratio R of

$$\langle R \rangle = \left\langle \frac{I\ (v=1,\ J=2-1)}{I\ (v=1,\ J=1-0)} \right\rangle = 2.39 \quad .$$

All observed sources (Tables 6 and 7) have been included in this average except χ Cyg, which appears clearly anomalous; the two values of R for this source are an order of magnitude greater than the values for all the other sources. In fact, all but two of the remaining 32 values of R cluster very close to 2: ($\langle R \rangle_{30} = 2.06$), indicating that for most sources, the photon emission rates ($\sim I/\nu$) in the v=1, J=2-1 and v=1, J=1-0 transitions are essentially equal, (a conclusion also arrived at theoretically by Kwan and Scoville (1974)). No systematic phase-dependent variations were found in the 2-1/1-0 ratio.

An average value for the integrated flux ratio of the v=1, J=1-0 and v=3, J=1-0 lines was also computed, by excluding observations where only an upper limit (or questionable detection) in the v=3 line was measured. For 20 observations covering six different sources, we obtain:

$$\left\langle \frac{I\ (v=1,\ J=1-0)}{I\ (v=3,\ J=1-0)} \right\rangle = 25.2 \quad .$$

SiO photon emission rates. In order to determine the intrinsic SiO maser output of different sources, the maximum SiO photon luminosity, L_p, for each of four transitions was computed by assuming the maser radiation is isotropic:

$$L_p = \frac{S\ 4\pi\ d^2}{h\ \nu} \quad (\text{photons sec}^{-1}) \quad ,$$

where S is the maximum integrated SiO line flux and d is the distance. The distances used were taken from the literature (see Table 8, col. 2); most values were derived using the period-absolute magnitude relation for Miras and either the apparent visual magnitude at mean maximum or the $\lambda 1.04\mu$ magnitude at mean maximum. In most cases, the distances appear to be uncertain by ~20%, although derived values which differ by factors of two or three are sometimes encountered (e.g., χ Cyg, see below).

Values for the maximum SiO photon luminosities are given in columns 3-6 of Table 8. In the v=1, J=1-0 line, they range from $\sim 5 \times 10^{42}$ photons s^{-1} for the Mira variables χ Cyg and Mira to $\sim 1 \times 10^{46}$ photons s^{-1} for the supergiants VX Sgr and VY CMa. The relatively low SiO maser output for Mira is consistent with the non-detectability of the thermal ground state (v=0, J=2-1) SiO line in this source (Lambert and Van den Bout 1978; Olofsson et al. 1982) and may be due to photodestruction of SiO molecules by UV radiation from Mira's white dwarf companion (Cahn and Elitzur 1979). In the case of χ Cyg, if

TABLE 8

SiO PHOTON LUMINOSITY

SOURCE	DISTANCE (pc)	MAXIMUM SiO PHOTON LUMINOSITY (photons sec^{-1})			
		v=1, J=1-0	v=2, J=1-0	v=3, J=1-0	v=1, J=2-1
R LEO	238 (1)	1.32 (44)	1.03 (44)	1.11 (43)	1.07 (44)
MIRA	77 (1)	5.44 (42)	4.70 (42)		6.46 (42)
U ORI	239 (1)	3.64 (43)	2.84 (43)		2.19 (43)
W HYA	135 (2)	6.59 (43)	7.86 (43)	6.74 (42)	8.07 (43)
R AQR	200 (3)	1.12 (43)	5.06 (42)		1.21 (43)
U HER	322 (1)	1.95 (43)	1.75 (43)		4.67 (43)
χ CYG	132 (4)	4.92 (42)	2.79 (42)		2.04 (43)
R CAS	230 (1)	7.56 (43)	3.24 (43)		4.28 (43)
IK TAU	270 (5)	1.88 (44)	1.38 (44)	2.47 (42)	1.35 (44)
TX CAM	696 (2)	9.23 (44)	7.56 (44)	8.44 (43)	2.75 (44)
VX SGR	1500 (6)	1.03 (46)	8.51 (45)	3.82 (44)	5.94 (45)
VY CMA	1500 (7)	1.34 (46)	8.82 (45)	1.33 (45)	8.32 (45)
ORION	500 (8)	1.35 (45)	8.52 (44)		1.19 (45)

References for distances:

(1) Lepine & Paes de Barros 1977
(2) Cahn & Elitzur 1979
(3) Wallerstein & Greenstein 1980
(4) Hinkle, Hall, & Ridgway 1982
(5) Hyland et al. 1972
(6) Lockwood & Wing 1982
(7) Herbig 1969
(8) Genzel et al. 1981

the distance is taken to be 393 pc (Barnes 1978, priv. comm.; quoted by Morris et al. 1979; see also Lambert and Van den Bout 1978) rather than the value of 132 pc found by Hinkle et al. (1982), then the photon luminosities for this source are increased by a factor of ~10 and are no longer anomalously low. Regardless, the sources have an intrinsic spread in SiO luminosity of at least three orders of magnitude. By comparison, the OH luminosities of Type I and Type II sources spread over factors of only ~50 and ~70, respectively (Nguyen-Q-Rieu et al. 1979). H_2O masers in Mira variables have photon emission rates quite comparable to the SiO rates, although no direct correlation is found for individual sources (Lepine et al. 1978). It will be noted below that the ratio of maximum and minimum SiO flux for individual sources is also significantly greater than the range of OH maser variability observed for individual sources; however, both are at least an order of magnitude smaller than the intrinsic dispersion in the distribution of their respective maser luminosities.

SiO luminosity - period relation. Since the stellar luminosities of Mira variables are known to be well-correlated with the stellar pulsation period (at least for periods between 200 and 500 days; Clayton and Feast 1969; Foy et al. 1975), and the SiO luminosity appears to be correlated with the stellar luminosity (Cahn and Elitzur 1979; Cahn 1981), it is natural to expect the SiO luminosity may also be correlated with period. Such is indeed the case. The maximum SiO photon luminosities in the v=1, J=1-0 transition are plotted versus stellar period in

Figure 9. SiO photon luminosities vs. stellar period. Maximum photon luminosities in the v=1, J=1-0 line are from Table 8. Dashed lines connect points for R Leo and χ Cyg where discrepant distances have been reported (see text).

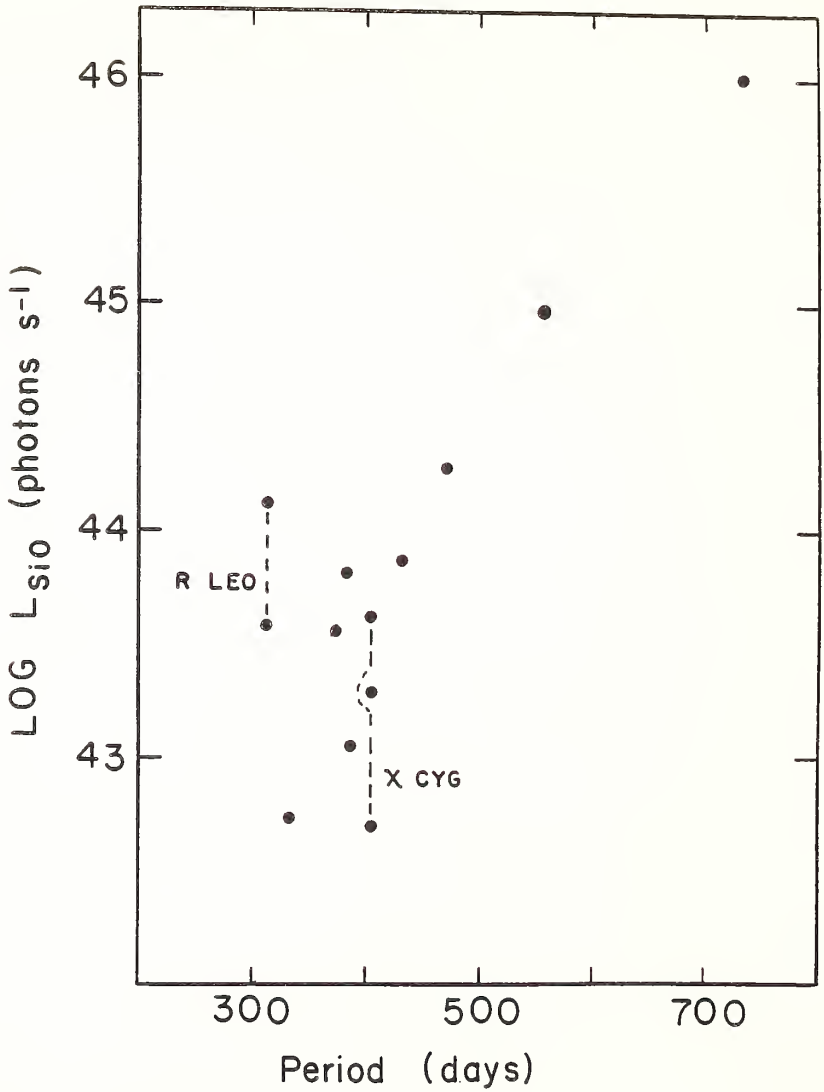
46
45
44
43
LOG L_{SiO} (photons s^{-1})
R LEO
X CYG
300
500
700
Period (days)

Figure 9. A similar correlation between OH luminosity and stellar period was not found by Nguyen-Q-Rieu et al. (1979).

Comparison with stellar light curves. The SiO integrated fluxes in the v=1, J=1-0; v=2, J=1-0; and v=1, J=2-1 lines are plotted against time, along with the stellar visual light curves, in Figure 10(a-m). For each source, the J=1-0, v=1 and v=2 data are plotted with equivalent flux scales, while the scale for the J=2-1 data is compressed by a factor of two to represent comparable changes in photon flux. The visual light curves are shown in magnitudes and are derived from data kindly provided by the AAVSO. The vertical lines on the plots mark the dates of visual maximum. Filled symbols indicate SiO measurements obtained at FCRAO, while open symbols show 43 GHz data from Haystack. It can be seen that the relative calibration of the data from the two observatories is quite good. In addition, values of integrated flux obtained at Bonn at a single epoch (May 1979) in the J=1-0 lines have been taken from the literature (Spencer et al. 1981) and are plotted as +'s. These data also seem quite consistent with our calibration.

The plots show that the SiO flux for most sources exhibits both periodic variations which correlate with the stellar pulsation cycle and secular variations. The total integrated SiO line flux for these thirteen sources varied by factors of ~2 - 30 over the $2\frac{1}{2}$ year period of the observations, with the range of variability being somewhat smaller at 86 GHz than at 43 GHz. The general characteristics of the SiO "light curves" fall into four general categories, which will be discussed briefly below.

Figure 10(a-m). SiO integrated flux in three transitions versus time for thirteen sources. Solid symbols (● for v=2, J=1-0; ▲ for v=1, J=1-0; ■ for v=1, J=2-1) are data from FCRAO, open symbols are from Haystack. The pluses (+) show data in the J=1-0 lines observed at Bonn (Spencer et al. 1981). The visual light curves are shown at the bottom of each plot (data courtesy of AAVSO); the vertical lines mark dates of optical maximum.

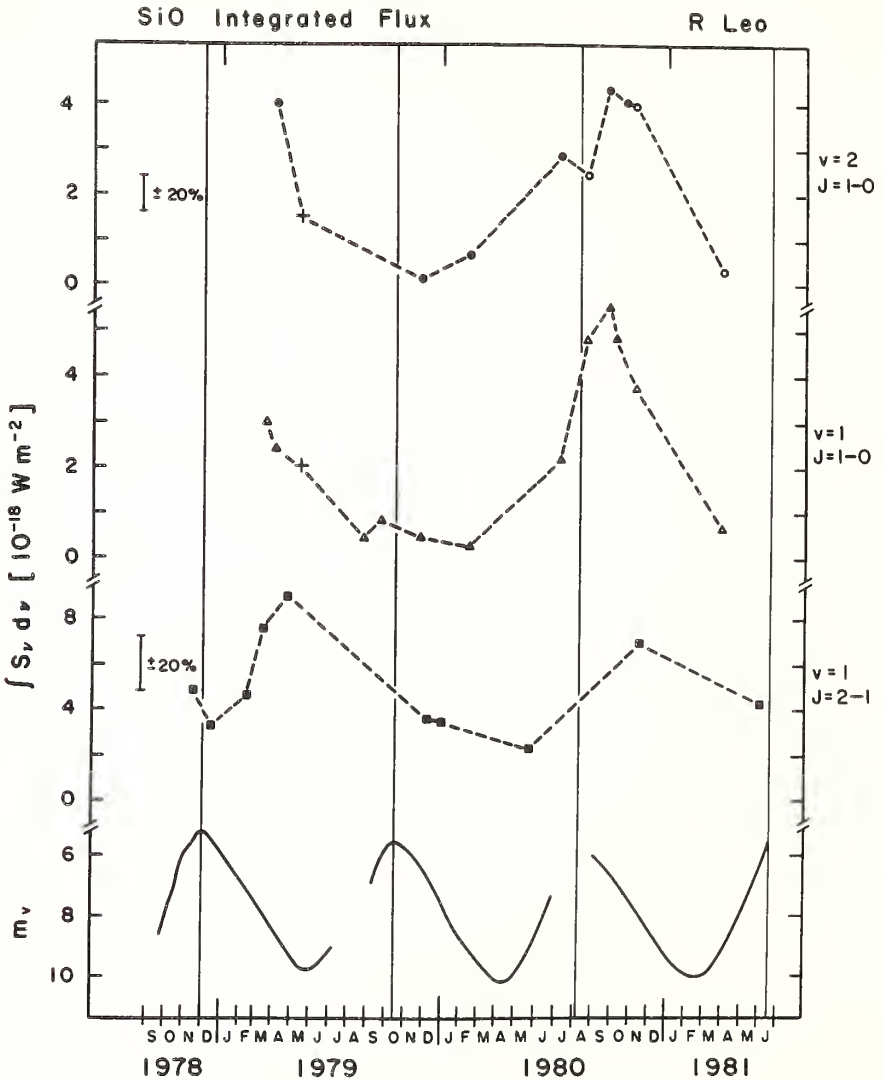
SiO Integrated Flux
R Leo
v = 2
J = 1–0
v = 1
J = 1–0
v = 1
J = 2–1
± 20%
± 20%
$\int S_\nu d\nu$ [10^{-18} W m^{-2}]
m_v
S O N D J F M A M J J A S O N D J F M A M J J A S O N D J F M A M J
1978
1979
1980
1981

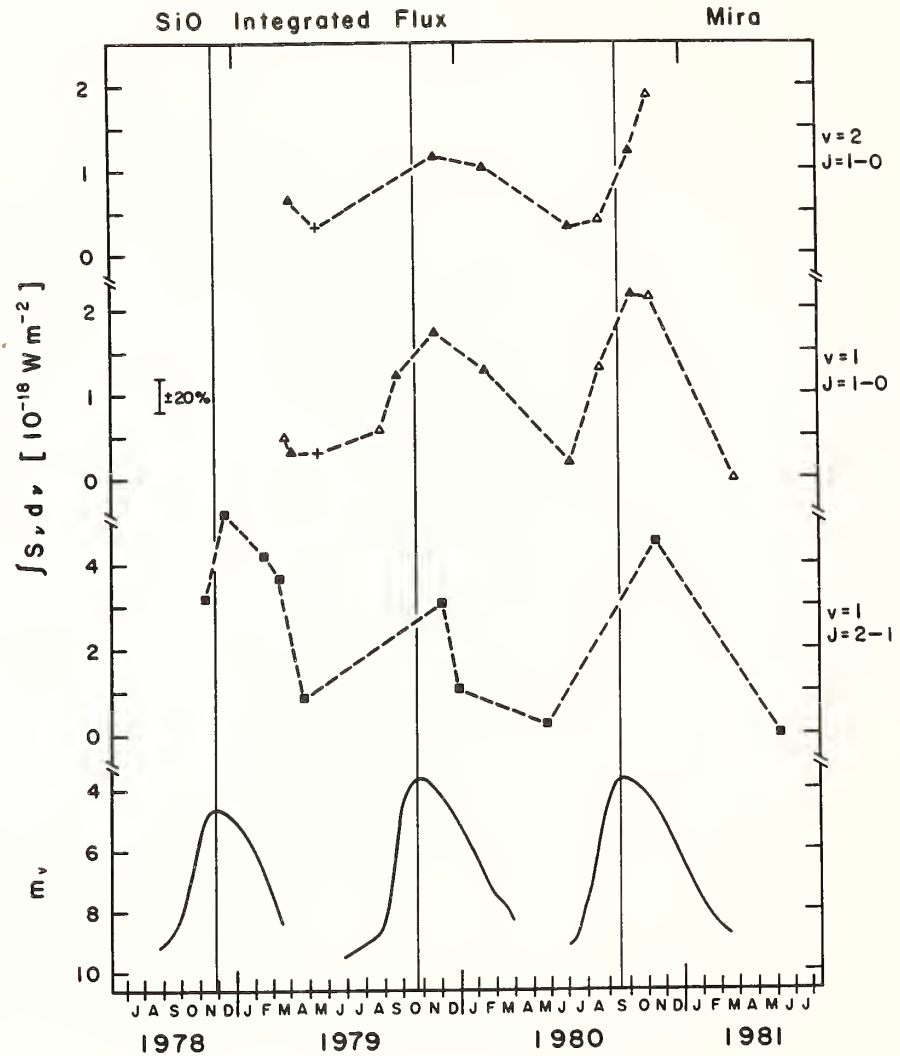
SiO Integrated Flux
Mira
v=2
J=1-0
v=1
J=1-0
v=1
J=2-1
±20%
$\int S_\nu d\nu$ [10^{-18} W m^{-2}]
m_v
J A S O N D J F M A M J J A S O N D J F M A M J J A S O N D J F M A M J J
1978
1979
1980
1981

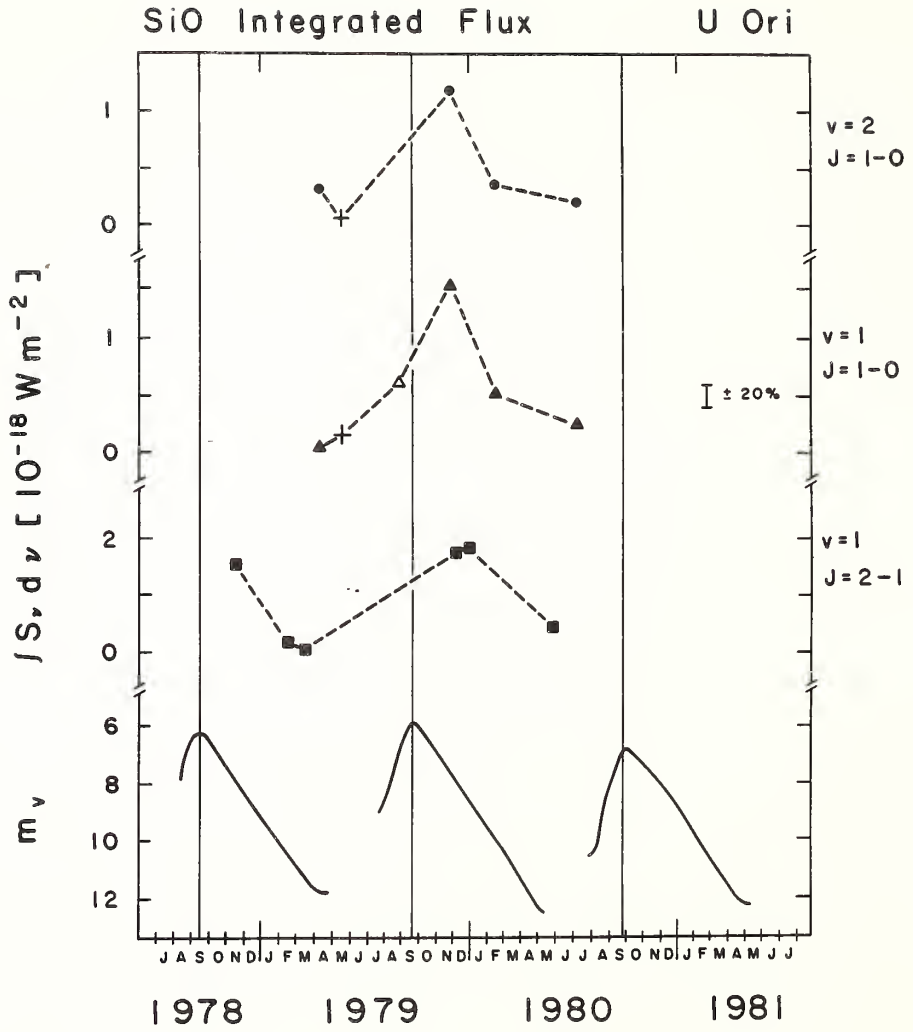
SiO Integrated Flux
U Ori
v = 2
J = 1-0
v = 1
J = 1-0
v = 1
J = 2-1
± 20%
m_v
∫S_ν dν [10^-18 W m^-2]
J A S O N D J F M A M J J A S O N D J F M A M J J A S O N D J F M A M J J
1978
1979
1980
1981

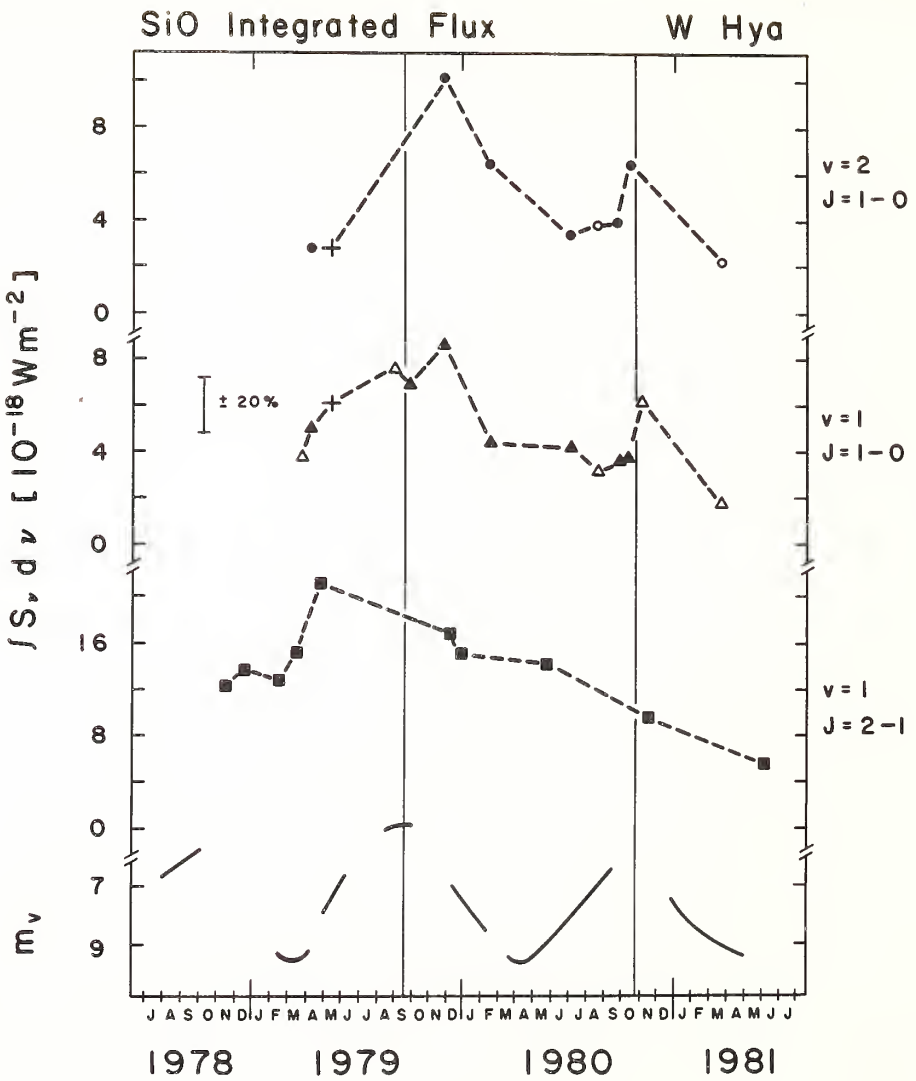
SiO Integrated Flux
W Hya
$\int S_\nu d\nu$ [10^{-18} Wm^{-2}]
± 20%
v = 2
J = 1 – 0
v = 1
J = 1 – 0
v = 1
J = 2 – 1
m_v
J A S O N D J F M A M J J A S O N D J F M A M J J A S O N D J F M A M J J
1978
1979
1980
1981

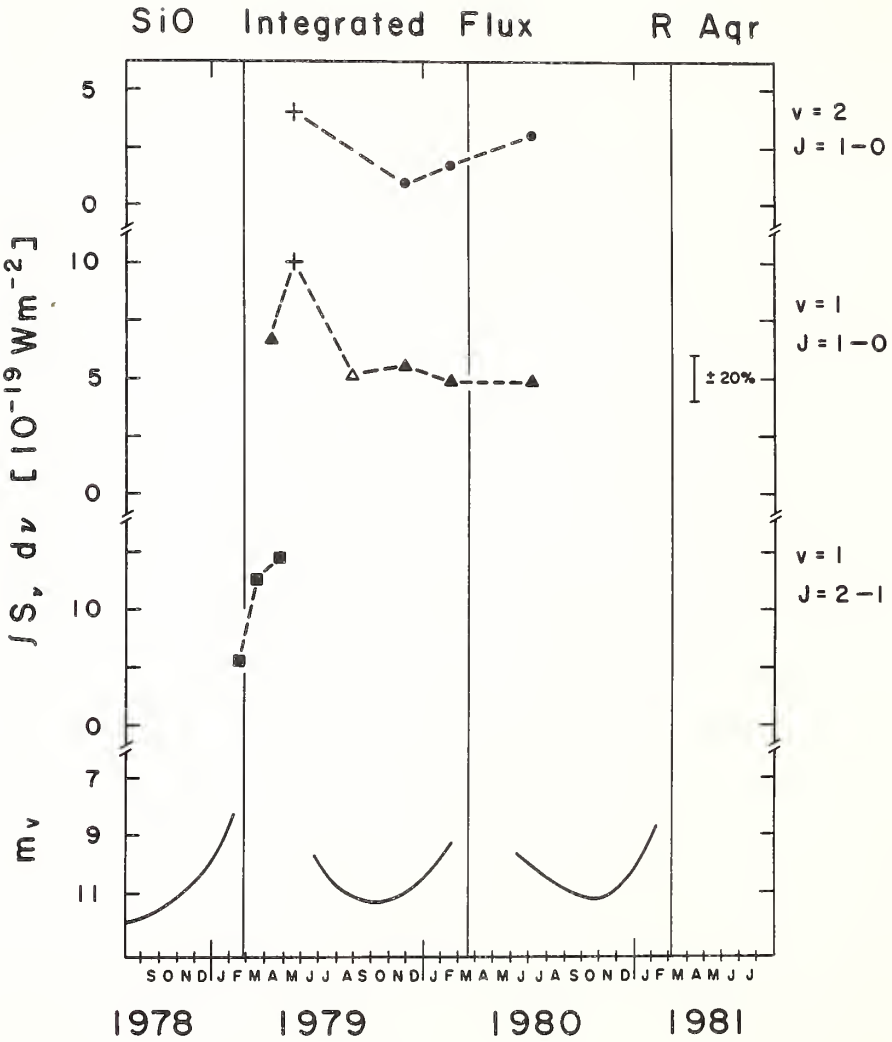
SiO Integrated Flux R Aqr
$\int S_\nu d\nu$ [10^{-19} Wm^{-2}]
m_v
v = 2
J = 1−0
v = 1
J = 1−0
v = 1
J = 2−1
± 20%
S O N D J F M A M J J A S O N D J F M A M J J A S O N D J F M A M J J
1978
1979
1980
1981

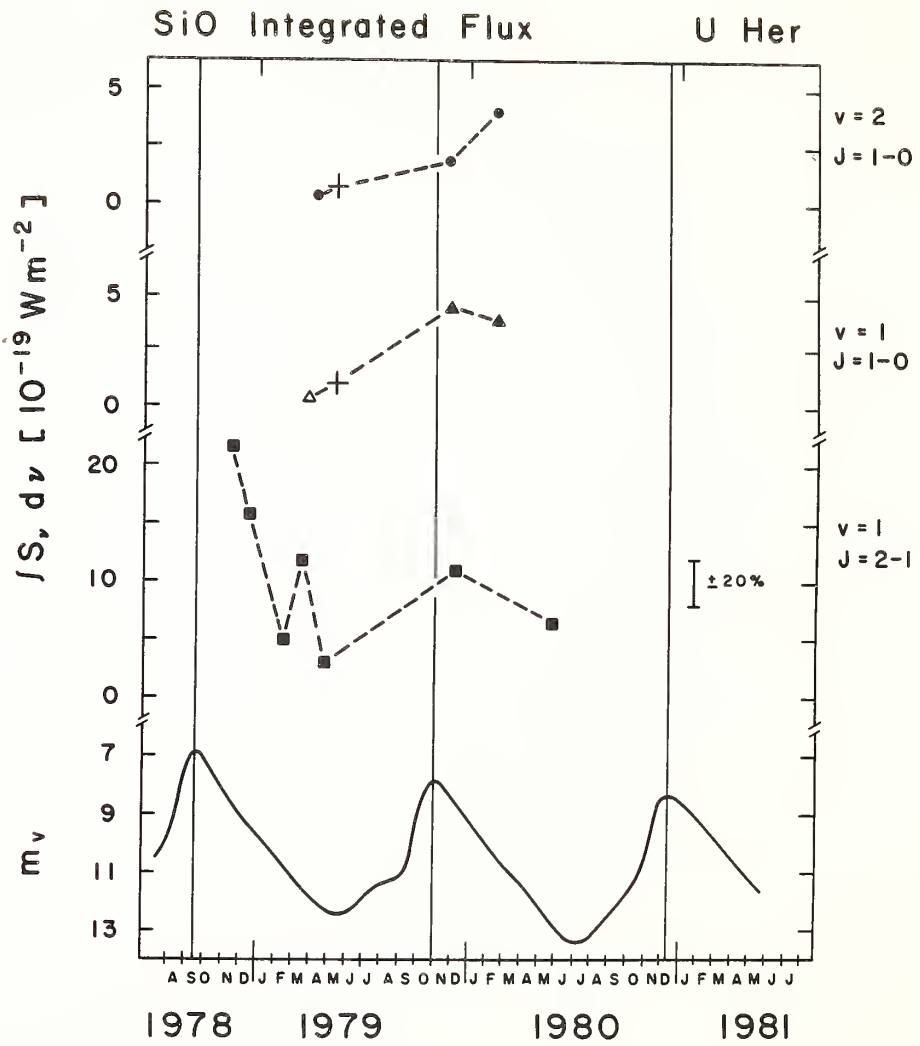
SiO Integrated Flux
U Her
∫S, dv [10⁻¹⁹ Wm⁻²]
5
0
5
0
20
10
0
v = 2
J = 1-0
v = 1
J = 1-0
v = 1
J = 2-1
±20%
m_v
7
9
11
13
A SO ND J FM AM J J A SO ND J FM AM J J A SO ND J FM AM J J
1978
1979
1980
1981

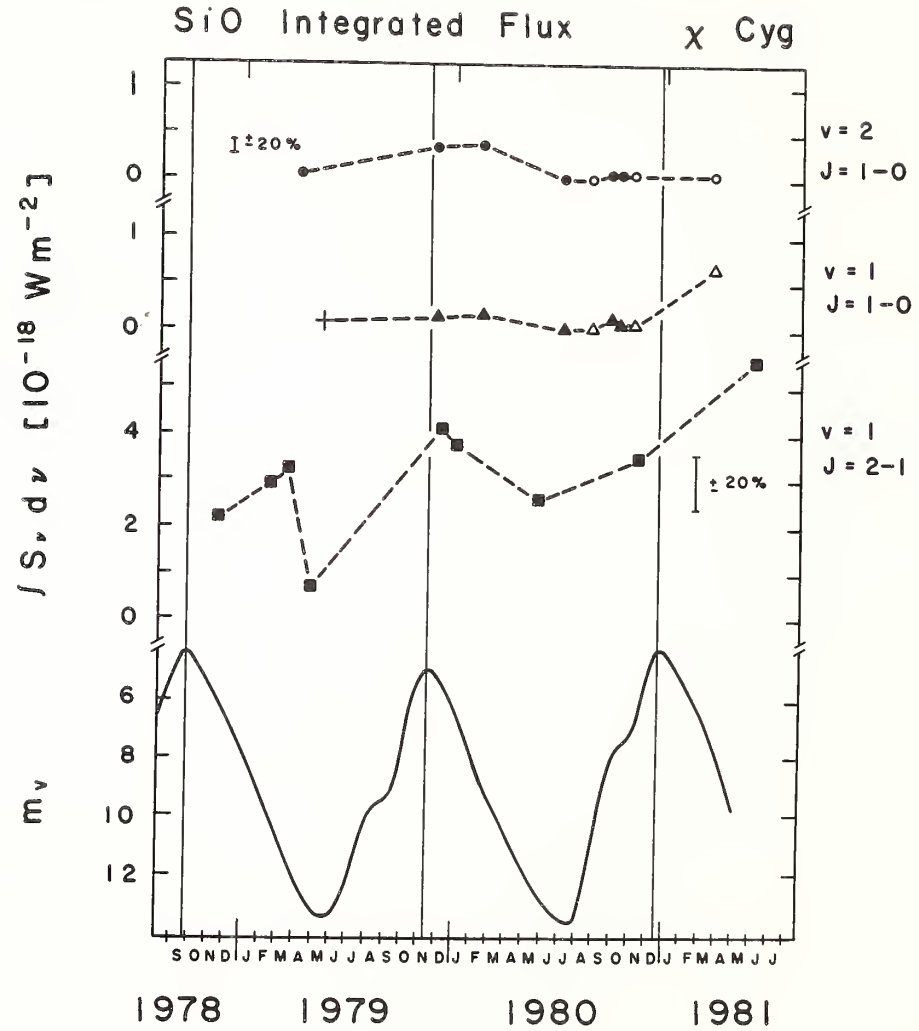
SiO Integrated Flux
χ Cyg
I ± 20%
v = 2
J = 1–0
v = 1
J = 1–0
v = 1
J = 2–1
± 20%
$\int S_\nu d\nu$ [10^{-18} Wm^{-2}]
m_v
1
0
1
0
4
2
0
6
8
10
12
S O N D J F M A M J J A S O N D J F M A M J J A S O N D J F M A M J J
1978
1979
1980
1981

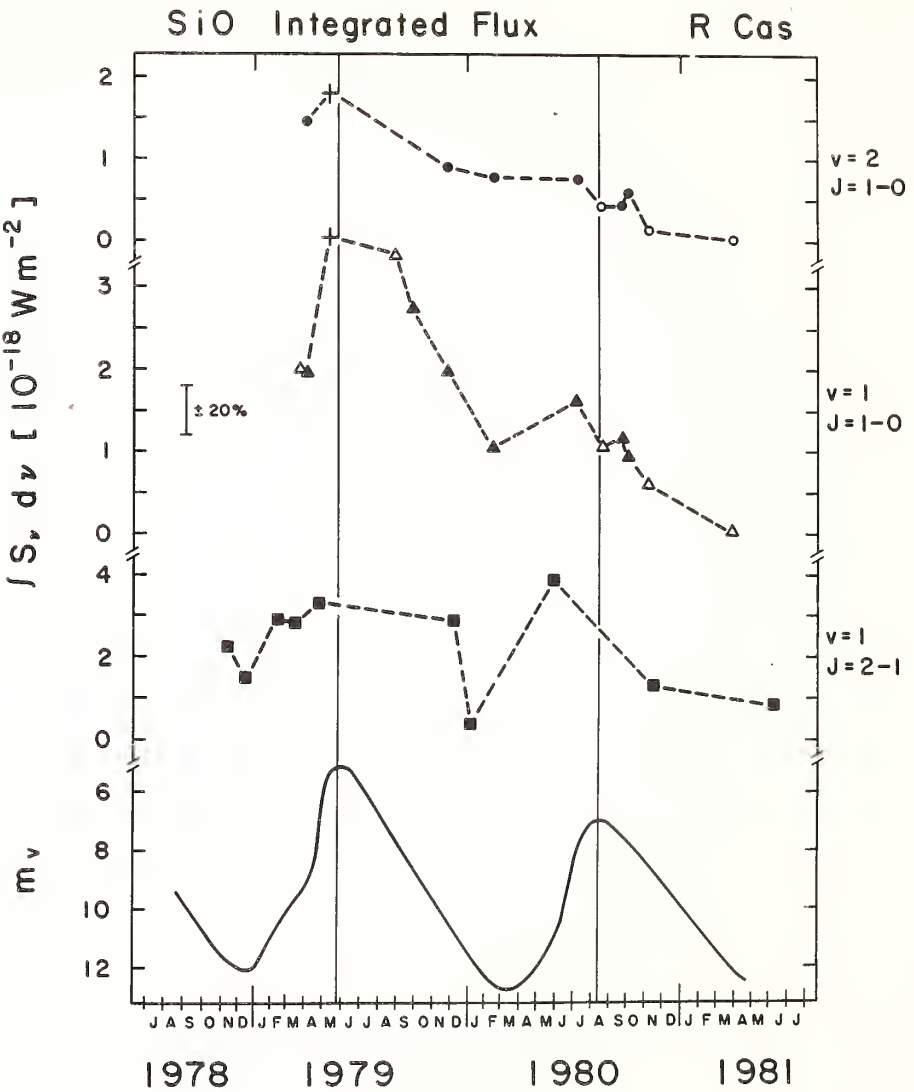
SiO Integrated Flux
R Cas
$\int S_\nu \, d\nu$ [10^{-18} $W m^{-2}$]
± 20%
v = 2
J = 1-0
v = 1
J = 1-0
v = 1
J = 2-1
m_v
J A S O N D J F M A M J J A S O N D J F M A M J J A S O N D J F M A M J J
1978
1979
1980
1981

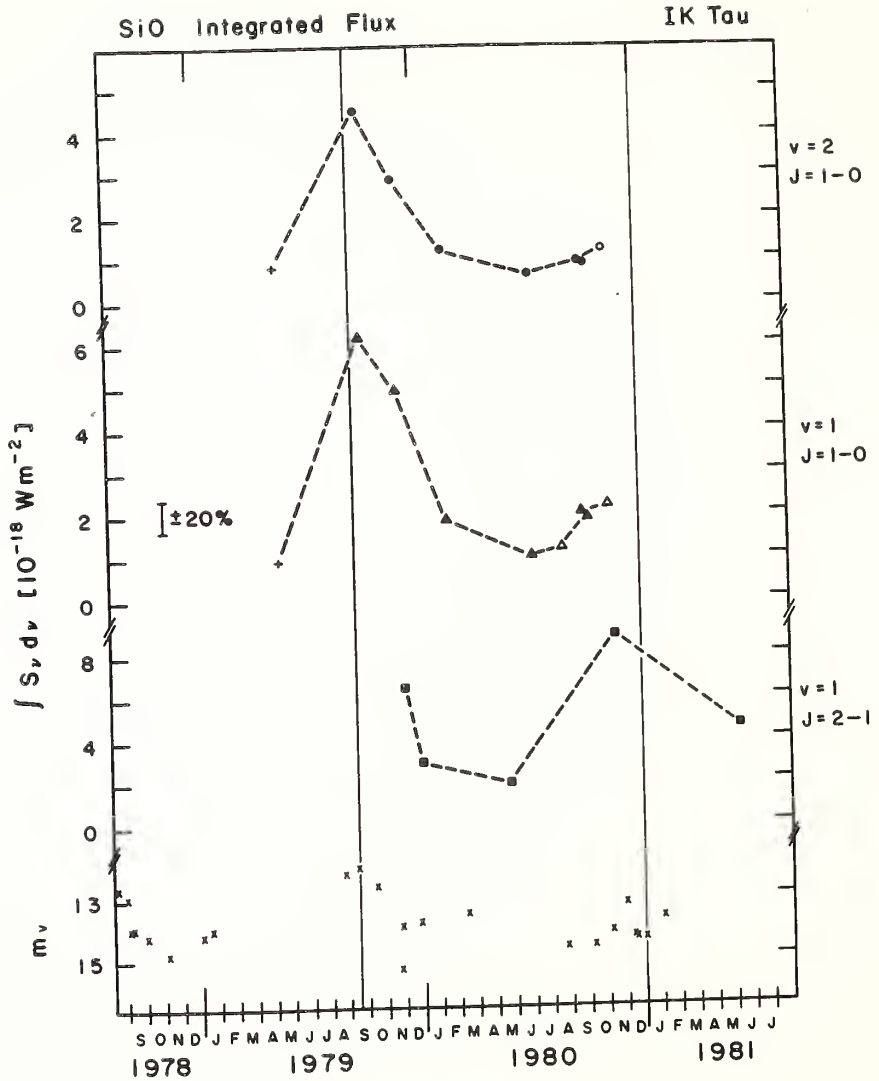
SiO Integrated Flux
IK Tau
v = 2
J = 1–0
v = 1
J = 1–0
v = 1
J = 2–1
±20%
$\int S_\nu d\nu$ [10^{-18} Wm^{-2}]
m_v
S O N D J F M A M J J A S O N D J F M A M J J A S O N D J F M A M J J
1978
1979
1980
1981

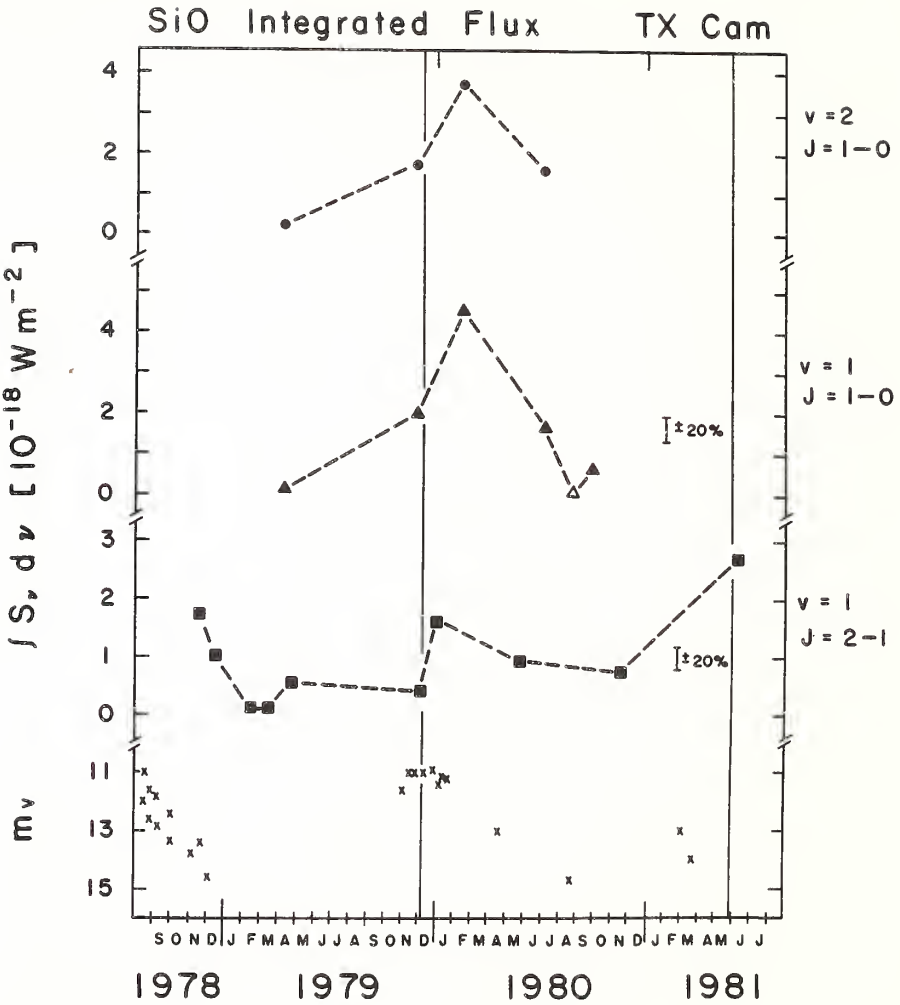
SiO Integrated Flux TX Cam
v = 2
J = 1−0
v = 1
J = 1−0
v = 1
J = 2−1
±20%
±20%
∫ S_ν dν [10^-18 W m^-2]
m_v
S O N D J F M A M J J A S O N D J F M A M J J A S O N D J F M A M J J
1978
1979
1980
1981

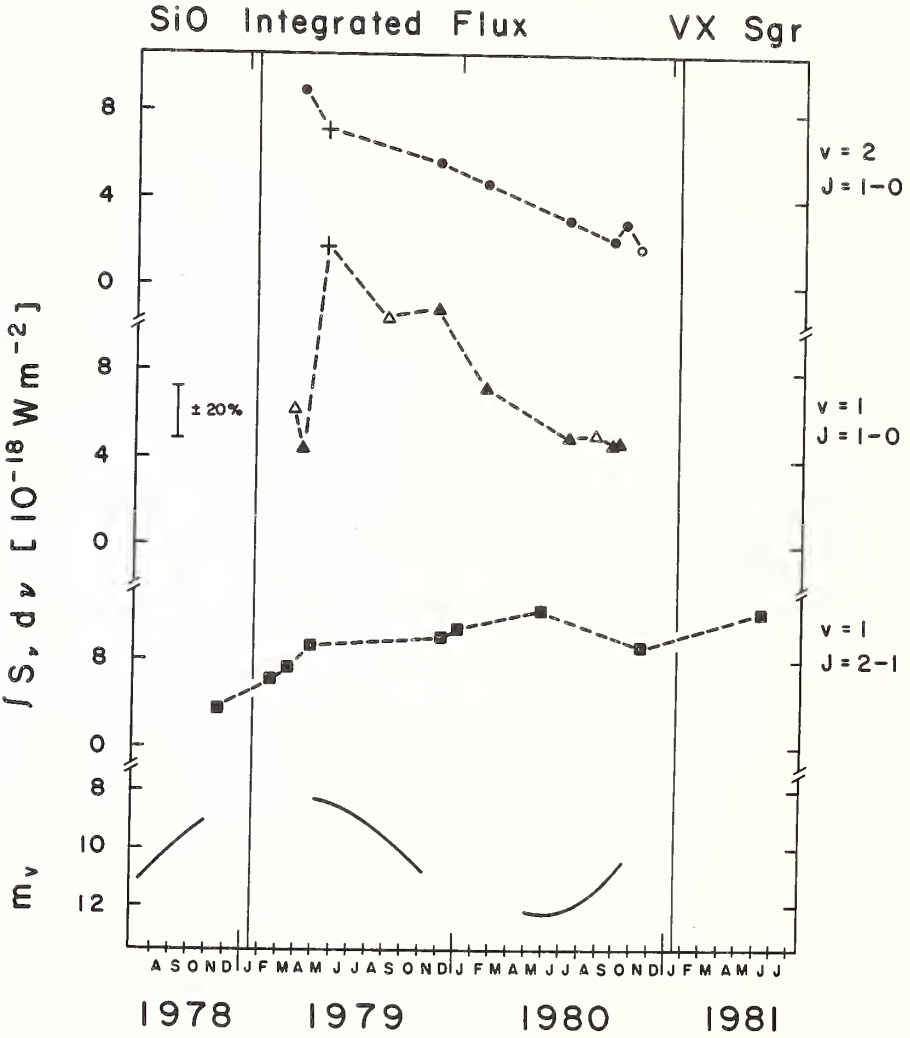
SiO Integrated Flux
VX Sgr
v = 2
J = 1-0
v = 1
J = 1-0
v = 1
J = 2-1
± 20%
$\int S_\nu d\nu$ [10^{-18} W m^{-2}]
m_v
A S O N D J F M A M J J A S O N D J F M A M J J A S O N D J F M A M J J
1978
1979
1980
1981

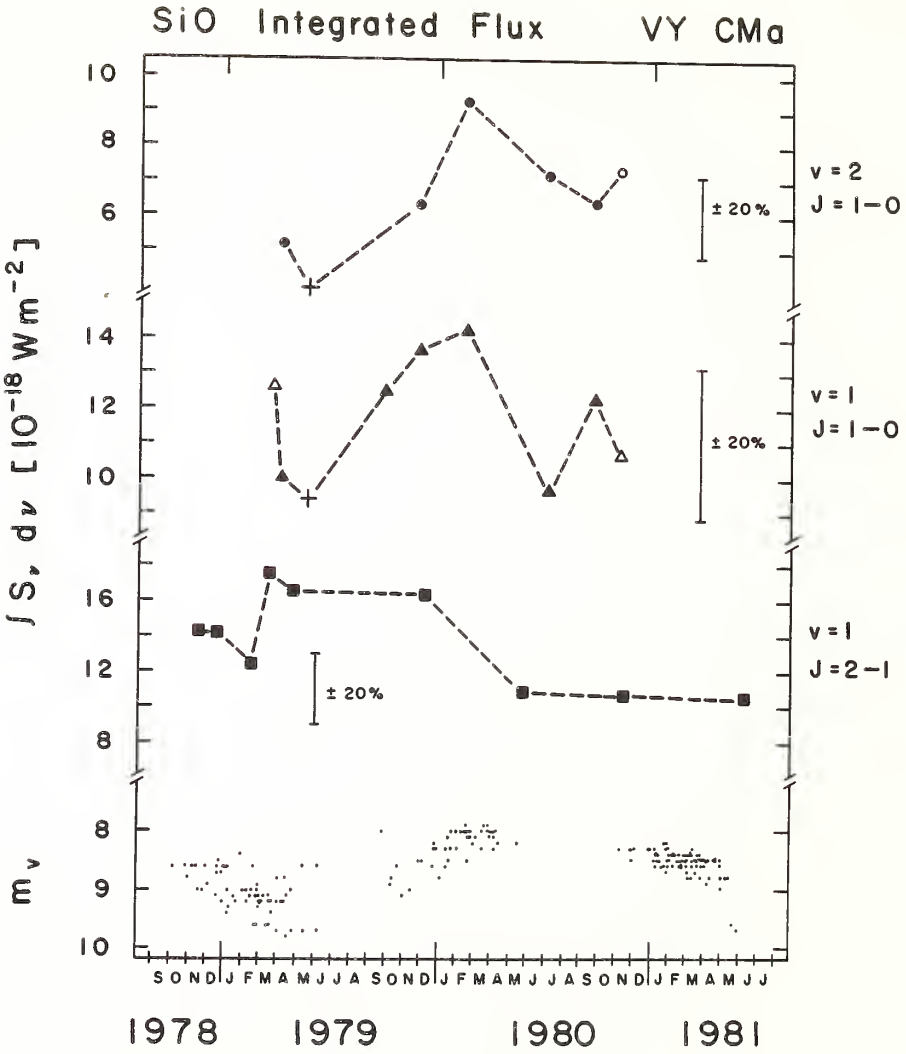
SiO Integrated Flux
VY CMa
∫S, dv [10⁻¹⁸ Wm⁻²]
v = 2
J = 1−0
± 20%
v = 1
J = 1−0
± 20%
v = 1
J = 2−1
± 20%
m_v
S O N D J F M A M J J A S O N D J F M A M J J A S O N D J F M A M J J
1978
1979
1980
1981

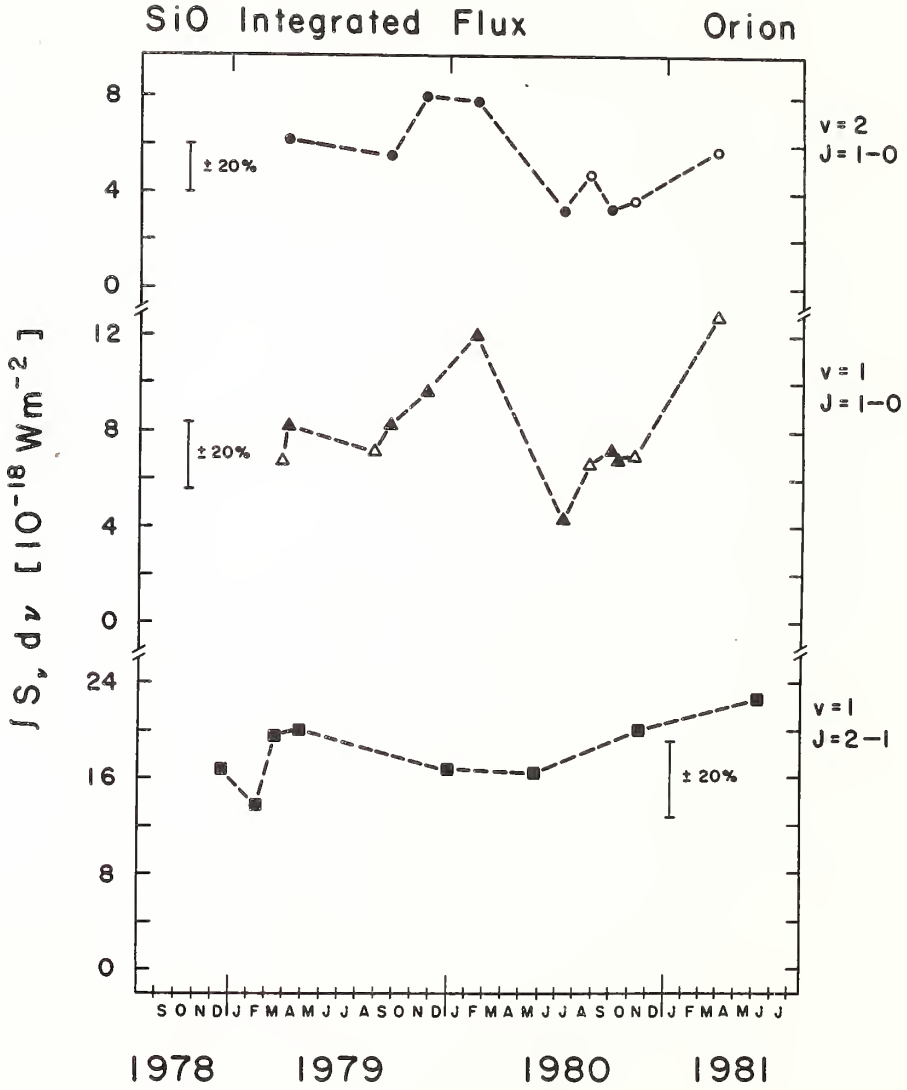
SiO Integrated Flux
Orion
v = 2
J = 1–0
v = 1
J = 1–0
v = 1
J = 2–1
± 20%
± 20%
± 20%
∫ S_ν dν [10^-18 Wm^-2]
8
4
0
12
8
4
0
24
16
8
0
S O N D J F M A M J J A S O N D J F M A M J J A S O N D J F M A M J J
1978
1979
1980
1981

For at least six sources (R Leo, Mira, U Ori, W Hya, IK Tau, and TX Cam), the shapes of the SiO light curves in the v=1, J=1-0 and v=2, J=1-0 transitions are extremely similar. It is clear that whatever is causing the flux variations affects the J=1-0 transitions in the two vibrational states in very much the same way. Although the sampling is different (and somewhat sparser) for the v=1, J=2-1 transition, the data for the above six sources are for the most part consistent with a similar variability here as well.

The SiO light curves of three sources (R Cas, VX Sgr, χ Cyg) show considerable dissimilarity in the three transitions. For R Cas, although both the v=1 and v=2, J=1-0 lines show an overall decline in flux from early 1979 to early 1981, the variations in v=1, J=1-0 are more extreme and, in addition to the overall decline, show some correlation with the optical variations. The v=1, J=2-1 variations are more erratic than the J=1-0 fluxes, with little indication of either periodicity or long-term secular trends. In the supergiant VX Sgr, the v=1, J=2-1 line shows a gradual, steady increase in flux, while the v=2, J=1-0 line shows a steep decline and v=1, J=1-0 is possibly correlated with the optical variations with a phase lag of roughly 0.2-0.3 period. In spite of the unusually large amplitude of its optical variations, χ Cyg shows little indication of correlated SiO flux or similarity of behavior in the three transitions.

The variations in the v=1, J=1-0 and v=2, J=1-0 lines of VY CMa and Orion show some similarity to each other but are primarily erratic.

For both of these sources, the v=1, J=2-1 light curves show no correspondence with the J=1-0 variations and the total flux in this transition is roughly constant (to within the calibration uncertainties of ~±20%).

For the relatively weak sources R Aqr and U Her, the sampling is insufficient to draw firm conclusions about the relative variations of total integrated flux in different transitions, although there may be some tendency for SiO flux to peak shortly after optical maximum.

If the SiO maser emission is radiatively pumped, a correlation of SiO flux with infrared light would be expected. Light curves in the near-infrared have been published for most of the sources in the present study. Observations of Mira and R Leo at λ2.7μ are given by Maran et al. (1977) and for U Ori, W Hya, U Her, VX Sgr, and VY CMa at several wavelengths between 1.2 and 10μ by Harvey et al. (1974). These curves show a high degree of repeatability from cycle to cycle, which allows extrapolation from the existing curves to the interval covered by the SiO observations of the present study. In general, the maxima of the IR light curves of long period variables lag the visual maxima by ~0.1-0.2 period (Petit and Nicholson 1933; Lockwood and Wing 1971), while the IR minimum tends to be coincident with or to precede the visual minimum (Maran et al. 1977).

Although radiative pumping of the SiO masers may provide an explanation for the observed correlation of SiO and infrared light curves,

the observations do not definitely rule out the possibility of collisional pumping. The rise in the IR light curve from minimum to maximum is found to be associated with an increase in photospheric temperature (Lockwood and Wing 1971), which may produce sufficient changes in the collision rates to affect the maser pump. Alternatively, the maser variations may be related to temperature induced changes in the thermal line width, Δv_D, since the maser amplification path length is determined by the distance over which the velocity varies by $\sim\Delta v_D$ (Genzel et al. 1979). In contrast, for the case of OH masers in the outer regions of circumstellar envelopes ($R \sim 100\text{-}1000\ R_*$), radiative pumping is the most likely coupling mechanism between the OH and IR variations since the masers are located too far from the star for propagation of density or pressure waves over timescales consistent with the lack of an observed phase lag between the OH and IR light curves (Harvey et al. 1974; Fillit et al. 1977; Jewell et al. 1979). Although the situation for H_2O masers is less clearcut, radiative pumping is also commonly invoked for these sources to explain the correlation between H_2O maser and infrared variations (e.g., Schwartz et al. 1974).

Time variations of velocity structure. While the previous section referred to the time variability of the total integrated flux, this section will address the question of the general stability of the line profiles and the typical lifetimes of features. The existence of quasi-periodic flux variations is not accompanied by periodic or repeatable changes in the velocity structure of the SiO profiles. Instead, the

changes in profile shape appear to be of a secular nature; no evidence was found for any cycle-to-cycle repeatability of profile shape. Various phase-dependent velocity structure characteristics were searched for in the data and none were found. Since systematic phenomena applicable to many sources were not discovered, the behavior of several individual sources will be described below.

R Cas. The general shape of the v=1, J=1-0 profile is quite constant over nine observations covering an entire light cycle (431 days), from visual phase 0.19 (Aug. 1979) through the following maximum to phase 0.20 (Nov. 1980; see Fig. 5h). In particular, the strongest feature (probably a blend) at V_{lsr}=29 km s^{-1} persists over all phases, with only minor jitter (~0.5-1.0 km s^{-1}) in the velocity of the peak. The v=1, J=1-0 spectrum, however, is quite different at the preceeding phases 0.82-0.85 (Mar-Apr. 1979), when the peak emission was shifted several km s^{-1} and a minimum was present where the 29 km s^{-1} peak subsequently appeared. These changes may be further evidence for the perturbations of velocity structure near phase 0.9 which Clark et al. (1981) report occurred in R Cas in late July 1980 (the next cycle). These authors attribute the transient profile changes to the passage of a shock wave through the SiO line formation region. Our observations in early July 1980, however, show no evidence at ϕ = 0.92 for the disturbance observed by Clark et al. three weeks later. Nor were any similarly transient velocity perturbations at late stellar phases observed in any other source during our observing period.

The v=1, J=2-1 spectra for R Cas (Fig. 6h) provide another good example of profile stability over many months, followed by drastic changes and non-repeatable velocity structure. The non-repeatability is particularly well demonstrated by a comparison of the spectrum at ϕ = 0.73 (Feb. 1979), which shows exclusively redshifted emission and a single narrow spike, with the spectrum at the following ϕ = 0.70 (June 1981), where peak emission appears at the stellar velocity accompanied by weaker blueshifted emission. Just as there is no correlation between the presence of redshifted or blueshifted emission and stellar phase, there is no tendency evident for stellar velocity masers to occur at particular light cycle phases.

R Leo. Both the v=1, J=1-0 and v=2, J=1-0 data for this source (see Fig. 5a) likewise show many spectra dominated by a single strong (blended) feature near V_* which persists over a wide range of phases covering more than one light cycle (e.g., Feb. 1980-Mar. 1981). While the integrated flux varies by a factor of ~20, the basic profile shape is stable (except for some transient low-level redshifted emission). However, comparison of spectra at identical phases from two different cycles (e.g., ϕ~0.40: Mar.-Apr. 1979 and Feb. 1980) reveals completely different profile structure at the two epochs: broad, multiple-component, entirely redshifted emission on the one hand, and a narrow, symmetric, stellar velocity feature on the other. The v=1, J=2-1 spectra for R Leo show similar discrepancies in profile shape from one cycle to the next (cf. ϕ~0.95: Nov. 1978 and June 1981; ϕ~0.27: Feb.

1979, late Dec. 1979, Nov. 1980). Evidently, the factors which determine which velocity regimes can produce maser emission are not directly influenced by the stellar light or pulsation cycle, but must be related either to transient inhomogeneities in the maser regions or to variations with a longer timescale than the stellar period. Although the maser profiles sometimes change radically in appearance within 2-3 months (the typical sampling interval here), stability over several hundreds of days is not uncommon.

W Hya. The J=1-0 spectra for this source (Fig. 5d) exhibit a wide range of profile shapes, with an interesting evolutionary sequence from a single, narrow component at V_* (Mar.-Apr. 1979), to double-peaked, predominantly redshifted emission (Aug.-Sept. 1979), to complex, multiple-component structure covering a broad velocity range (Nov.-Feb. 1980), and eventually returning to strong stellar velocity emission (Sept. 1980-Mar. 1981). None of these changes appear to be systematically related to stellar optical phase. Furthermore, the velocity structure changes in the J=1-0 lines do not correspond to any similar changes in the v=1, J=2-1 line; (this result is hardly surprising given the scarcity of coincident features between the two rotational transitions as described in an earlier section).

VY CMa. Although relative intensities vary from one epoch to the next, most features persist over at least the 20 months spanned by the observations. There is some evidence for small changes in the velocities of features, on the order of ~1 km s^{-1}.

Obviously, other interesting examples of erratic and perplexing line profile variations could be mentioned. However, the three major conclusions are: 1) in spite of large changes in flux, individual features often have lifetimes at least as long as several hundred days, 2) velocity structure variations bear no evident relation to the stellar light and pulsation cycle, and 3) no correspondence is found between velocity structure changes in the J=1-0 and J=2-1 lines of the v=1 state. This last observation strengthens the conclusion that these lines must be formed in different regions of the stellar atmosphere or circumstellar shell.

Longer term variations: Comparisons with published data. A complete understanding of the time variability characteristics of SiO maser emission requires the accumulation of well-sampled data over a longer time span than was feasible for the present study. Sporadic observations, usually of only one transition at any given time, have been published by many researchers for most of the sources studied here since SiO masers were discovered in late 1973. Detailed conclusions which can be made based on this inhomogeneous and sparsely sampled data are limited and are further hindered by the lack of consistency in velocity resolution, signal-to-noise ratio, and calibration and by the lack of simultaneous observations of the various transitions. Nonetheless, a few comments are warranted based on comparisons of the present data with earlier observations.

Although nearly all of the sources in the present study were observed to exhibit a clear predominance of redshifted emission over the

entire $2^1/2$ year observing period (at least in J=1-0, v=1 and v=2), earlier published spectra show that at least three of these sources have exhibited more symmetric profiles or even predominance of blueshifted emission at some earlier epochs. For example, significant long-term variations have occurred in the J=1-0 lines from R Leo. While the velocity extent of the v=1, J=1-0 line observed in June 1974 (Snyder and Buhl 1975) and in June 1976 (Balister et al. 1977) is almost entirely redshifted from V_*, in Jan. 1977 (data of Snyder et al. 1978) a strong feature at V_* appeared, with "pedestal" emission only slightly shifted to the red. Over the following few months, the redshifted emission gradually disappeared and blueshifted emission became dominant. The v=1, J=1-0 and v=2, J=1-0 profiles observed by Schwartz et al. (1979) in Feb. 1977 show emission more or less centered about V_*, while in June 1977 (Schwartz et al. 1979) and Aug. 1977 (Lepine et al. 1978) the emission is almost entirely blueshifted. The earliest data reported in this thesis (Mar. 1979) shows the R Leo J=1-0 lines are once again redshifted, an asymmetry which persists throughout 1979 and (to a lesser degree) at least until Mar. 1981. The changes which occur in the velocity range of emission involve both strong maser spikes and pedestal emission, if present. (However, there is no implication that individual maser features are actually shifting in velocity; it is more likely that features at one velocity die out while new ones at another velocity turn on).

Long-term changes in the velocity range of emission have also occurred in the J=1-0 lines toward Mira. The v=1, J=1-0 spectrum in

June 1974 (Spencer and Schwartz 1975) appears to have approximately equivalent amounts of redshifted and blueshifted flux, while in June 1976, the v=1 and v=2 spectra of Balister et al. (1977) are entirely blueshifted. In Feb. 1977 (Schwartz et al. 1979), the v=1 flux is mostly blueshifted, v=2 is mostly redshifted (although coincident features appear in the spectra), and by June 1977, v=2 is entirely redshifted (and v=1 is too weak to detect). In Aug. 1977, the v=1 line from Mira (Lepine et al. 1978) is again symmetric about V_*.

Spectra of one or more of the J=1-0 lines from W Hya have been reported for the following epochs: June 1974 (Snyder and Buhl 1975), June 1976 (Balister et al. 1977), Jan. 1977 (Snyder et al. 1978), Feb. 1977 (Schwartz et al. 1979), Aug. 1977 (Schwartz et al. 1979, Lepine et al. 1978), and Oct. 1977 (Scalise and Lepine 1978). These spectra all show profiles which are fairly symmetric about V_*. No clearcut evidence is seen for the larger velocity extent of redshifted emission and predominance of flux from redshifted gas which is so striking in the spectra from Apr. 1979 through July 1980 (see Fig. 5d).

Published J=1-0 spectra for R Cas at a number of epochs between 1974 and 1978 (e.g., Spencer and Schwartz 1975, Snyder and Buhl 1975, Snyder et al. 1978, Schwartz et al. 1979, Moran et al. 1979) are in agreement with the spectral characteristics shown in the present work (Fig. 5h); all show mostly redshifted emission. A weak stellar velocity feature appeared along with the stronger redshifted component in Jan.-Feb. 1977 (Snyder et al. 1978, Schwartz et al. 1979).

The above descriptions, based on visual impressions from spectra which often have lower signal-to-noise and lower velocity resolution than those presented in this thesis, are necessarily qualitative and rather imprecise. However, the conclusion remains that, although redshifted emission seems to be strongly favored in most sources in the J=1-0 lines, blueshifted emission may dominate at certain epochs.

Rotational transitions of states with $v \geq 3$. Previous to this study, detections of maser emission in the J=1-0 transition of the v=3 state have been reported by Scalise and Lepine (1978) for VX Sgr and W Hya and by McIntosh, Lane, and Clemens (1980) and Spencer et al. (1981) for VY CMa. We report here additional positive detections of this transition in R Leo, TX Cam, and IK Tau. Thus, six of the twelve sources which were searched repeatedly in v=3, J=1-0 showed detectable emission (see Table 6 and spectra in Fig. 5). For the giant variable stars, the line was only detectable relatively close to stellar optical maximum (i.e., ϕ_V between 0.9 and 0.3); no v=3 detections were made for these sources at optical phases between 0.3 and 0.9. The v=3, J=1-0 emission from the supergiant VX Sgr persisted to somewhat later phases (e.g., 0.42-0.54), but still disappeared at very late phases. It thus appears that, like the lower v states, v=3 maser emission is correlated with the stellar light cycle.

At an epoch when the SiO emission from R Leo underwent a particularly bright flare (i.e., Aug.-Oct. 1980; see Figs. 5a, 10a), emission from higher vibrational states and from two isotopes of SiO was

searched for. While the peak intensity of the v=3, J=1-0 line was 135 Jy, an upper limit of 9 Jy (3σ) was set for the following transitions: v=4, J=1-0; v=5, J=1-0; ^{29}SiO v=1, J=1-0; and ^{30}SiO v=1, J=1-0. Maser emission from isotopes of SiO in the ground vibrational state (v=0, J=2-1) was subsequently detected in Orion by Olofsson, Hjalmarson, and Rydbeck (1981) and in VY CMa by Deguchi et al. (1982).

C H A P T E R I I I.

VLBI OBSERVATIONS OF SiO MASERS

§1. Introduction

Since the apparent angular size of maser sources is much smaller than the beamwidth of even the largest radio telescope, questions concerning the detailed geometry and structure of SiO masers can only be addressed by means of interferometry. Techniques of VLBI have previously been applied to the study of the OH and H_2O masers associated with both long period variables and star formation regions. Since the angular resolution of a two-element interferometer is proportional to the wavelength of observation divided by the distance between the two telescopes, the relatively shorter wavelengths of SiO masers require only modest separations between antennas. An attempt to observe the SiO maser in Orion with an 845 km (Haystack-Green Bank) baseline resulted in a complete resolving out of the emission (Moran et al. 1977).

Three spectral line VLBI experiments on SiO masers at 43 GHz have been performed using the FCRAO 13.7 m telescope and the Haystack Observatory 36.6 m telescope. The 75 km baseline produces a fringe spacing of 0.02 arcsec, which is ideal for observations of SiO masers associated with late type stars at typical distances of a few hundred parsecs. In the first experiment in July 1978, results were obtained on the v=1, J=1-0 transition in two sources and were reported by Moran et

al. (1979). This experiment firmly established that the SiO emission is due to maser processes and determined that the strongest features in the spectra of R Cas and VX Sgr have brightness temperatures of 1-2 x 10^{10} K. Results from the second and third experiments, where both v=1 and v=2, J=1-0 were observed, are reported in this Chapter.

The primary purpose of these experiments was to compare the properties of the v=1, J=1-0 and v=2, J=1-0 masers and to study their spatial structure. The similarities apparent in the velocity structure of these two transitions were found to be also reflected in similar visibilities; all features were at least partially resolved, corresponding to apparent spot sizes for the masers of 0.2-4.0 x 10^{14} cm. For the third experiment, improvements in receiver sensitivity over the previous experiments permitted the first mapping of SiO maser features to be made by analysis of relative phase as a function of time. Maps of the spatial distribution of maser features are presented for VX Sgr in the v=1, J=1-0 and v=2, J=1-0 lines and for R Cas in v=1, J=1-0. Spatial offsets of ~10^{15} cm were measured between features in the v=1, J=1-0 spectra of both Orion and VY CMa.

§2. Observations and Data Reduction

For the second SiO VLBI experiment, which took place Oct. 31 -Nov. 2, 1978, the FCRAO antenna was equipped with an uncooled λ7mm mixer receiver with a SSB receiver temperature of ~2000 K; the receiver tem-

perature of the Haystack uncooled mixer was ~1800 K (SSB). For the third experiment on Sept. 24-30, 1979, the mixers at both stations had SSB receiver temperatures of ~800 K. The local oscillators at both sites were phase-locked to hydrogen maser frequency standards. Both antennas had horizontally polarized feeds. Data were recorded on video tapes with the standard Mark II tape recording system (Clark 1973) and were correlated with the NRAO Mark II VLB processor in Charlottesville, Virginia.

The sources observed during the second experiment were Orion, VX Sgr, W Hya, and R Cas in both v=1, J=1-0 and v=2, J=1-0, and R Leo in v=1, J=1-0. For the Orion observations, the local oscillator was switched in frequency by 3.3 MHz at a 0.5 Hertz rate in order to observe both velocity components at -6 and +19 km s^{-1}. The delay offset was determined by processing the SiO data with different clock delays (+12, 0, -12 μsec) until fringes were found.

During the third experiment, observations were made in both v=1 and v=2, J=1-0 of Orion (frequency switched by 2.7 MHz), VX Sgr, W Hya, R Cas, and IK Tau, and in three switch cycles (separated by 2 MHz) in the v=1, J=1-0 line for VY CMa. The sensitivity was sufficient that observations of 3C84 were used to aid in the delay calibration. A linear drift of ~1 μsec per day in the SAO hydrogen maser frequency standard at FCRAO was determined by hourly measurements of the difference between the maser and the LORAN timing signal; the clock delay used in processing is estimated to be accurate to ~0.1 μsec.

Each observation lasted about one hour and consisted of a 5-15 minute off source scan to provide the bandpass profile needed for total-power spectra, followed by a 45-50 minute scan on source. Every one to two hours, a thirty minute period was devoted to pointing checks at each telescope.

The processor calculates a 192-channel complex cross correlation function every 0.2 seconds; these were Fourier transformed into a time series of cross-power spectra with 128 complex channels (96 independent). Ninety-six channel autocorrelation functions were also computed from the data streams from each telescope. The total bandwidth was 2 MHz (13.9 km s^{-1}), which provides a velocity resolution of 0.30 km s^{-1} with Hanning weighting. The minimum detectable correlated flux density (5σ) in a 40 kHz bandwidth and 100 sec integration time for the three FCRAO-Haystack 43 GHz VLBI experiments were: Exp. I, ~350 Jy; Exp. II, ~215 Jy; Exp. III, ~100 Jy.

The theory and techniques of VLBI spectral line data analysis have been discussed in detail by Moran (1976), Benson (1978), Hansen (1980), and others. A standard package of data reduction routines was used on the IBM 360 computer at NRAO to further reduce and calibrate the SiO data and to produce maps of the relative positions of different spectral components. For the experiments reported here, the cross power spectra output by the processor were coherently averaged for 20-30 seconds. A strong spectral feature was then chosen for each source and its phase was subtracted from the data for the remaining channels. The phase

referencing procedure allowed coherent averaging of the data for 20-45 minutes by removing atmospheric and oscillator phase noise which is independent of frequency across the 2 MHz observed bandwidth.

§3. Results

Experiment II: (Oct.-Nov. 1978). The data on which fringes were successfully obtained consisted of the following: 3 scans on VX Sgr in v=1, J=1-0 (covering a 3-3/4 hour period), 2 scans on VX Sgr in v=2, J=1-0 (2 hours), 2 scans on W Hya in v=1, J=1-0 (2-1/4 hours), and 2 scans on W Hya in v=2, J=1-0 (2 hours). No fringes were found on the data for R Cas and R Leo, presumably because these sources were too weak (optical phases were 0.5 and 0.9, respectively). The results for Orion from this experiment have been discussed by Genzel et al. (1979) and preliminary results for VX Sgr and W Hya were presented by Lane et al. (1980).

Figure 11(a-b) shows total power and cross-correlated power spectra obtained for VX Sgr and W Hya. The cross power data in the v=1, J=1-0 and v=2, J=1-0 transitions were obtained on consecutive days at similar hour angle, while the total power spectra were produced by averaging autocorrelation data from Haystack. At any velocity, the ratio of the cross-correlated power to the total power gives the normalized fringe visibility. The highest peak in each cross power

Figure 11(a-b). Total power (solid line) and cross power (dotted line) spectra for a) VX Sgr, and b) W Hya (Experiment II). The upper spectrum for each source is the v=2, J=1-0 transition; lower spectra are v=1, J=1-0. The v=1 and v=2 spectra for each source were obtained at similar hour angles on the date indicated at the top of each plot. The interferometer fringe spacings for the VX Sgr spectra shown were 20.2 mas (v=1) and 20.9 mas (v=2); for W Hya they were 23.4 mas (v=1) and 25.4 mas (v=2).

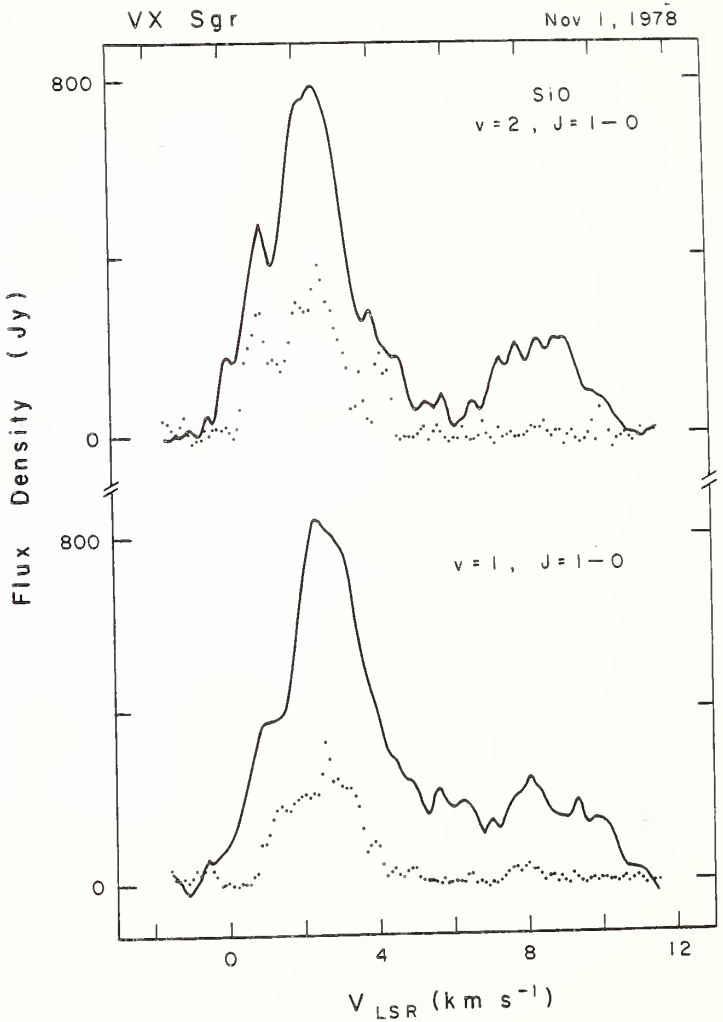
VX Sgr
Nov 1, 1978
SiO
v = 2 , J = 1 — 0
v = 1 , J = 1 — 0
800
0
800
0
Flux Density (Jy)
0
4
8
12
V LSR (km s⁻¹)

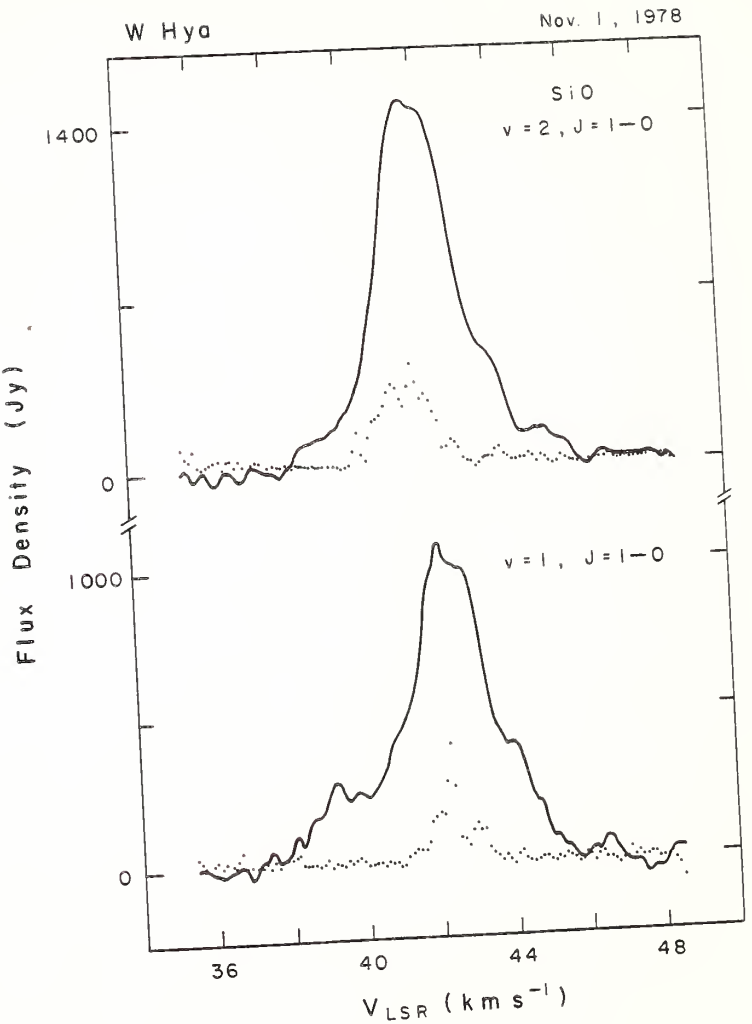
W Hya
Nov. 1, 1978
SiO
v = 2, J = 1—0
v = 1, J = 1—0
1400
0
1000
0
Flux Density (Jy)
36
40
44
48
V_LSR (km s^-1)

spectrum is the channel used as a phase reference; since the phase of this channel is set equal to zero, the amplitude of the feature is somewhat overestimated.

The VX Sgr data show evidence for at least 20 blended maser features across the spectrum, with typical line widths of ~0.5 km s^{-1}; a few features are as narrow as 0.2-0.3 km s^{-1}. Similarly, the cross power spectra for W Hya can be decomposed into at least 15 blended features with FWHP of 0.3-0.5 km s^{-1}. For this source, however, differences between the two vibrational states are evident in the velocities of partially resolved features.

The observed visibilities and other parameters of the spectra are summarized in Table 9. For each source and transition, several radial velocity ranges are listed with the corresponding range of the observed visibilities. These visibilities represent mean or typical values; the data were too sparse to warrant detailed modeling of the variations in visibility with projected baseline length. The apparent sizes of the maser features have been derived from the visibilities by assuming a model for the source brightness distribution at each velocity. We assume that the emission in a given velocity channel originates from a single location and may be represented by a circular Gaussian intensity distribution. The visibility (V) of a circular Gaussian as a function of fringe spacing (θ_f) and the FWHM source size (θ_s) is given by

$$V = \exp\left\{ \frac{-\pi^2}{4 \ln 2} \left(\frac{\theta_s}{\theta_f}\right)^2 \right\} \quad . \qquad \text{(IV-1)}$$

TABLE 9

PARAMETERS OF SiO FEATURES FROM VLBI EXPERIMENT II (Oct.-Nov. 1978)

Source	Transition	Radial Velocity Range (km s^{-1})	Visibility	Apparent Size[a] (mas)	Linear Size[b] (x 10^{13} cm)
W HYA	v=1, J=1-0	37.0-41.0	≤0.05	≥20	≥4.1
		39.4	0.58	9	1.8
		41.0-44.0	0.05-0.25	14-20	2.8-4.1
		44.0-47.0	≤0.05	≥20	≥4.1
	v=2, J=1-0	38.5-40.0	≤0.05	≥20	≥4.1
		40.1	0.44	11	2.2
		40.5-43.5	0.05-0.30	13-20	2.6-4.1
		43.5-46.0	≤0.05	≥20	≥4.1
VX SGR	v=1, J=1-0	-0.5-0.5	≤0.05	≥20	≥45
		0.5-4.0	0.15-0.55	8-15	18-34
		5.0-7.0	≤0.05	≥20	≥45
		7.0-9.0	0.10-0.25	12-16	27-36
		9.0-11.0	≤0.05	≥20	≥45
	v=2, J=1-0	-0.5-0.5	≤0.05	≥20	≥45
		0.5-4.5	0.15-0.85	4-15	9-34
		5.0-7.0	≤0.05	≥20	≥45
		7.0-9.0	0.00-0.25	≥12	≥27
		9.0-11.0	≤0.05	≥20	≥45

(a) Assumes Gaussian brightness distribution.
(b) Distances are given in Table 8.

The apparent linear sizes of the maser features are shown in column 6, using distances from Table 8. For W Hya the spot sizes for both v=1, J=1-0 and v=2, J=1-0 are in the range 2-4 x 10^{13} cm, while for the supergiant VX Sgr, the values are about an order of magnitude larger. The sizes for W Hya are comparable to those found for R Cas by Moran et al. (1979).

It is interesting to note that in both W Hya and VX Sgr the masers at the stellar velocity (40 km s^{-1} for W Hya, 6 km s^{-1} for VX Sgr) in general appear to have larger sizes (lower visibilities) than emission shifted several km s^{-1} from V*. In VX Sgr, the strong blueshifted features have higher visibilities than the redshifted features.

Experiment III: (Sept. 1979). The data on which fringes were obtained are summarized below:

TABLE 10
SiO VLBI DATA FROM EXP. III

Source	No. of Scans		Interval Covered (hours)	
	v=1, J=1-0	v=2, J=1-0	v=1, J=1-0	v=2, J=1-0
VX Sgr	4	3	4.75	4.0
R Cas	4	1	5.0	1.0
W Hya	3	3	3.5	3.5
IK Tau	2	1	2.0	1.0
VY CMa	4	-	4.0	-
Orion	6	5	7.25	6.0

Total power and cross power spectra are shown in Figure 12(a-d) for VX Sgr, W Hya, IK Tau, and R Cas. Except for R Cas, the total power

Figure 12(a-d). Total power (solid line) and cross power (dotted line) spectra for a) VX Sgr, b) W Hya, c) IK Tau, and d) R Cas (Experiment III). The upper spectrum for each source is the v=2, J=1-0 transition; lower spectra are v=1, J=1-0. The v=1 and v=2 spectra for each source were obtained at similar hour angles on the dates indicated at the top of each plot. The interferometer fringe spacings were 20.2 mas (v=1) and 21.9 mas (v=2) for VX Sgr, 19.3 mas (v=1) and 19.0 mas (v=2) for W Hya, 24.8 mas (v=1) and 24.2 mas (v=2) for IK Tau, and 28.8 mas (v=1) and 20.2 mas (v=2) for R Cas. The flux density scale was determined using the single dish data and calibration techniques described in Chapter II.

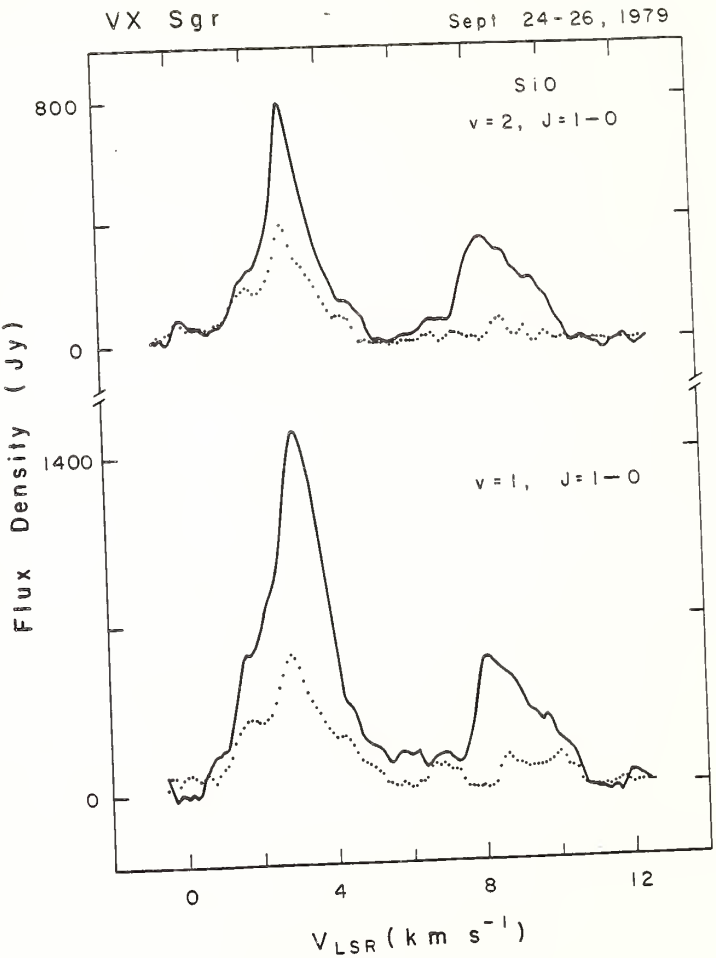
VX Sgr
Sept 24-26, 1979
SiO
v=2, J=1-0
v=1, J=1-0
800
0
1400
0
Flux Density (Jy)
0
4
8
12
V_{LSR} (km s^{-1})

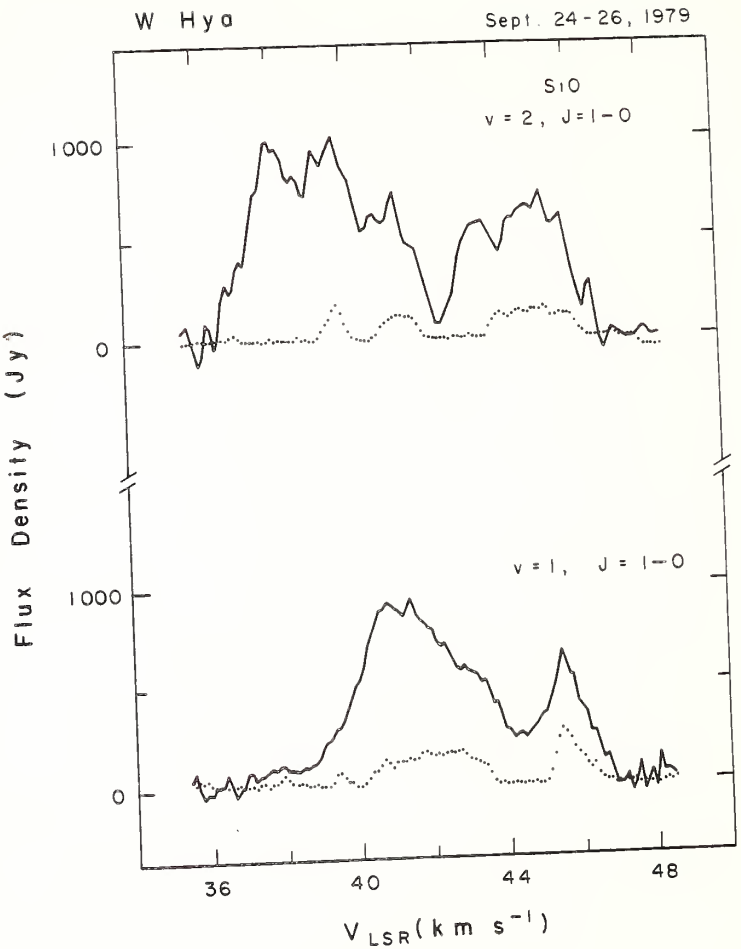
W Hya
Sept. 24-26, 1979
SiO
v = 2, J=1-0
1000
0
v = 1, J = 1-0
1000
0
Flux Density (Jy)
36
40
44
48
V LSR (km s-1)

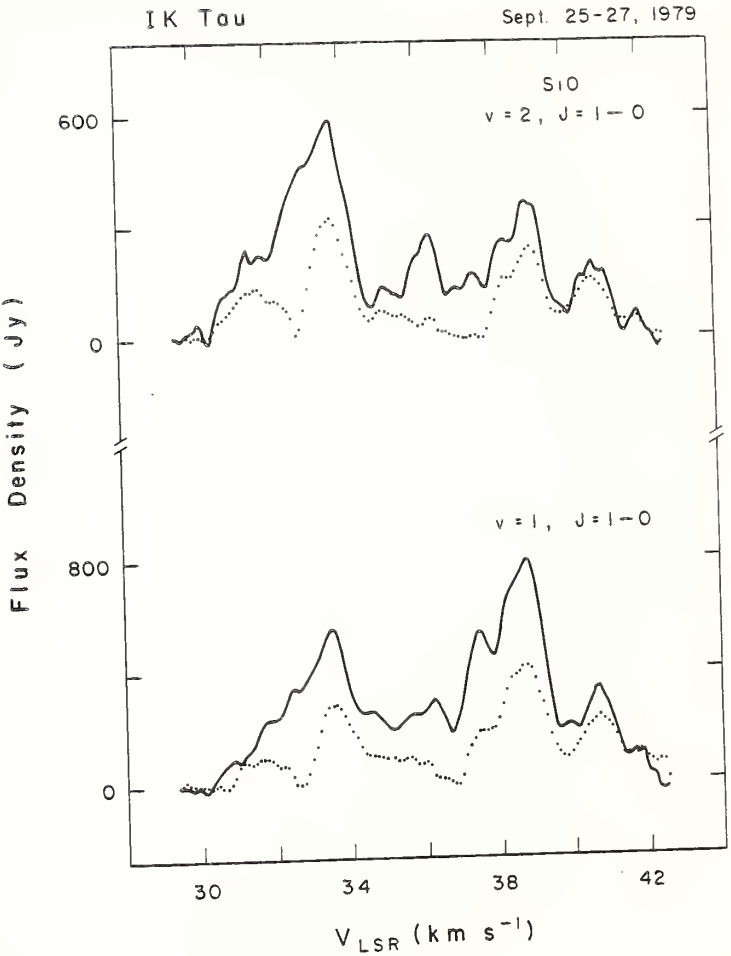
IK Tau
Sept. 25-27, 1979
SiO
v = 2, J = 1 — 0
600
0
v = 1, J = 1 — 0
800
0
Flux Density (Jy)
30
34
38
42
V LSR (km s⁻¹)

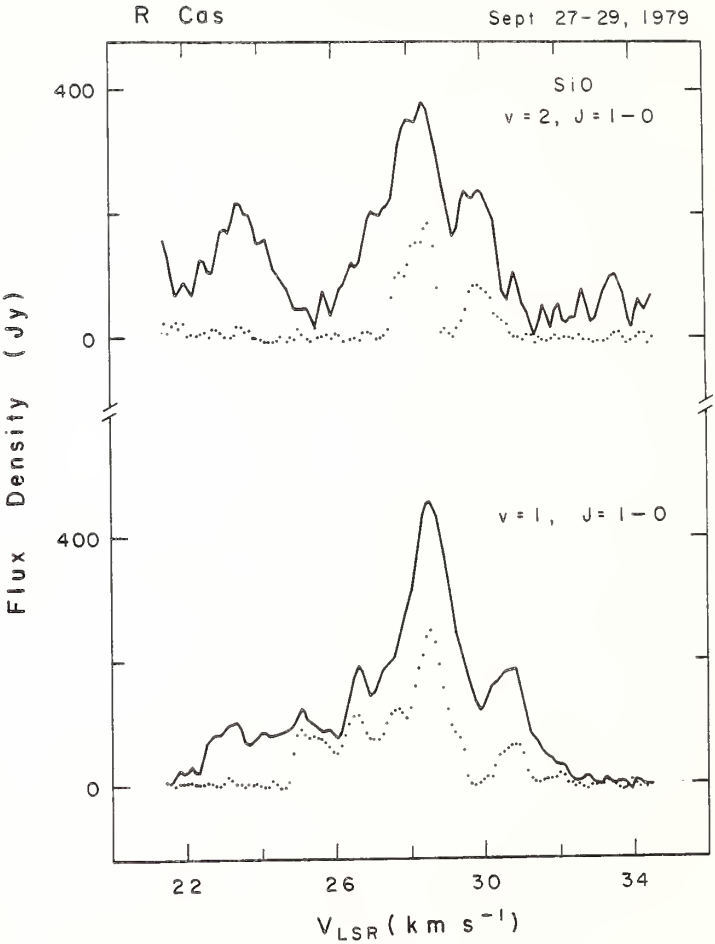
R Cas
Sept 27-29, 1979
SiO
v = 2, J = 1 − 0
v = 1, J = 1 − 0
400
0
400
0
Flux Density (Jy)
22
26
30
34
V_{LSR} (km s^{-1})

spectra were produced by averaging autocorrelation data from FCRAO. Although weak fringes were obtained on VY CMa, the observations were made at relatively low elevations under poor weather conditions; numerous baseline problems at both observatories rendered useless the autocorrelation data and thus prevented calibration of the cross power amplitudes. An attempt was made, however, to phase map the data and the results will be discussed below.

First, the visibility data will be described for individual sources, then the maps will be presented:

VX SGR. As before, the cross power spectra for VX Sgr can be decomposed into at least 15-20 features. Visibilities are in the range 0.3-0.6 in both transitions, corresponding to apparent linear diameters of ~1.5-3.0 x 10^{14} cm. In contrast to the results of the previous experiment, several features near the stellar velocity (6 km s^{-1}) show up with high visibilities (e.g., V ~ 0.6-1.0); their detection in the present experiment may be due to the increased sensitivity, or could perhaps be a time variability effect (ϕ_V = 0.35 as compared with 0.89 during Exp. II).

IK TAU. The cross power spectra for IK Tau consist of 15-20 blended features with half-power widths of 0.4-1.0 km s^{-1}. Visibilities vary widely across the spectrum, with some (marginal) evidence for higher visibilities at the more extreme velocities. The average visibility of ~0.5 corresponds to an apparent maser size of ~10 milliarcsec,

or a linear size of ~4 x 10^{13} cm at the distance of IK Tau. The v=1, J=1-0 and v=2, J=1-0 transitions appear to have both very similar velocity structure and similar maser sizes. The typical peak brightness temperatures for IK Tau are ~5 x 10^{9} K in both transitions.

R CAS. The emission in R Cas is mostly redshifted from the stellar velocity (24.7 km s^{-1}). The weak features at V* and on the blueshifted side are either completely resolved out or have very low visibilities ($V \leq 0.15$), while the redshifted features have visibilities which are in the range 0.4-0.6. All features in the v=1, J=1-0 and v=2, J=1-0 lines are at least partially resolved; apparent spot sizes are in the range 8-17 milliarcsec (2.8-5.9 x 10^{13} cm).

W HYA. As for R Cas, the emission from W Hya at the time of this experiment was predominantly redshifted from the stellar velocity (40 km s^{-1}) and visibilities of partially resolved features were low ($V \sim 0.1$-0.5). Corresponding spot sizes are 2-4 x 10^{13} cm. No evidence for any systematic variation of spot size with velocity is apparent in this source. The limited amount of data and the spectral blending of features confuses any more detailed interpretation of the visibility data.

Phase maps. The relative positions of different spectral components can be determined either by analysis of relative fringe phase data or by analysis of relative fringe rate (the time derivative of fringe phase). Fringe rate mapping is inherently much less sensitive than phase

mapping, but must be used when the distribution of maser components is spread over an area which is sufficiently large compared to the interferometer fringe spacing that integral 2π ambiguities in the phase cannot be resolved. Because the stellar sizes of the sources observed in the present study are on the order of the fringe spacing ($\theta_f \sim 20$ milliarcsec) and because it is likely from excitation considerations that SiO masers occur within a few stellar radii of the stars, SiO masers at 43 GHz are amenable to phase mapping techniques for data obtained on the FCRAO-Haystack baseline ($D/\lambda = 10^7$).

The relative phase, $\Delta\phi$, of the emission from two maser features separated by right ascension offset, $\Delta\alpha$, and declination offset, $\Delta\delta$, is given by

$$\Delta\phi(t) = 2\pi \left\{ u\ \Delta\alpha \cos\delta + v\ \Delta\delta \right\} \text{ radians} \qquad \text{(IV-2)}$$

where δ is the declination of the source and u and v are the projected baseline components in wavelengths:

$$u = \frac{1}{\lambda} \left(X^2 + Y^2\right)^{1/2} \sin(\text{IHA})$$

$$v = -\frac{1}{\lambda} \left(X^2 + Y^2\right)^{1/2} \sin\delta \cos(\text{IHA}) + \frac{1}{\lambda} Z \cos\delta \ .$$

The quantities X, Y, and Z are the components of the baseline (in meters) along axes in the directions of 0° longitude, 90° west longitude, and the earth's instantaneous pole, respectively. The interferometer hour angle (IHA) is given by

$$IHA = UTC + GASTM - \alpha - \tan^{-1}(Y/X),$$

where GASTM is the Greenwich apparent sidereal time at 0^h UTC. The mapping technique consists of adjusting the position offsets ($\Delta\alpha$, $\Delta\delta$) to minimize the sum of the squares of the differences between a time series of measurements of $\Delta\phi$ and the model phases predicted by Eq. IV-2.

Figure 13 shows plots of phase relative to the reference feature versus interferometer hour angle for three spatially separated maser features in the v=1, J=1-0 line from VX Sgr. These plots demonstrate the quality of the phase data (each point represents 12 minutes of data) and of the least squares fits (solid lines). It is clear that the features are clustered within a sufficiently small region and gaps in the data sampling are sufficiently small that phase connection and integral turn ambiguities are not a problem.

The resulting map of the distribution of the v=1, J=1-0 maser features toward VX Sgr is shown in Figure 14; the position offsets (relative to the reference feature at 3 km s^{-1}) are listed in Table 11. The spatial distribution of the v=2, J=1-0 masers near VX Sgr is shown in Figure 15. In both transitions, the features are spread over an area approximately 70 milliarcsec (~1.5 x 10^{15} cm) in diameter. The cluster size is thus about an order of magnitude larger than the apparent spot sizes of the individual features. The size of the stellar photosphere (at the appropriate light cycle phase) is shown in the inset to Figs. 14 and 15, based on effective temperature and total flux measurements of

Figure 13. Relative phase versus interferometer hour angle (IHA) for three maser components in the v=1, J=1-0 SiO line from VX Sgr. The data (circles) were obtained on Sept. 24, 1979 during a VLBI experiment between FCRAO and Haystack. The position offsets of these (and other) features were determined from a least squares fit (shown by the solid line) of Eq. IV-2 to the data; the offsets are given in Table 11 and plotted in Fig. 14.

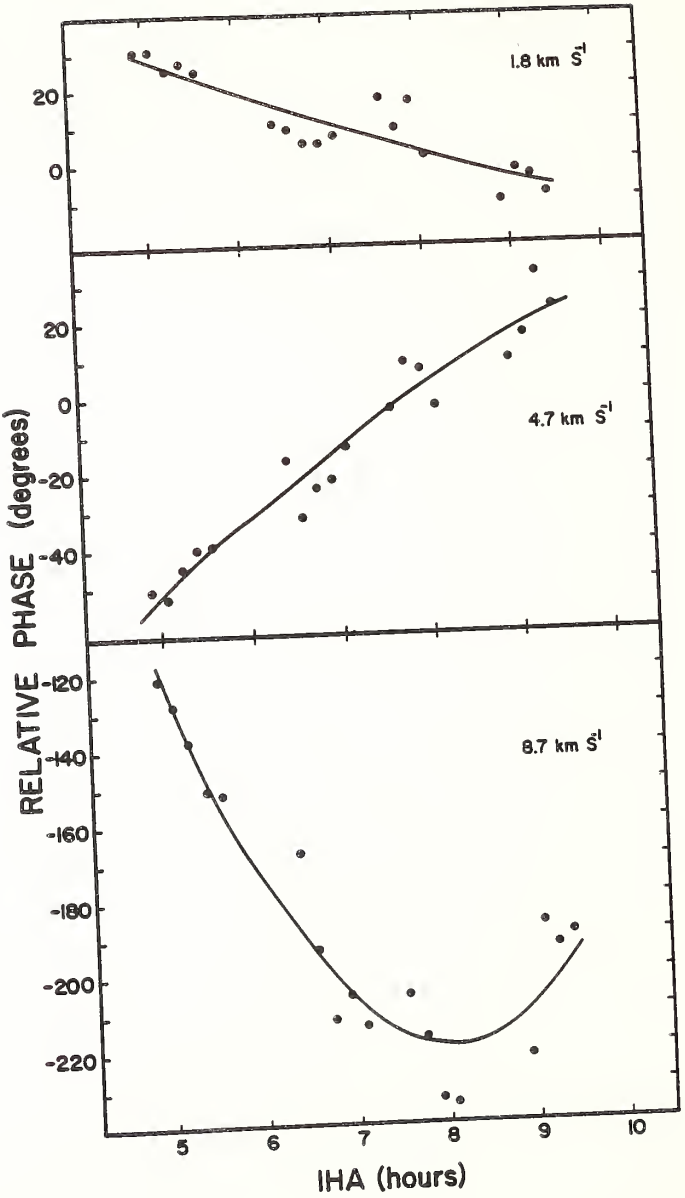
1.8 km S⁻¹
4.7 km S⁻¹
8.7 km S⁻¹
RELATIVE PHASE (degrees)
IHA (hours)
20
0
-20
-40
-120
-140
-160
-180
-200
-220
5
6
7
8
9
10

TABLE 11

RELATIVE POSITIONS OF MASER FEATURES TOWARD VX SGR

v = 1, J = 1 - 0			v = 2, J = 1 - 0		
Radial Velocity (km s^{-1})	θ_x(a) (milliarcsec)	θ_y(a) (milliarcsec)	Radial Velocity (km s^{-1})	θ_x(a) (milliarcsec)	θ_y(a) (milliarcsec)
10.5	-20.4±1.0	17.8±4.2	9.4	15.4±0.6	-25.7±3.5
10.2	9.5±0.5	-9.1±2.6	9.2	16.8±0.5	-24.7±3.1
9.7	-14.9±0.5	-1.1±2.3	8.9	17.2±0.4	-25.0±2.1
8.7	16.5±0.3	-24.3±1.2	8.6	19.3±0.6	-27.8±3.2
8.0	22.4±1.5	21.4±6.5	7.8	26.0±1.2	-1.5±7.0
6.9	18.5±0.4	-12.2±1.7	5.0	-26.2±0.6	30.0±3.7
6.0	-8.0±0.9	38.2±4.1	4.5	-2.2±0.3	10.2±1.9
5.1	0.4±0.6	15.7±2.7	3.8	-0.6±0.2	3.4±1.0
4.7	-0.9±0.2	11.2±0.7	3.0	0.0±0.0	0.0±0.0
4.3	-1.3±0.2	9.2±0.9	2.5	-0.2±0.3	-1.4±1.6
3.6	-0.3±0.2	3.9±1.0	2.1	0.2±0.2	-3.7±1.0
3.0	0.0±0.0	0.0±0.0	1.9	-0.6±0.3	-0.4±1.7
2.3	0.6±0.2	-3.8±0.7	1.6	-0.4±0.2	-2.8±1.3
1.8	0.3±0.2	-5.0±0.7	1.0	0.1±0.5	-6.5±3.1
1.4	0.0±0.2	-5.5±0.9	0.6	-3.2±0.7	-0.9±3.8
0.8	2.7±0.7	-15.1±3.0	0.1	-1.1±0.6	-10.8±3.6
0.1	26.2±1.0	-31.4±4.2			

(a) Errors are 1σ formal errors from the fit.

Figure 14. Map of SiO features in the v=1, J=1-0 line from VX Sgr. The RA and Dec position offsets were determined from relative fringe phase data obtained on Sept. 24, 1979. The number next to each maser spot is the observed radial velocity in km s^{-1}. The reference feature is at 3.0 km s^{-1}. Features which are redshifted from the stellar velocity (6 km s^{-1}) are plotted as open circles; blueshifted features are shown as filled circles. Error bars are 2σ formal errors from the model fit. The size of the star is shown in the inset and is based on effective temperature and total flux measurements by Lockwood and Wing (1982), with an assumed distance of 1500 pc. The dashed circle indicates the position of the expanding shell discussed in the text.

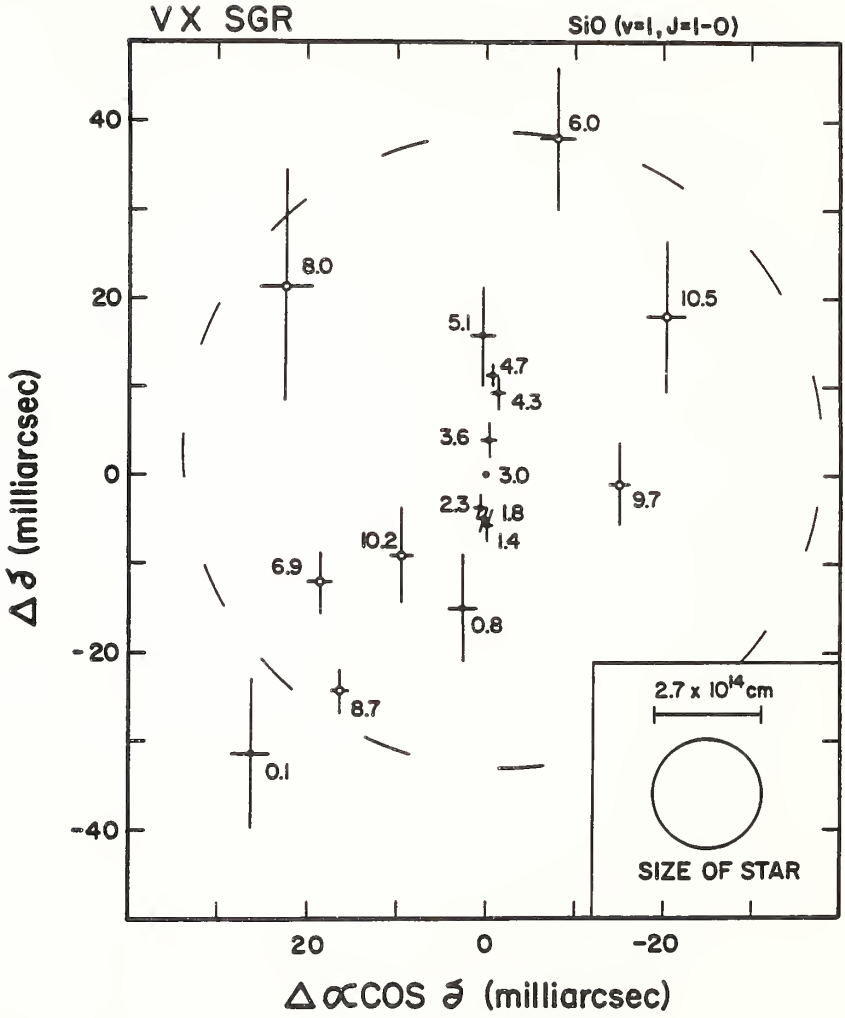
VX SGR
SiO (v=1, J=1-0)
6.0
8.0
10.5
5.1
4.7
4.3
3.6
3.0
2.3
1.8
1.4
9.7
10.2
6.9
0.8
8.7
0.1
2.7 x 10^14 cm
SIZE OF STAR
40
20
0
-20
-40
20
0
-20
Δδ (milliarcsec)
ΔαCOS δ (milliarcsec)

Figure 15. Map of SiO features in the v=2, J=1-0 line from VX Sgr. Same as Fig. 15, except data were obtained on Sept. 26, 1979. Error bars for the features near the reference feature (3 km s^{-1}) are comparable to the size of the circles.

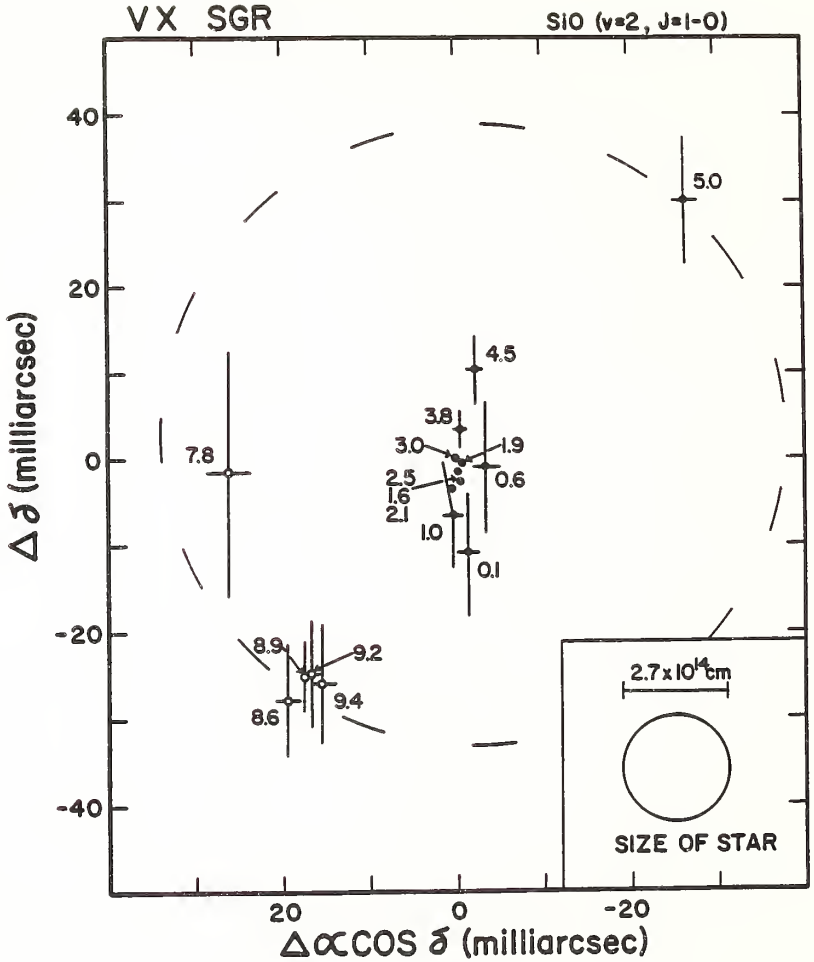
VX SGR
SiO (v=2, J=1-0)
40
20
0
-20
-40
Δδ (milliarcsec)
5.0
4.5
3.8
3.0
1.9
2.5
0.6
1.6
2.1
1.0
0.1
7.8
8.9
9.2
9.4
8.6
2.7x10^14cm
SIZE OF STAR
20
0
-20
ΔαCOS δ (milliarcsec)

Lockwood and Wing (1982). Although the precise location of the star on the map is unknown, it appears that the SiO features mapped in this experiment are probably located within 5-6 R_* of the stellar surface.

Because a somewhat longer interval of data was obtained in the v=1, J=1-0 transition toward VX Sgr, accurate positions could be determined for more features than in v=2, J=1-0 and more features appear on the v=1 map. Nonetheless, comparison of positions of features which were mapped in both transitions shows a high degree of similarity in the two maps. In particular, the blueshifted features (filled circles) are clustered at the center on both maps, while the redshifted features (open circles) appear surrounding them. On both maps, the blueshifted features show an elongated distribution with a north-south progression from higher to lower velocities. Further correspondence between the two maps is seen in the position of features in the velocity range 8.6-9.4 km s^{-1}.

The spatial distribution of the v=1, J=1-0 masers appears to be consistent, at least in a qualitative way, with their location in an expanding circumstellar shell. The possible location of such a shell is suggested on the maps in Figs. 14 and 15 by a large dashed circle. In this model, the blueshifted features would be located directly in front of the star and their velocities would result from the outflow of material (toward the observer). Extreme redshifted velocities from the backside of the shell would not be observed at map center due to occultation by the stellar disk. A few features at intermediate red-

shifted velocities are seen in a region surrounding map center, corresponding to projected velocities of backside radial mass outflow. The feature at the stellar velocity (6 km s^{-1}) may mark the edge of the expanding SiO maser shell, where amplification is in the direction perpendicular to mass outflow. The radius of the SiO shell is then ~8 x 10^{14} cm. This model is roughly consistent with both the v=1, J=1-0 and v=2, J=1-0 maps. The physical interpretation of the velocity gradient in the blueshifted features is not clear; systematic effects in the mapping procedure cannot be definitely ruled out.

Relative positions of maser features toward R Cas were also determined by analysis of relative phase. A map of the distribution of v=1, J=1-0 masers is shown in Figure 16 and offsets are listed in Table 12. The masers occur out to distances of at least four stellar radii (eg., $R_{SiO} \sim 1.5 \times 10^{14}$ cm) from the star, whose size is shown in the inset (cf. Cahn and Elitzur 1979). The distribution is elongated in the NW-SE direction; this direction does <u>not</u> coincide with the axis of maximum positional uncertainty due to the limited u-v coverage of the data. No systematic velocity gradient is found along the axis of elongation. All of the mapped features are redshifted from the stellar velocity (24.7 km s^{-1}).

Limited maps were also attempted on the Orion and VY CMa data in the v=1, J=1-0 transition, although the signal-to-noise ratio was generally lower than for the above sources due to the use of frequency switching to observe the full velocity range of the emission (and also

Figure 16. Map of SiO features in the v=1, J=1-0 line from R Cas. The RA and Dec position offsets were determined from relative fringe phase data obtained on Sept. 29-30, 1979. The number next to each maser spot is the observed radial velocity in km s^{-1}. The reference feature is at 28.5 km s^{-1}. Error bars are 2σ formal errors from the model fit. The size of the star (Cahn and Elitzur 1979) is shown in the inset; the linear scale assumes a distance of 230 pc (Lepine and Paes de Barros 1977). All of the features on the map are redshifted from the stellar velocity (24.7 km s^{-1}).

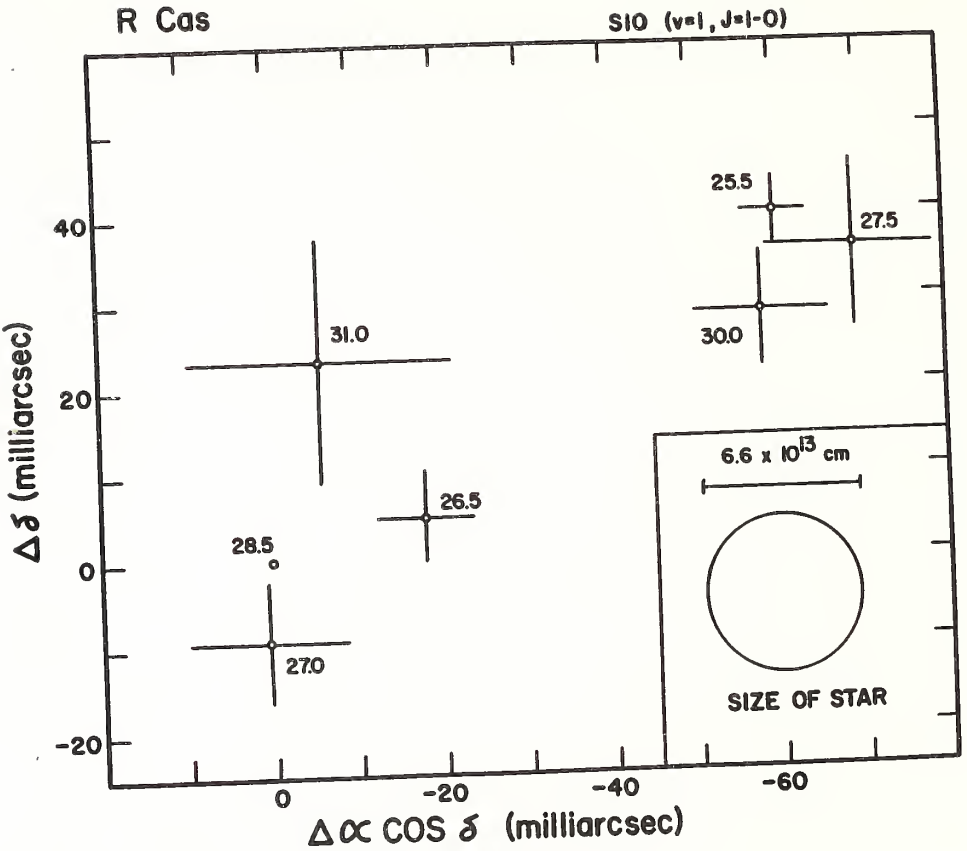
R Cas
SiO (v=1, J=1-0)
25.5
27.5
30.0
31.0
26.5
28.5
27.0
6.6 x 10^13 cm
SIZE OF STAR
40
20
0
-20
0
-20
-40
-60
Δδ (milliarcsec)
Δα COS δ (milliarcsec)

TABLE 12

RELATIVE POSITIONS OF MASER FEATURES TOWARD R CAS

v = 1, J = 1 - 0		
Radial Velocity ($km\ s^{-1}$)	Θ_x(a) (milliarcsec)	Θ_y(a) (milliarcsec)
31.0	-6.0±8.0	23.5±7.0
30.0	-58.0±4.0	28.0±3.5
28.5	0.0±0.0	0.0±0.0
27.5	-69.0±6.0	36.0±5.0
27.0	1.0±4.5	-9.0±3.6
26.5	-18.0±3.0	5.0±2.5
25.5	-60.0±2.0	39.0±2.0

(a) Errors are 1σ formal errors from the fit.

due to adverse weather). In Orion, the two main groups of features at $\sim$-6 km s^{-1} and +19 km s^{-1} (see Fig. 5m) appear to be spatially offset by $\sim 10^{15}$ cm. This is demonstrated by the data shown in Figure 17, where the variation with interferometer hour angle of the phase for a strong channel within the 19 km s^{-1} feature is shown relative to the phase of the reference channel at -5.3 km s^{-1}. Although the relative phase undergoes several turns in the observed period, the data sampling is sufficiently close that the phase connections from one scan to the next are well-determined. The position offsets derived from the fitted curve are:

$$\begin{aligned} \Delta\alpha \cos\delta &= -51 \pm 3 \text{ milliarcsec} \\ \Delta\delta &= 128 \pm 17 \text{ milliarcsec} . \end{aligned}$$

The individual features within the two main groups appear to be clustered within 10-20 mas, or $\sim 10^{14}$ cm at a distance of 500 pc.

In VY CMa, only the 2-3 strongest features produced detectable fringes. The feature at 19-20 km s^{-1} (cf. Fig. 5ℓ) is offset from the reference feature at 12 km s^{-1} by:

$$\begin{aligned} \Delta\alpha \cos\delta &= -40 \pm 12 \text{ milliarcsec} \\ \Delta\delta &= -26 \pm 12 \text{ milliarcsec} . \end{aligned}$$

This separation corresponds to $\sim 10^{15}$ cm at a distance of 1500 pc.

§4. Discussion and Conclusions

The low visibilities generally observed toward the SiO maser sources studied by VLBI (Moran et al. 1979; this work) imply that a signi-

Figure 17. Relative phase of features near -5 and +19 km s^{-1} versus interferometer hour angle for the Orion SiO (v=1, J=1-0) line. The solid line is a least squares fit of Eq. IV-2 to the data points.

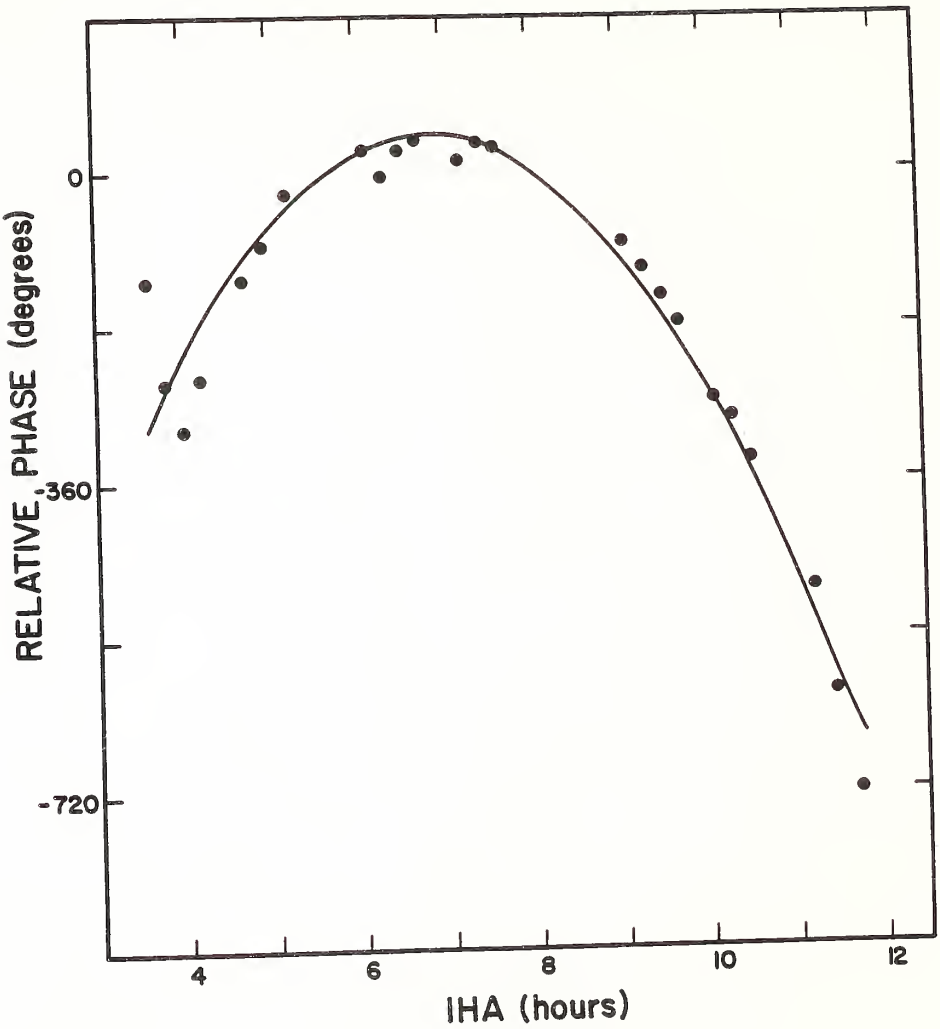
RELATIVE PHASE (degrees)
0
-360
-720
4
6
8
10
12
IHA (hours)

ficant fraction of the flux originates either from extended halo components (i.e., large features) surrounding the hot spots detected by the interferometer or from an ensemble of many weak maser components, small in size, but spread over an area larger than the fringe spacing. Thus, roughly half of the observed total-power flux is not accounted for on the maps presented here. The apparent sizes of the smallest features observed toward Mira variables are in the range 2-6 x 10^{13} cm (FWHM), while for the supergiant VX Sgr the sizes are 2-4 x 10^{14} cm, assuming a Gaussian brightness model. The spot sizes of the smallest features toward Orion are ~8 x 10^{13} cm. These maser sizes imply peak brightness temperatures of ~5 x 10^{9} K for W Hya, IK Tau, R Cas, and Orion and ~2 x 10^{10} K for VX Sgr. During the July, 1978 VLBI experiment (Exp. I), a brightness temperature of 2 x 10^{10} K was observed for R Cas (Moran et al. 1979).

An estimate of the state of saturation of the J=1-0 SiO masers follows from the observed flux densities and apparent angular sizes. A maser is said to be "saturated" when the rate at which population is transferred across the maser transition (the "stimulated emission rate") exceeds the rate at which population of a maser level is transferred to other energy levels of the molecule (the "decay rate"). The stimulated emission rate, W, is given by (Kwan and Scoville 1974):

$$W = \frac{B\ I\ \Omega}{4\ \pi} \quad , \qquad \text{(IV-3)}$$

where B is the Einstein coefficient (2.54 x 10^{9} cm^{2} $ergs^{-1}$ s^{-1}), Ω is

the solid angle into which the maser radiation is beamed, and I, the maser intensity at the surface of the cloud, is related to the distance, d, and maser radius, r, by

$$I = \frac{S_\nu \, d^2}{\Omega \, r^2} \, .$$

Evaluating Eq. IV-3 using the maser sizes and fluxes measured here ($r \sim 2\text{-}4 \times 10^{13}$ cm, $S_\nu \sim 500\text{-}1000$ Jy) gives W equal to a few x 10^2 to a few x 10^3 sec^{-1}. The decay rate is estimated by Kwan and Scoville (1974) to be ~5 sec^{-1}, the rate of spontaneous decay to the ground vibrational state. Hence, the masers are probably saturated.

The spatial maps obtained for VX Sgr and R Cas, and the more limited positional data obtained for Orion and VY CMa, imply that the masers are clustered within ~4-6 stellar radii from the centers of the stars. (The dimensions of the maser clusters toward VX Sgr and R Cas deduced from the data of Experiment III are somewhat larger than those reported by Moran et al. (1979) based on more limited data; the differences appear to be due to the detection of a larger number of features with the higher sensitivity of the later experiment). The fact that the observed distributions are significantly larger than the stellar disks is inconsistent with the model by Elitzur (1980a) locating the masers (in particular, the strong, narrow spikes) in convective cells in the stellar photosphere. The maser spots mapped in this study must be located farther from the stellar surface than is implied by the convective cell model. Furthermore, the apparent sizes of these masers

are considerably larger than the expected dimensions of convective cells (Elitzur 1980a; Schwartzschild 1975) and, in fact, are comparable with the diameters of the stellar disks themselves (6-7 x 10^{13} cm for R Cas, IK Tau, and W Hya). The true physical sizes of the masers are probably even larger (Goldreich and Keeley 1972).

Since the extent of the masering region is larger than the size of the star, it is likely that the masers amplify their own spontaneous emission rather than stellar photons. If the fractional population inversion, $(N_2 - N_1)/N_2$, is ~0.12 for the J=1-0 transition (cf. Kwan and Scoville 1974), the spontaneous emission provides a source of photons at an effective temperature of 16 K. A maser gain of $\sim e^{21}$ would then be required to produce the observed brightness temperatures of 2 x 10^{10} K. The thermal Doppler width ($\Delta v_D = (8 \ln 2\ kT/m)^{1/2}$) expected in a region with $T_k = 10^3$ K is ~1 km s^{-1}; the line width of an unsaturated maser with 21 gain lengths would be reduced to ~0.22 km s^{-1} ($\Delta v = \Delta v_D/(21)^{1/2}$). Thus, the observed line widths ($\Delta v \sim 0.3$-1.0 km s^{-1}) also imply the masers are at least partially saturated.

Comparison of the VLBI results for the v=1, J=1-0 and v=2, J=1-0 lines indicates that these masers have similar properties. For the five sources observed in both transitions, the visibilities, and hence apparent spot sizes and brightness temperatures, are comparable in the two lines. Since the velocity structure present in the line profiles is also very similar in the two transitions (see also Chapter II), it appears that the masers must originate from the same regions in the

circumstellar envelope. This conclusion is borne out, at least in a general way, by the spatial maps produced in both v=1, J=1-0 and v=2, J=1-0 for the supergiant VX Sgr. The maps show similar position offsets for velocity features which were mapped in both transitions, and both distributions are consistent with location of the masers in an expanding shell of radius 8 x 10^{14} cm.

The size and spatial extent of SiO masers may be compared with properties of H_2O masers in circumstellar envelopes. Apparent sizes of SiO masers are generally larger than sizes of H_2O masers observed toward late-type stars (Spencer et al. 1979). Toward W Hya, for example, $\Theta_{app}(SiO) = 4\text{-}8 \times \Theta_{app}(H_2O)$. The reverse is true in Orion, however; the apparent sizes of the H_2O "shell" features are about four times larger than the SiO maser features in Orion (Genzel et al. 1979). Although only the strongest H_2O features in the spectra of several Mira and semi-regular variables were mapped by Spencer et al., the sizes of the H_2O clusters toward these stars appear to be comparable to or slightly larger than the SiO cluster sizes reported here for the Mira variable R Cas. The VLBI results are thus consistent with the idea that the SiO masers, which have higher excitation requirements than H_2O, occur in regions which are somewhat closer than the H_2O maser regions to the central energy sources which pump them. This conclusion appears to be true for the supergiants which have been measured as well. For VX Sgr, the SiO shell has a radius of ~8 x 10^{14} cm, while the H_2O maser shell has a radius of 2 x 10^{15} cm (Moran et al. 1980; quoted by Elitzur

1980b). In VY CMa, the H_2O masers are spread over a region 5×10^{15} cm in diameter (Rosen et al. 1978), while the two strongest SiO features are separated by 1×10^{15} cm. Because the H_2O maser flux densities toward stars are about the same as SiO flux densities, the smaller H_2O sizes imply H_2O brightness temperatures which are higher by at least an order of magnitude than the SiO brightness temperatures.

C H A P T E R I V.

DISCUSSION AND COMPARISON WITH MASER MODELS

This study has sought to define the major observational characteristics of SiO masers which must be taken into account by any theoretical attempt to model the masers and the physical environment in which they occur. The major findings of this thesis are summarized below. Then the maser models which have been published to date are briefly described and the implications of the observational results for these models are discussed. Finally, recent progress in understanding the kinematics and energetics of pulsating stellar atmospheres through time monitoring infrared spectroscopy is used as a context in which to view the SiO maser phenomenon.

§1. Summary of Results

1) Time monitoring observations in four microwave maser transitions of SiO toward late type variable stars show that many sources exhibit variations of integrated flux which correlate with the stellar light and pulsation cycle. Correlated variability was observed in the following sources and transitions (transitions are indicated as follows: A (v=1, J=1-0); B (v=2, J=1-0); C (v=3, J=1-0); D (v=1, J=2-1)): R Leo (C), Mira (A, B, D), U Ori (A, B, D), W Hya (A, B, C), R Cas (A), IK Tau (A, B, D), TX Cam (A, B, C), and VX Sgr (A, C).

2) The maxima in the SiO light curves generally lag the optical maxima by an amount (0.1-0.2 period) which is consistent with the phase lag of the stellar variations in the near-infrared.

3) Non-periodic and erratic variations of integrated SiO flux are also observed. The secular trends have timescales on the order of a few years (e.g., v=1, J=2-1 in VX Sgr, Orion, W Hya), while shorter timescale erratic variations are seen in the Orion and VY CMa J=1-0 (v=1 and v=2) lines and in v=1, J=2-1 from R Cas, TX Cam, χ Cyg, and U Her. The SiO J=1-0 transitions in R Leo and in R Cas show a decline in flux over a 1-2 year period following instances of unusually bright optical maxima in these sources.

4) Over the 2½ year observing period, the integrated flux in the various transitions in thirteen sources varied by factors ranging from ~2-30. The small amplitude of these changes suggests saturated masers. The J=2-1 flux generally exhibits a smaller range of variability than the J=1-0 transitions.

5) The differences between sources in total maser output are much larger than the variations within a given source. The maximum SiO photon luminosities of these thirteen sources range over more than three orders of magnitude, from $\sim 5 \times 10^{42}$ to $\sim 1 \times 10^{46}$ photons s^{-1} in each of the three strongest transitions (J=1-0, v=1 and v=2; J=2-1, v=1).

6) The maser output is larger for stars with longer period (and, therefore, higher stellar luminosity (Cahn 1981)).

7) On the average, the maser photon luminosities of the J=1-0 transitions in the first three excited vibrational states are in the ratio:

$$L(v=1) : L(v=2) : L(v=3) = 1 : 0.67 : 0.04 \quad .$$

The photon luminosities in the two lowest rotational transitions of the v=1 state are in the ratio:

$$L(J=1-0) : L(J=2-1) = 1 : 1.20 \quad .$$

None of the line ratios show any systematic variation with stellar optical phase.

8) SiO maser emission from red giant variable stars is confined within the range -8 to +14 km s^{-1} relative to the stellar velocity. The average total velocity extent of the emission is 10 km s^{-1}, with no significant difference in width between the J=2-1 (v=1) and J=1-0 (v=1 and v=2) lines. For the supergiants VX Sgr and VY CMa, the emission occurs in the range -20 to +30 km s^{-1} relative to the stellar velocity.

9) On the average, the emission profiles in the v=1, J=1-0 and v=2, J=1-0 transitions are systematically skewed to the red for nine out of ten sources for which reliable determination of V_* is available; the average velocity shift of the emission centroid is 2.7 km s^{-1}. At most epochs, from 65-100% of the flux in the J=1-0 (v=1 and v=2) transitions originates from redshifted gas. Over the same period, a similar predominance of redshifted emission is <u>not</u> present in the v=1, J=2-1 line.

The profiles in the v=3, J=1-0 transition range from a single narrow spike near V_* to a total velocity width of over 25 km s^{-1} in VY CMa.

10) Neither the velocity extents of redshifted and blueshifted emission, nor the fraction of the total flux which is redshifted from V_* were found to correlate with stellar optical phase.

11) At a given epoch, the spectra of the J=1-0 rotational transitions in different vibrational states show a marked resemblance to each other in velocity structure; incidence of corresponding velocity components in the v=1, J=1-0 and v=2, J=1-0 transitions is at least 70%. The v=1, J=2-1 line shows velocity structure which is dissimilar both to the J=1-0 lines and to the v=2, J=2-1 line.

12) No evidence was found for any phase dependent variations in either the velocities of individual features or in other velocity structure characteristics of the lines. Such characteristics include the central velocity of the pedestal, the total velocity extent of the emission, and the presence or absence of stellar velocity features, pedestal emission, and features at extreme redshifted or blueshifted velocities. No evidence was found for any cycle to cycle repeatability of profile shape.

13) In spite of large changes in flux, individual features often have lifetimes as long as several hundred days. On the other hand, the profile may change its appearance completely within 1-2 months.

14) The apparent sizes of the smallest features in the J=1-0 lines toward Mira variables are in the range 2-6 x 10^{13} cm (FWHM). For the supergiant VX Sgr, the sizes are 2-4 x 10^{14} cm. Toward Orion, the spot sizes are ~8 x 10^{13} cm. The maser sizes and flux densities imply the v=1, J=1-0 and v=2, J=1-0 masers are saturated. The peak brightness temperatures in both transitions are ~5 x 10^{9} K for W Hya, IK Tau, R Cas, and Orion and ~2 x 10^{10} K for VX Sgr.

15) Toward R Cas, the v=1, J=1-0 masers occur out to distances of at least 4 R_* (1.5 x 10^{14} cm). The spatial distributions of the v=1, J=1-0 and v=2, J=1-0 masers toward VX Sgr are roughly similar to each other and are consistent with location of the masers in an expanding circumstellar shell of radius 6 R_* (~8 x 10^{14} cm).

§2. Models for SiO Maser Pumping

The basic requirement which enables a maser to operate is a population inversion between the levels involved in the maser transition. In addition to the presence of an energy source not in thermal equilibrium with the masing gas, there must be an adequate abundance of the maser molecules and sufficient velocity coherence along the maser column such that substantial maser gain is achieved. For SiO, since masers are observed from vibrational levels which are as high as 5251 K above the ground state, a means of populating such high energy levels is also required. It is this requirement which implies proximity to the star for SiO masers.

A mechanism utilizing radiative trapping for inversion of the rotational levels of an excited vibrational state was proposed by Kwan and Scoville (1974). They showed that population inversions of the low J rotational states within vibrational state v are possible if the $v \rightarrow v-1$ radiative decays are optically thick and if transfer of population into the v level is by some other route than by optically thick radiative excitation from the v-1 level. The mechanism they discuss involves indirect radiative excitation of the v level by optically thin transitions from higher v states. Inversions occur because the de-excitation rates decrease as J increases when the radiative decays are thick (Kwan and Scoville 1974). Since equal numbers of photons escape in each thick line, the selection rule $\Delta J=\pm 1$ implies that for each rotational level J, the decay rate per magnetic sublevel is proportional to $2/(2J+1)$. This model can, in principle, produce population inversions in the various observed vibrational states, although not in the same volume of gas. Population inversions in the v=2 state, for example, require optically thick $v=2 \rightarrow 1$ transitions, while v=1 masers (in the KS model) require these transitions into v=1 to be thin. Since the fraction of the molecules in the v=2 state is small compared to the population in the v=1 state for temperatures of order 1000-2000 K, the masers in v=2 would be expected to be weaker than v=1 masers if the rotational population inversions are of comparable magnitude. In fact, however, the photon emission rates in the v=1, J=1-0 and v=2, J=1-0 masers in a given source are about equal.

The observed high degree of correspondence in the velocity structure and spatial distribution of the v=1, J=1-0 and v=2, J=1-0 masers suggests that these masers operate in the same clumps of gas, a fact which is incompatible with the Kwan and Scoville pumping mechanism. Furthermore, inversions in J=3-2 and higher rotational states are not predicted by the model, yet strong masers in states as high as J=5-4 have recently been detected (Clemens and Lane 1982).

Deguchi and Iguchi (1976) proposed a radiative pumping model which produces masers in the v=1 and v=2 states and in rotational transitions higher than J=2-1 by utilizing anisotropic escape probabilities in an expanding gas having a large velocity gradient. Using the formalism of Castor (1970), the opacity of the gas in a direction at angle Θ from the radial direction is given by

$$\tau(\cos\,\Theta) = \frac{\tau_o}{1 + (\varepsilon - 1)\,\cos^2\Theta}$$

where τ_o, the opacity for $\Theta = \pi/2$, depends on the population inversion and the velocity law. When the logarithmic velocity gradient (ε = d ln V/d ln R) of the gas is large, the opacity in the radial direction is smaller than the opacity in the tangential direction. The result is that the gas in the maser region can be optically thin to absorption of 8μ stellar photons (v-1 $\rightarrow$ v), while the angle averaged opacity applicable to the v $\rightarrow$ v-1 radiative decays remains larger than unity (as required to invert the rotational levels in the v state). Thus, the

populations of rotational levels of several vibrational states can be inverted at nearly the same radius (cf. Figs. 2 and 3 of Deguchi and Iguchi (1976)). The model predicts maximum maser gains along lines of sight which are tangential to the star for regions where the acceleration of the gas is large (e.g., ϵ = 3-5). Thus, masers would be expected to occur at or very close to the stellar velocity, with no preference for redshifted or blueshifted velocities.

The anisotropic escape model cannot explain masers which occur at velocities widely separated from V_*, nor the asymmetry of the line profiles. A further difficulty with this mechanism is that if the opacity for emission in the v=1→0 line is very large (as is likely (Kwan 1982, private communication)), the radial opacity for absorption will also be substantial even for strong velocity gradients. The spatial distributions observed for the masers toward VX Sgr and R Cas are not consistent with the prediction of tangential masers.

A pumping mechanism for SiO masers based on collisions rather than radiation has been developed by Elitzur (1980a). In order that collisional rates dominate radiative rates, the masers must be located in the stellar atmosphere rather than in the inner regions of the circumstellar shell. While the excitation of low J levels of excited vibrational states is dominated by collisions according to this model, the population inversions are still maintained by optically thick vibrational decays as in the Kwan and Scoville mechanism. Since the atmosphere is known to be partaking in large amplitude oscillations the effects of which are not

seen in the velocities of SiO maser features, Elitzur proposes that the masers are located within large convective cells in the photosphere. Velocity coherence is expected to be greatest for masers tangential to the stellar surface so that the masers would be expected at the stellar velocity, with a velocity range consistent with expected convective velocities (~5 km s^{-1}). Although parameters and physical conditions within convective cells are not well-known, lifetimes of cells are estimated to be 100-200 days (Schwartzschild 1975; Elitzur 1980a), so that longer lifetimes for individual maser features would not be expected.

As described in Chapter III, both the apparent maser sizes and the spatial distribution of masers toward VX Sgr and R Cas are inconsistent with Elitzur's model. Although not all of the maser flux is detected by the interferometer, it is evident that a large fraction of the flux originates from maser features spread over an area several times larger than the stellar disks. The observed time variability behavior of the masers strongly suggests radiative pumping. The stability of some maser profiles (e.g., v=1, J=1-0 in VY CMa) over periods of at least 20 months is also difficult to understand in the context of the convective cell idea. The predominance of redshifted emission and the observed similarities and dissimilarities in profile structure of various SiO transitions are also unexplained if the masers are collisionally pumped in convective cells.

Although radiative pumping appears to be the most likely mechanism to explain SiO masers, a model consistent with all of the available observations has not yet been developed.

§3. Structure and Kinematics of the Inner Circumstellar Regions

Recent work by Hinkle and his collaborators (Hinkle 1978; Hinkle and Barnes 1979; Hinkle, Hall, and Ridgeway 1982) may shed some light on several perplexing aspects of the SiO maser phenomenon. Time monitoring spectroscopy between 1.6 and 2.5μ of the $\Delta v=1$, 2, and 3 vibration-rotation bands of CO toward χ Cyg shows evidence for four different components originating from different layers of the stellar atmosphere and circumstellar shell (Hinkle, Hall, and Ridgeway 1982; hereafter HHR). The second overtone ($\Delta v=3$) CO lines exhibit smooth and repeatable velocity variations of ~30 km s^{-1} amplitude through the stellar light cycle, indicating these lines are formed in a pulsating photospheric region. Between optical phases 0 to ~0.4, the lines are blueshifted from V_*, as the stellar oscillation is accelerating gas away from the surface. An outwardly propagating shock wave forms as rising gas collides with gas falling back to the surface from the previous cycle. During the second half of the cycle, the $\Delta v=3$ CO lines show increasingly redshifted velocities as the gas falls back to the surface prior to the emergence of the next shock. Such velocity variations, however, are <u>not</u> observed in the SiO maser lines. Furthermore, since both hydrogen emission lines and evidence of reduced CO column density are observed (HHR), the propagating shock evidently has sufficient energy not only to ionize H (13.6 eV) and dissociate CO (11.1 eV), but also to dissociate SiO (8.3 eV) in this region.

In contrast, the first overtone ($\Delta v=2$) CO lines (as well as absorption lines in the visual (Wallerstein 1979)) show consistently

redshifted velocities throughout the stellar cycle. This gas is evidently located beyond the photosphere (> 2 R_* from star center) and is infalling to the stellar surface. The presence of gas which is infalling throughout the stellar cycle may be intimately linked to the SiO maser lines which show predominance of redshifted emission and no phase-dependent velocity variations.

Of additional interest for the interpretation of SiO masers is the fact that the low excitation first overtone lines of CO exhibit unchanging velocities close to V_*, which HHR attribute to the presence of a "stationary layer" of gas located at a distance of order ~10 R_* from the photosphere, well outside the region affected by the stellar pulsation. The derived excitation temperature for this gas is ~800 K and the total mass is $\geq 10^{-5}$ $M_\odot$. Finally, low excitation fundamental lines show velocities and excitation consistent with formation in an expanding circumstellar envelope at ~300 K.

The stationary layer observed by HHR may provide a very suitable location for the SiO masers (as these authors have themselves suggested). Time variations over several stellar cycles in the properties of the CO gas observed from this region indicate the layer may be built up during a particularly violent stellar oscillation and maintained over several cycles by dissipation of energy from the outwardly propagating shocks. Considerable turbulence in this layer is implied by the observed IR line widths. HHR suggest that this layer may provide a reservoir from which material is accelerated outward by radiation

pressure on dust grains which condense at temperatures near 1000 K. In addition, gas may continually drain back down onto the surface from this layer, as is suggested by the redshifted velocities observed in the $\Delta v=2$ CO lines and the visual absorption lines.

The existence of this layer may explain several of the observed SiO maser properties. HHR report that such a layer has been identified in the ten Mira variables for which they have obtained infrared spectra. The long-term secular trends in the SiO maser flux of some sources may be associated with the build up and dissipation of the stationary layer. Unfortunately, HHR's long-term IR line monitoring in χ Cyg overlaps only slightly with the radio observations reported in this thesis. Future attempts to correlate variability in the stationary low excitation $\Delta v=2$ CO lines with maser variability would be extremely interesting.

The fact that the J=1-0 SiO lines are preferentially redshifted and have different velocity structure from the v=1, J=2-1 line, which is more or less symmetric about V_*, suggests these lines are formed in different regions. One possible explanation is that the v=1, J=2-1 masers may be located in the turbulent stationary layer; maser lines which are symmetric about V_* could in this case be formed from either radial or tangential path lengths. On the other hand, J=1-0 masers may occur preferentially in clumps of gas which are raining back down toward the surface; presumably, the extreme blueshifted velocities from infalling material on the backside of the star are occulted by the stellar disk. If the J=2-1 masers are formed farther from the star than the J=1-0

masers, this might help explain why the J=2-1 masers in high vibrational states are so much weaker than the J=1-0 masers in these states.

Further examination of these rather speculative ideas must be combined with a detailed re-examination of radiative maser pumping mechanisms before the complex SiO maser phenomenon can be fully understood. Combination of information derived from observations in different regions of the spectrum would seem to be a very fruitful approach to the problem.

BIBLIOGRAPHY

Balister, M., Batchelor, R.A., Haynes, R.F., Knowles, S.H., McCulloch, M.G., Robinson, B.J., Wellington, K.J., and Yabsley, D.E. 1977, M.N.R.A.S. 180, 415.

Barkat, Z., and Tuchman, Y. 1980, Ap. J. 237, 105.

Benson, J.M. 1978, Ph.D. Thesis, University of Iowa.

Buhl, D., Snyder, L.E., Lovas, F.J., and Johnson, D.R. 1974, Ap. J. 192, L97.

Buhl, D., Snyder, L.E., Lovas, F.J., and Johnson, D.R. 1975, Ap. J. 201, L29.

Bujarrabal, V., and Nguyen-Q-Rieu 1981, Ast. and Ap. 102, 65.

Cahn, J.H. 1981, Ast. J. 86, 1935.

Cahn, J.H. and Elitzur, M. 1979, Ap. J. 231, 124.

Cassinelli, J.P. 1979, Ann. Rev. Astron. Ap. 17, 275.

Castor, J.I. 1970, M.N.R.A.S. 149, 111.

Clark, B.G. 1973, Proc. IEEE 61, 1242.

Clark, F.O., Troland, T.H., Lovas, F.J., and Schwartz, P.R. 1981, Ap. J. 244, L99.

Clayton, M.L., and Feast, M.W. 1969, M.N.R.A.S. 146, 411.

Clemens, D.P., and Lane, A.P. 1982, preprint.

Cox, G.C., and Parker, E.A. 1979, M.N.R.A.S. 186, 197.

Davis, J.H., Blair, G.N., Van Till, H., and Thaddeus, P. 1974, Ap. J. 190, L117.

Davis, J.H., and Van den Bout, P.A., 1973, Ap. Lett. 15, 43.

Deguchi, S., and Iguchi, T. 1976, Publ. Ast. Soc. Jap. 28, 307.

Deguchi, S., Good, J., Fan, Y., Mao, X., Wang, D., and Ukita, N. 1982, preprint.

Dickinson, D.F. 1972, Ap. J. 175, L43.

Dickinson, D.F., Kollberg, E., and Yngvesson, S. 1975, Ap. J. 199, 131.

Dickinson, D.F., Reid, M.J., Morris, M., and Redman, R. 1978, Ap. J. 220, L113.

Elitzur, M. 1980a, Ap. J. 240, 553.

Elitzur, M. 1980b, Paper presented at workshop on "Physical Processes in Red Giants", Erice, Italy.

Engels, D. 1979, Ast. and Ap. Suppl. 36, 337.

Fillit, R., Proust, D., and Lepine, J.R.D. 1977, Ast. and Ap. 58, 281.

Foy, R., Heck, A., and Mennessier, M.O. 1975, Ast. and Ap. 43, 175.

Fusi-Pecci, F., and Renzini, A. 1976, Ast. and Ap. 46, 447.

Gehrz, R.D., and Woolf, N.J. 1971, Ap. J. 165, 285.

Genzel, R., Downes, D., Schwartz, P.R., Spencer, J.H., Pankonin, V., and Baars, J.W.M. 1980, Ap. J. 239, 519.

Genzel, R., Moran, J.M., Lane, A.P., Predmore, C.R., Ho, P.T.P., Hansen, S.S., and Reid, M.J., 1979, Ap. J. 231, L73.

Genzel, R., Reid, M.J., Moran, J.M., and Downes, D. 1981, Ap. J. 244, 884.

Goldreich, P., and Keeley, D.A. 1972, Ap. J. 174, 517.

Haisch, B.M., Linsky, J.L., and Basri, G.S. 1980, Ap. J. 235, 519.

Hansen, S.S. 1980, Ph.D. Thesis, University of Massachusetts.

Hartmann, L., and MacGregor, K.B. 1980, Ap. J. 242, 260.

Harvey, P.M., Bechis, K.P., Wilson, W.J., and Ball, J.A. 1974, Ap. J. Suppl. 27, 331.

Hedelund, J., and Lambert, D.L. 1972, Ap. Letters 11, 71.

Herbig, G.H. 1969, Mem. [8°] Soc. Roy. Sci. Liege.

Hill, S.J., and Willson, L.A. 1979, Ap. J. 229, 1029.

Hinkle, K.H. 1978, Ap. J. 220, 210.

Hinkle, K.H., and Barnes, T.G. 1979, Ap. J. 227, 923.

Hinkle, K.H., Hall, D.N.B., and Ridgway, S.T. 1982, Ap. J. 252, 697.

Hjalmarson, A., and Olofsson, H. 1979, Ap. J. 234, L199.

Hyland, A.R., Becklin, E.E., Frogel, J.A., and Neugebauer, G. 1972, Ast. and Ap. 16, 204.

Jewell, P.R., Elitzur, M., Webber, J.C., and Snyder, L.E. 1979, Ap. J. Suppl. 41, 191.

Kaifu, N., Buhl, D., and Snyder, L.E. 1975, Ap. J. 195, 359.

Knapp, G.R., Phillips, T.G., Leighton, R.B., Lo, K.Y., Wannier, P.G., Wootten, H.A., and Huggins, P.J. 1982, Ap. J. 252, 616.

Kwan, J., and Scoville, N. 1974, Ap. J. 194, L97.

Kwok, S., 1975, Ap. J. 198, 583.

Lambert, D.L., and Vanden Bout, P.A., 1978, Ap.J. 221, 854.

Lane, A.P. 1978, FCRAO Internal Memo.

Lane, A.P., Ho, P.T.P., Predmore, C.R., Moran, J.M., Genzel, R., Hansen, S.S., and Reid, M.J. 1980, in IAU Symposium #87, Interstellar Molecules, ed. B. Andrew, (Dordrecht: Reidel).

Lepine, J.R.D., and Paes de Barros, M.H. 1977, Ast. and Ap. 56, 219.

Lepine, J.R.D., LeSqueren, A.M., and Scalise, E. 1978, Ap. J. 225, 869.

Lo, K.Y., and Bechis, K.P., 1977, Ap. J. 218, L27.

Lockwood, G.W., and Wing, R.F. 1971, Ap. J. 169, 63.

Lockwood, G.W., and Wing, R.F. 1982, M.N.R.A.S. 198, 385.

Maciel, W.J. 1977, Ast. and Ap. 57, 273.

Manson, E.L., Jr., Clark, W.W., DeLucia, F.C., and Gordy, W. 1977, Phys. Rev. A 15, 223.

Maran, S.P., Heinsheimer, T.F., Stocker, T.L., Anand, S.P.S., Chapman, R.D., Hobbs, R.W., Michalitsanos, A.G., Wright, F.H., and Kipp, S.L. 1977, Infrared Physics 17, 565.

McIntosh, G.C., Lane, A.P., and Clemens, D.P. 1980, B.A.A.S. 12, 456.

Menietti, J.D., and Fix, J.D. 1978, Ap. J. 224, 961.

Moran, J.M. 1976, in Methods of Experimental Physics, Vol. 12, Part C, ed. M.L. Meeks (New York: Academic Press), p. 228.

Moran, J.M., Ball, J.A., Predmore, C.R., Lane, A.P., Huguenin, G.R., Reid, M.J., and Hansen, S.S. 1979, Ap. J. 231, L67.

Moran, J.M., Johnston, K.J., Spencer, J.H., and Schwartz, P.R. 1977, Ap. J. 217, 434.

Moran, J.M., Lichten, S., Reid, M.J., Huguenin, G.R., and Predmore, C.R. 1980 (in preparation).

Morris, M., Redman, R., Reid, M.J.,and Dickinson, D.F. 1979, Ap. J. 229, 257.

Nguyen-Q-Rieu, Laury-Micoulant, C., Winnberg, A., and Schultz,G.V. 1979, Ast. and Ap. 75, 351.

Olofsson, H., Hjalmarson, A., and Rydbeck, O.E.H. 1981, Ast. and Ap. 100, L30.

Olofsson, H., Johansson, L.E.B., Hjalmarson, A., and Nguyen-Q-Rieu 1982, Ast. and Ap. 107, 128.

Olofsson, H., Rydbeck, O.E.H., Lane, A.P., and Predmore, C.R. 1981, Ap. J. 247, L81.

Penzias, A.A., and Burrus, C.A. 1973, Ann. Rev. Astron. Ap. 11, 51.

Petit, E., and Nicholson, S.B. 1933, Ap. J. 78, 320.

Predmore, C.R., Goldsmith, P.F., Raisanen, A.V., Parrish, P.T., Marrero, K.L., and Kot, R.A. 1980, URSI Symposium on Millimeter Wave Technology, Grenoble.

Reid, M.J. 1976, Ap. J. 207, 784.

Reimers, D. 1977, in IAU Colloquium #42, The Interaction of Variable Stars with Their Environment, ed. R. Kippenhahn et al., Publ. Bamberg Obs.

Rosen, B.R., Moran, J.M., Reid, M.J., Walker, R.C., Burke, B.F., Johnston, K.J., and Spencer, J.H. 1978, Ap. J. 222, 132.

Salpeter, E.E. 1977, Ann. Rev. Astron. Ap. 15, 267.

Scalise, E., and Lepine, J.R.D. 1978, Ast. and Ap. 65, L7.

Schloerb, F.P., and Snell, R. 1980, FCRAO Internal Report #150.

Schwartz, P.R., Harvey, P.M., and Barrett, A.H. 1974, Ap. J. 187, 491.

Schwartz, P.R., Waak, J.A., and Bologna, J.M. 1979, Ast. J. 84, 1349.

Schwartz, P.R., Zuckerman, B., and Bologna, J.M. 1982, Ap. J. 256, L55.

Schwartzschild, M. 1975, Ap. J. 195, 137.

Silverglate, P., Zuckerman, B., Terzian, Y., and Wolff, M. 1979, Ast. J. 84, 1349.

Snyder, L.E., and Buhl, D. 1974, Ap. J. 189, L31.

Snyder, L.E., and Buhl, D. 1975, Ap. J. 197, 329.

Snyder, L.E., Dickinson, D.F., Brown, L.W., and Buhl, D. 1978, Ap. J. 224, 512.

Spencer, J.H., Johnston, K.J., Moran, J.M., Reid, M.J., and Walker, R.C. 1979, Ap. J. 230, 449.

Spencer, J.H., and Schwartz, P.R. 1975, Ap. J. 199, L111.

Spencer, J.H., Winnberg, A., Olnon, F.M., Schwartz, P.R., Matthews,H.E., and Downes, D. 1981, Ast. J. 86, 392.

Thaddeus, P., Mather, J., Davis, J.H., and Blair, G.N. 1974, Ap. J. 192, L33.

Tipping, R.H., and Chackerian, C., Jr. 1981, J. Mol. Spec. 88, 352.

Troland, T.H., Heiles, C., Johnson, D.R., and Clark, F.O. 1979, Ap. J. 232, 143.

Tuchman, Y., Sack, N., and Barkat, Z. 1978, Ap. J. 219, 183.

Tuchman, Y., Sach, N., and Barkat, Z. 1979, Ap. J. 234, 217.

Ukita, N., and Kaifu, N. 1980, in IAU Symposium #87, Interstellar Molecules, ed. B. Andrew, (Dordrecht: Reidel).

Ulich, B.L., Davis, J.H., Rhodes, P.J., and Hollis, J.M. 1980, IEEE Trans. Antennas Propagat., Vol. AP-28, p. 367.

Ulich, B.L., and Haas, R.W. 1976, Ap. J. Suppl. Series 30, p. 247.

Wallerstein, G.I. 1979, in IAU Colloquium #46, Changing Trends in Variable Star Research, ed. F.M. Bateson, J. Smak, and I. Urch (Hamilton, New Zealand: University of Waikato).

Wallerstein, G., and Greenstein, J. 1980, PASP 92, 275.

Weymann, R.J. 1977, in IAU Colloquium #42, The Interaction of Variable Stars with Their Environment, ed. R. Kippenhahn et al., Publ. Bamberg Obs.

Willson, L.A., and Hill, S.J. 1979, Ap. J. 228, 854.

Wilson, W.J., Barrett, A.H., and Moran, J.M. 1970, Ap. J. 160, 545.

Wilson, R.W., Penzias, A.A., Jefferts, K.B., Kutner, M., and Thaddeus, P. 1971, Ap. J. 167, L97.

Wolff, R.S., and Carlson, E.R. 1982, Ap. J. 257, 161.

Wood, P.R. 1979, in IAU Colloquium #46, Changing Trends in Variable Star Research, ed. F.M. Bateson, J. Smak, and I. Urch (Hamilton, New Zealand: University of Waikato).

Zuckerman, B. 1980, Ann. Rev. Astron. and Ap. 18, 263.

Zuckerman, B. 1981, Ast. J. 86, 84.

Zuckerman, B., Palmer, P., Gilra, D.P., Turner, B.E., and Morris, M. 1978, Ap. J. 220, L53.

Zuckerman, B., Palmer, P., Morris, M., Turner,B.E., Gilra, D.P., Bowers, P.F., and Gilmore, W. 1977, Ap. J. 211, L97.